AFRL-RV-PS-
TR-2011-0089
Vol. I

AFRL-RV-PS-
TR-2011-0089
Vol. I

PLASMA INTERACTIONS WITH SPACECRAFT

Volume I of II

V.A. Davis, et al.

Science Applications International Corporation
10260 Campus Point Drive, Mailstop A-2A
San Diego, CA 92121

15 April 2011

Final Report

AIR FORCE RESEARCH LABORATORY
Space Vehicles Directorate
3550 Aberdeen Ave SE
AIR FORCE MATERIEL COMMAND
KIRTLAND AIR FORCE BASE, NM 87117-5776

DTIC Copy

NOTICE AND SIGNATURE PAGE

AFRL-RV-PS-TR-2011-0089, Vol. I HAS BEEN REVIEWED AND IS APPROVED FOR PUBLICATION IN ACCORDANCE WITH ASSIGNED DISTRIBUTION STATEMENT.

//Signed//	//Signed//
Adrian Wheelock, RVBXR	Joel Mozer, PhD
Program Manager	Associate Chief, AFRL/RVB

REPORT DOCUMENTATION PAGE

Form Approved
OMB No. 0704-0188

Public reporting burden for this collection of information is estimated to average 1 hour per response, including the time for reviewing instructions, searching existing data sources, gathering and maintaining the data needed, and completing and reviewing this collection of information. Send comments regarding this burden estimate or any other aspect of this collection of information, including suggestions for reducing this burden to Department of Defense, Washington Headquarters Services, Directorate for Information Operations and Reports (0704-0188), 1215 Jefferson Davis Highway, Suite 1204, Arlington, VA 22202-4302. Respondents should be aware that notwithstanding any other provision of law, no person shall be subject to any penalty for failing to comply with a collection of information if it does not display a currently valid OMB control number. **PLEASE DO NOT RETURN YOUR FORM TO THE ABOVE ADDRESS.**

1. REPORT DATE *(DD-MM-YYYY)* 15-04-2011	2. REPORT TYPE Final Report	3. DATES COVERED *(From - To)* 07-02-2005 to 15-02-2011
4. TITLE AND SUBTITLE Plasma Interactions with Spacecraft		**5a. CONTRACT NUMBER** FA8718-05-C-0001
		5b. GRANT NUMBER
		5c. PROGRAM ELEMENT NUMBER 62601F
6. AUTHOR(S) V.A. Davis, M.J. Mandell, S.L. Huston, B.M. Gardner		**5d. PROJECT NUMBER** 4827
		5e. TASK NUMBER
		5f. WORK UNIT NUMBER 849760
7. PERFORMING ORGANIZATION NAME(S) AND ADDRESS(ES) Science Applications International Corporation 10260 Campus Point Drive, Mailstop A-2A San Diego, CA 92121		**8. PERFORMING ORGANIZATION REPORT NUMBER**
9. SPONSORING / MONITORING AGENCY NAME(S) AND ADDRESS(ES) Air Force Research Laboratory Space Vehicles Directorate 3550 Aberdeen Ave SE Kirtland AFB, NM 87117-5776		**10. SPONSOR/MONITOR'S ACRONYM(S)** AFRL/RVBXR
		11. SPONSOR/MONITOR'S REPORT NUMBER(S) AFRL-RV-PS-TR-2011-0089, Vol. I

12. DISTRIBUTION / AVAILABILITY STATEMENT

Approved for public release; distribution is unlimited. (377ABW-2011-0384; 22 March 2011)

13. SUPPLEMENTARY NOTES

14. ABSTRACT
The objective of this contract is to develop, incorporate, test, and validate new algorithms for *Nascap-2k* that are needed to self-consistently compute plasma transport and to model electromagnetic radiation in the near to mid field from very low frequency (VLF) (3 kHz to 30 kHz) antennas. The plasma flow models can be used to address various plasma engineering concerns including surface discharges due to meteoroid impact and spacecraft contamination due to electric propulsion plasma plume effects. The goal of this effort is to provide a plasma engineering capability to the spacecraft community. Progress was made on Nascap-2k development, particularly charging with time-dependent bias values, macroparticle splitting and injection, and algorithm development of charging with tabular spectra generated by magnetospheric models. New database and memory manager software was developed for *Nascap-2k*. Support was provided for the DSX program. An algorithm was developed for the calculation of surface currents on a satellite that is acting as an antenna.

15. SUBJECT TERMS
Nascap-2k, potentials, space environment, spacecraft, spacecraft charging, DSX, N2kDB

16. SECURITY CLASSIFICATION OF:			17. LIMITATION OF ABSTRACT	18. NUMBER OF PAGES	19a. NAME OF RESPONSIBLE PERSON Adrian Wheelock
a. REPORT Unclassified	**b. ABSTRACT** Unclassified	**c. THIS PAGE** Unclassified	Unlimited	108	**19b. TELEPHONE NUMBER** *(include area code)*

Standard Form 298 (Rev. 8-98)
Prescribed by ANSI Std. 239.18

i

This page is intentionally left blank.

TABLE OF CONTENTS

Section	Page

LIST OF FIGURES

LIST OF TABLES

1. INTRODUCTION

In support of the goal to provide a plasma engineering capability to the spacecraft community, the objective of the Plasma Interactions with Spacecraft contract is to develop, incorporate, test, and validate new algorithms for the three-dimensional plasma-environment spacecraft interactions computational tool, *Nascap-2k.* These algorithms are required to self-consistently compute plasma transport and to model electromagnetic radiation in the near to mid field from very low frequency (VLF) (3 kHz to 30 kHz) antennas. The plasma flow models can be used to address various plasma engineering concerns including surface discharges due to meteoroid impact, and spacecraft contamination due to electric propulsion plasma plume effects.

Under this contract, support was provided for the DSX (Demonstration and Science eXperiments) program. In addition to program support, this included adding capabilities to *Nascap-2k* to enable near field modeling and developing an algorithm for the computation of surface currents on a satellite acting as an antenna. Another task was the development of a prototype of *Nascap-2k RealTime* for use by the SEEFS (Space Environmental Effects Fusion System) program. A significant effort was the development and integration of a new database and memory manager software for *Nascap-2k.* The earlier database software, while more than sufficient in its time, created severe limitations on further *Nascap-2k* development and calculation ability. The new database and memory manager successfully removes these limitations.

1.1 Related Documents

The following three documents were prepared under this contract and are being delivered under separate cover.

N2kDB Database and Memory Manager Software for Nascap-2k, V.A. Davis, N.R. Baker, B.G. Gardner, R.A. Kuharski, M.J. Mandell, A.J. Ward, K.G. Wilcox

Nascap-2k Scientific Documentation, M.J. Mandell and V.A. Davis

Nascap-2k Programmer's Documentation, V.A. Davis, M.J. Mandell, K.G. Wilcox

1.2 *Nascap-2k* Software Development

Nascap-2k was developed by Science Applications International Corporation (SAIC) with funding from the National Aeronautics and Space Administration (NASA) and the Air Force Research Laboratory (AFRL). Under this contract, *Nascap-2k* was improved with new and enhanced algorithms, and its calculation capabilities were expanded. Here, we list many of the specific tasks performed under this effort.

The most significant development effort has been the design, creation, and implementation of **N2kDB**, the new database and memory management software, summarized in Section 1.3 below. This software is documented in *N2kDB Database and Memory Manager Software for Nascap-2k*, delivered under separate cover.

A number of enhancements were made specifically to enable DSX near-field calculations. These are summarized in Section 1.2 below.

At contract end, in February 2011, we are delivering *Nascap-2k* 4.1 RC (release candidate). This version includes the new database and memory management software and the latest code improvements. In January 2009, before incorporation of the new database and memory manager software, *Nascap-2k* 3.2 was released to AFRL and the NASA SEE Program, which handles distribution. *Nascap-2k* 3.1 was released to AFRL and the NASA SEE Program in July 2005. All of these versions of *Nascap-2k* were tested on our standard suite of test cases on both Windows and Linux. In addition, a number of interim deliveries of the code to AFRL were made (April 2006, July 2006, March 2008, October 2008, August 2010, and November 2010).

To develop and test the parallel processing capabilities and 64-bit compatibility of *Nascap-2k*, we ported the code to a four processor Apple Macintosh Pro with the MacOS X.5 operating system with Intel C++ and Fortran compilers. To resolve LINUX installation issues, we purchased a computer with a 64-bit AMD multicore microprocessor and installed CentOS v5.4 and Portland Group compiler suite 10.9. With this new computer we resolved the final issues and *Nascap-2k* is now fully compatible with the Windows, CentOS LINUX, and 64-bit MacOS X environments.

N2kScriptRunner, a C++ code that runs a *Nascap-2k* script outside of the Java user interface, was created. Using **N2kScriptRunner**, we compiled, linked, and ran *Nascap-2k* using the OpenMP compiler commands for multiprocessor operations.

An improvement was made to the algorithm used to display fields (such as charge density) that are stored as nodal extensive quantities. The approach used is described in Section 2.

In addition to the above, we made a number of small changes to *Nascap-2k*. The most notable are the following:

> Revised the color scale used on the **Result 3D** tab. The new color scale maps monotonically to gray levels.

> Added monopole and debye screening boundary conditions to reduce perturbations to free space problems caused by a grounded boundary.

> Made a number of changes to the Particle Tracking and Potentials in Space modules recommended by AFRL to make these modules parallelizable.

> Implemented the ability to specify and display a parameter on multiple planes at once on the **Results 3D** tab.

> Added to the **Results** tab the ability to view the surface number of the surface with the minimum and maximum value of the displayed quantity.

Added to the **Results 3D** tab the ability to view the components of the current for all timesteps.
Added the ability to display results from any timestep on the **Results 3D** tab.

Added the ability to select a view direction from the sun, from the ram, and from a user specified direction for the **Results 3D** tab display.

Added Freja environments as default auroral environments on the **Environment** tab.

Made the specification of an insulating surface as "fixed potential" work properly.

Removed the use of XML schema files for input validation.

Added a check to make sure that the particle file filename is no more than 20 characters (the most that can be read by the keyword input routines used by Tracker).

Revised coding so that a missing conductor number is allowed.

Implemented the ability to close one project and open another project from the Java user interface without shutting down the code.

Implemented the buttons on the **Problem** tab under LINUX.

Revised the tracking of the last directory used. The file that contains the latest directory used is now saved either in the install directory or the user's home directory, depending on the operating system and access of the user to the install directory.

We added a warning when a user saves an object in which a node of one surface element is contained within another surface element.

The user interface was revised to allow for easy use of the new capabilities. The user documentation was updated to reflect the user interface and code changes.
We discussed collaborating with AFRL/RZSS to make RZSS's code COLISEUM and *Nascap-2k* work together.

We wrote *Nascap-2k Scientific Documentation* and *Nascap-2k Programmer's Documentation*, both delivered under separate cover.

1.3 *Nascap-2k* **for DSX**

To compute the sheath structure and currents about the DSX VLF antenna, a number of capabilities were added to *Nascap-2k*. This included improvements to *Nascap-2k*'s surface charging and PIC (Particle-in-cell) computational capabilities.

The ability to inject macroparticles carrying charge at the boundary of the computational space was implemented. The model now has the ability to split macroparticles carrying charge immediately after creation, thus creating a representation of the thermal distribution, when the

macroparticles are created either throughout or at the boundary of the computational space. We also implemented the ability to split particles carrying either charge or current at the subgrid boundaries as needed. A discussion of these additional capabilities and our testing is included in Section 3.

Upon making one minor code change, we established that currents computed in time-dependent *Nascap-2k* calculations can be used to compute the change in potential of spacecraft surfaces. First, it was verified that the current to surfaces, computed during tracking, is used to compute the change in potential and, second, that the current is being used correctly in the calculation of the change in surface potential. We also added the ability to include an analytic electron current in a Hybrid PIC charging calculation. This capability is discussed in Section 4.

The **Charge Surfaces** module of *Nascap-2k* was modified so that the user may specify a time-varying bias value consisting of multiple Fourier components. The conductor potentials are appropriately adjusted to account for the internal current flow as the bias potential changes.

The *Nascap-2k* user interface was modified to allow the ability to specify a loop within the script. We added iteration-number-dependent execution of the **Save** and **Create Particles** commands.

A self-consistent calculation was performed of the space potentials and current to the CHAWS (Charging Hazards And Wake Studies) probe on the Wake Shield Facility (WSF) using the Hybrid PIC approach. The previous charge stabilization algorithm is ineffective in dense plasmas. With the incorporation of the new database it became possible to save the volume ion density during PIC calculations. This allowed us to implement a new algorithm that linearizes about the barometric potential rather than about zero potential. We also added the ability to generate a variable positional, angular, and energy distribution of macroparticles for PIC boundary injection. After making these changes, we repeated the CHAWS calculation using the Hybrid PIC approach. The results are described in Section 5.

We also added the optional ability, when tracking macroparticles carrying charge, to deposit charge on the nodes at the end of each sub-step rather than at the end of the time step. The applicability and stability of this numeric technique for typical *Nascap-2k* plasma physics problems is under evaluation. For a simple problem, we showed that as long as there are enough macroparticles, standard PIC and the orbit-averaged approach give the same results. This discussion appears in Section 6.

We added to Nascap-2k the infrastructure need for PIC (particle-in-cell) calculations with two species with different timescales (hydrogen ions and electrons).

A technique was developed for the evaluation of transverse surface currents along the DSX antennas and implemented it in *Nascap-2k*. We developed a related algorithm for the computation of volume electron currents. At present this algorithm is implemented in a stand-alone Java code and uses ion densities from an existing *Nascap-2k* database. A description of the algorithms is in Section 7.

We added the ability to use surface and volume currents to compute the vector potential, magnetic field, and time derivative of the vector potential. The earlier implementation of volume ion currents was corrected. A description of the algorithm is in Section 7.

The user interface was revised to allow for easy use of the new capabilities. The user documentation was updated to reflect the user interface and code changes.

1.4 New Database and Memory Manager

Early in this contract, we reviewed the original *Nascap-2k* database and memory management system, the specification, the desired capabilities of the replacement, and available open source databases that would be available for our use. We determined the requirements of a new database and memory management system for *Nascap-2k*. The requirements document appeared as an appendix to AFRL-VS-HA-TR-2007-1062, the first interim report for this contract.

During the fourth year of this contract, we focused on designing, building, and implementing into *Nascap-2k* the new database and memory management software, **N2kDB**. During the fifth and sixth years, we revised *Nascap-2k* to take full advantage of the new structure. We revised the way quantities associated with conductors, material properties, particle species, and other data are saved in order to increase (or eliminate) limitations on the numbers of conductors, materials, species, and timesteps.

A Software Design Document was produced that describes the software design, test procedures, and software standards. The document was revised during development as the design matured. Versions appeared as appendices to several quarterly reports. Sections of this document were subsequently reorganized into *N2kDB Database and Memory Manager Software for Nascap-2k*.

We developed **N2kDB Test**, a database testbed code. **N2kDB Test** has the same structure as *Nascap-2k* and uses the database in the same manner. It is a small manageable code that we used for testing the database software during development and for developing the proper implementation of the new commands. After incorporation of **N2kDB** into *Nascap-2k* this code is no longer useful and is no longer maintained.

We developed two versions of **N2kDBTool** (console-based and with a Java interface), a stand alone program that reads and writes *Nascap-2k* database files. This program proved invaluable during development of **N2kDB** and promises to be useful in future *Nascap-2k* development. **N2kDBTool** is included with *Nascap-2k*.

N2kDB also includes two testing programs (**msiotest** and **dmtest**) that verify the behavior of the database code itself. They verify that the requested operation is performed correctly. (**N2kDB Test** was used to verify that the appropriate operation is requested.) These codes will be maintained with **N2kDB**, but will *not* be distributed to users.

N2kDB satisfies all the requirements specified in the software requirements document. A review of how these requirements are satisfied is given in an appendix to *N2kDB Database and Memory Manager Software for Nascap-2k*.

Before incorporation of **N2kDB** into *Nascap-2k*, we released *Nascap-2k* 3.2.

In order to simplify the transition, we first implemented **N2kDB** into *Nascap-2k* using wrappers between the original database commands and the new ones. The old database commands were subsequently replaced with direct calls to the new database software. The code was tested on a suite of problems after each stage.

1.5 *Nascap-2k* RealTime

We developed a prototype for *Nascap-2k RealTime*, a computer code that computes surface potentials on spacecraft in response to tabular spectra generated by magnetospheric models. It uses a robust version of the charging algorithms developed for *Nascap-2k* and is an independent executable written in Java, using code originally developed for the *SEE Spacecraft Charging Handbook*. The charging algorithms are only appropriate to the plasma environment found at geostationary altitude and the sun direction computation also assumes that the spacecraft is at geostationary altitude. The most important feature of this code is that it runs reliably and fast. Final documentation of this code appears in Section 8.

Once *Nascap-2k RealTime* was developed, we examined the coupling of a magnetospheric model (*MSM*) with *Nascap-2k RealTime*. We used a simplified geometric model of DSCS-III. After several preliminary calculations, we selected appropriate material properties. Using this model, we calculated frame charging for three days using MSM output generated using three different MSM input parameter sets. The results were included in the presentation prepared by Dr. Robert Hilmer of AFRL, AGU Fall Meeting Paper SM41A-1169, "Spacecraft Surface Charging Application Development for Geosynchronous Orbit**,"** R.V. Hilmer, D.L. Cooke, M. Tautz, V.A. Davis, M. J. Mandell, and R.A. Kuharski.

1.6 MEO Radiation

We analyzed pitch-angle distributions from the CRRES MEA and HEEF electron detectors. We examined the anisotropy factor and the perpendicular component of the flux. Details are given in Section 9.

1.7 DSX Calculations

In 2007 we used *Nascap-2k* to perform a set of self-consistent calculations of the plasma response to a high voltage square wave VLF antenna using the capabilities implemented at that time. These calculations were the first full test of all of the new capabilities. We learned that the inclusion of a representation of the thermal distribution at the boundary can influence the current collected by the antenna arms. These calculations are included in a paper prepared for the 2007 Spacecraft Charging Technology Conference (M.J. Mandell, V.A. Davis, D.L. Cooke, A.T. Wheelock, C.J. Roth, *Nascap-2k* Self-consistent Simulations of a VLF Plasma Antenna, *Spacecraft Charging Technology Conference*, Biarritz, France, June 2007).

After implementation of the new database and the other code revisions discussed above, we repeated these calculations. The new calculations use an updated geometric model, have a larger computational space, include a larger number of macroparticles, and have improved resolution about the antenna. The calculations are included in a paper prepared for the 2010 Spacecraft

Charging Technology Conference (M.J. Mandell, V.A. Davis, D.L. Cooke, A.T. Wheelock, C.J. Roth, *Nascap-2k* Self-consistent Simulations of a VLF Plasma Antenna, *Spacecraft Charging Technology Conference*, Albuquerque, New Mexico, September 2010).

Since September 2010, we extended the calculations, performed calculations including any effect of the magnetic field on the ion motion, and performed a calculation at higher voltage. There is no magnetic field effect on ion motion. Increasing the applied voltage from 1 kV to 5 kV led to no apparent qualitative differences.

The final results are discussed in Section 10.

1.8 DSX Program Support

In addition to calculations of the near field response to the DSX antenna, we supported the DSX program by participating in various meetings and teleconferences.

Via teleconference, Dr. Mandell attended the October 4, 2006 DSX HSD Solar Array Subsystem Preliminary Design Review held in Littleton, CO.

We took an active role in the Y-boom high voltage isolation design discussion. To that end, Dr. Myron J. Mandell participated in the following teleconferences and meetings.

- Weekly teleconferences with Y Antenna supplier (L'Garde) from November 6, 2007 to through February 13, 2008.

- A visit to the L'Garde facility to discuss the design issues on November 7, 2007.

- Y Antenna Isolation teleconference on December 19, 2007.

- Weekly teleconferences with the alternate supplier of Y Antenna (ATK) from January 15 to February 25, 2008.

- ATK Isolation face-to-face at Houston Airport (IAH) on February 13, 2008.

- DSX Alternative Y Antenna CDR, Goleta, California on February 26 by teleconference.

- DSX Y Antenna CDR at L'Garde, Tustin, California on February 27.

Dr. Myron Mandell attended and made a presentation at the Workshop on The Remediation of Enhanced Radiation Belts in Lake Arrowhead, California on March 3-6, 2008.

Dr. Mandell attended the DSX System CDR, Breckenridge, Colorado, May 6-8, 2008.

Dr. Mandell attended the MURI Review and RBR Workshop at Stanford in Palo Alto, California, February 18-19, 2009.

Dr. Mandell and Dr. Davis attended the DSX Science Team Meeting at Lake Arrowhead, CA, on September 15-18, 2009. Dr. Mandell made a presentation.

1.9 Contract

The scientists and other researchers who contributed to this work are Dr. Myron J. Mandell, Dr. Victoria A. Davis, Dr. Stuart L. Huston, Dr. Robert A. Kuharski, Dr. Michael Brown-Hayes, Ms. Barbara M. Gardner, Ms. Katherine Wilcox, Ms. Alisa J. Ward, and Mr. Nicholas R. Baker.

This contract continues work performed under earlier contracts: F19628-91-C-0187, Space System-Environment Interactions Investigation; F19628-93-C-0050, Modeling and Post Mission Data Analysis; F19628-89-C-0032, Analysis of Dynamical Plasma Interactions with High Voltage Spacecraft; and F19628-98-C-0074, Spacecraft Potential Control. NASA supported related work under contracts NAS8-98220 and NAS8-02028.

1.10 Publications

The following publications were supported in total or in part by this contract.

M.J. Mandell, V.A. Davis, D.L. Cooke, A.T. Wheelock, *Nascap-2k* Spacecraft Charging Code Overview, Proceedings of the 9th Spacecraft Charging Technology Conference, Tsukuba, Japan, 2005.

V.A. Davis, M.J. Mandell, F.J. Rich, D.L. Cooke, Reverse trajectory approach to computing ionospheric currents to the Special Sensor Ultraviolet Limb Imager on DMSP, Proceedings of the 9th Spacecraft Charging Technology Conference, Tsukuba, Japan, 2005.

M.J. Mandell, V.A. Davis, D.L. Cooke, A.T. Wheelock, C.J. Roth, *Nascap-2k* simulations of a VLF plasma antenna, Proceedings of the 9th Spacecraft Charging Technology Conference, Tsukuba, Japan, 2005.

M.J. Mandell, V.A. Davis, D.L. Cooke, A.T. Wheelock, *Nascap-2k* spacecraft charging code overview, *IEEE Trans Plasma Science, 34*, No. 5, p 2084, 2006.

V.A. Davis, M.J. Mandell, F.J. Rich, D.L. Cooke, Reverse trajectory approach to computing ionospheric currents to the Special Sensor Ultraviolet Limb Imager on DMSP, *IEEE Trans Plasma Science, 34*, No. 5, p 2062, 2006.

V.A. Davis, M.J. Mandell, D.L. Cooke, D.C. Ferguson, *Nascap-2k* spacecraft plasma environment interactions modeling: Capabilities and verification, AIAA 2007-1096, Aerospace Sciences Meeting and Exhibit, Reno, 2007.

M.J. Mandell, V.A. Davis, B.M. Gardner, F.K. Wong, R.C. Adamo, D.L. Cooke, A.T. Wheelock, Charge Control of Geosynchronous Spacecraft using Field Effect Emitters, AIAA 2007-284, Aerospace Sciences Meeting and Exhibit, Reno, 2007.

M.J. Mandell, V.A. Davis, D.L. Cooke, A.T. Wheelock, C.J. Roth, *Nascap-2k* Self-consistent Simulations of a VLF Plasma Antenna, *Spacecraft Charging Technology Conference*, Biarritz, France, June 2007.

M.J. Mandell, V.A. Davis, E.J. Pencil, M.J. Patterson, H.K. McEwen, J.E. Foster, J.S Snyder, Modeling the NEXT Multi-Thruster Array Test with *Nascap-2k*, *Spacecraft Charging Technology Conference*, Biarritz, France, June 2007. (Original research supported by NASA.)

M.J. Mandell, V.A. Davis, E.J. Pencil, M.J. Patterson, H.K. McEwen, J.E. Foster, J.S Snyder, Modeling the NEXT Multi-Thruster Array Test with *Nascap-2k, IEEE Transactions on Plasma Science, 36*, p. 2309, 2008. (Original research supported by NASA.) V.A. Davis, M.J. Mandell, D.L. Cooke, A.T. Wheelock, C.J. Roth, *Nascap-2k* Self-consistent Simulations of a VLF Plasma Antenna, *Spacecraft Charging Technology Conference*, Albuquerque, New Mexico, September 2010.

M.J. Mandell, V.A. Davis, D.L. Cooke, A.T. Wheelock, C.J. Roth, Pseudopotential algorithms for simulation of VLF plasma antenna current flow, *Spacecraft Charging Technology Conference*, Albuquerque, New Mexico, September 2010.

We made presentations or supported others who made presentations at the following meetings.

9th Spacecraft Charging Technology Conference, Tsukuba, Japan, April 2005.
    (Papers listed above.)

Sleight of HAND (RBR Phase 2 Kickoff) Meeting, Hanscom AFB, September 2005.
    M. J. Mandell, Antenna Sheath Modeling.

AGU Fall Meeting, San Francisco, CA, December 2005
    R.V. Hilmer, D.L. Cooke, M. Tautz, V.A. Davis, M. J. Mandell, and R.A. Kuharski, Spacecraft surface charging application development for geosynchronous orbit, SM41A-1169.

45th Aerospace Sciences Meeting, Reno, NV, January 2007.
    (Papers listed above.)

10th Spacecraft Charging Technology Conference, Biarritz, France, June 2007.
    (Papers listed above.)

Workshop on Remediation of Enhanced Radiation Belts, Lake Arrowhead, CA, March 2008.
    M. J. Mandell, V. A. Davis, D. L. Cooke, A. T. Wheelock, C. J. Roth, *Nascap-2k* simulations of static and dynamic sheaths.

GOMACTech-08, Las Vegas, NV, March, 2008.
    M.J. Mandell, V.A. Davis, A. Wheelock, D.L. Cooke, Modeling Space Weather Effects using *Nascap-2k*.

47th AIAA Aerospace Sciences Meeting, Orlando, FL, January 2009
    D.L. Cooke, A.T. Wheelock, V.A. Davis, M.J. Mandell, Simulation of auroral charging in the DMSP environment, AIAA 2009-350.

DSX Science Team Meeting, Lake Arrowhead, CA, September 2009
   M. J. Mandell and V. A. Davis, *Nascap-2k* surface current calculations.

11th Spacecraft Charging Technology Conference, Albuquerque, NM, September 2010.
(Papers listed above.)

2. PLOTTING AND POTENTIAL CALCULATION IMPROVEMENTS

2.1 Monopole Boundary Condition

When potentials are long-range, the shape and size of the sheath may be substantially affected by a zero potential outer boundary. This was recognized in NASCAP/GEO, where a 1/r boundary potential could be set with magnitude proportional to the computed charge on the object. No such option was implemented for subsequent codes, as their intended regime of applicability was dense plasma, and thus potentials were always short-range.

In Nascap-2k the problem was often apparent during tenuous plasma calculations. Addition of outer grids was not always sufficient to adequately minimize the problem, while adding substantially to the problem's size and complexity.

The algorithm implementing monopole boundaries is based on adding finite elements extending from the problem boundary to infinity. The consequent residuals to be added to the boundary nodes can be calculated analytically for Laplacian potentials. The algorithm is implemented as well for linearly screened (finite debye length) potentials, although for that case some of the integrals have been approximated. While this treatment makes the approximation that the center of charge is at the grid center, it does not depend on knowledge of the object charge, nor does it require the boundary potential to be symmetric about the grid center.

Examples of potential calculations with zero potential and with monopole boundary conditions are shown in Figure 1.
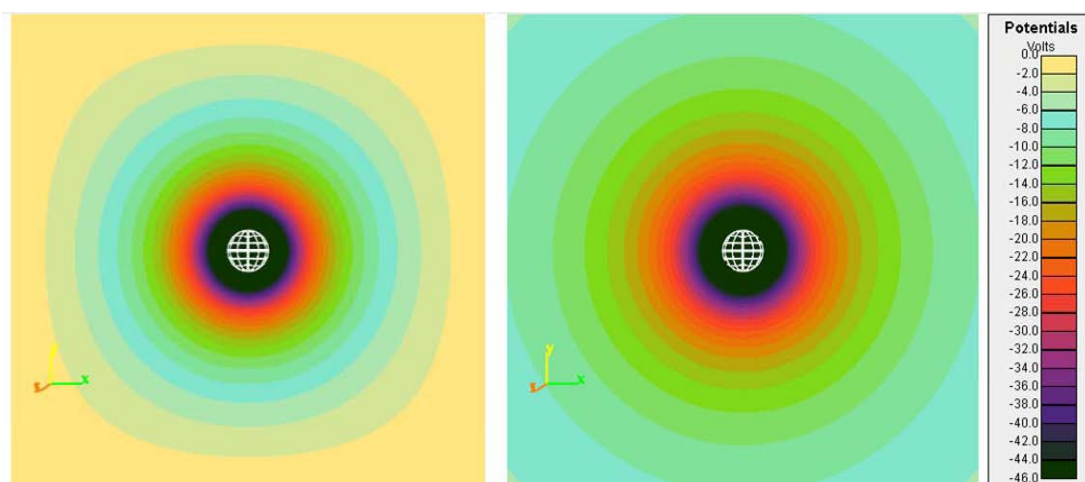
Figure 1. Potential Calculation Using Zero Potential Boundary Conditions (Left) and Monopole Boundary Conditions (Right)

2.2 Multiple Cut Planes

We implemented machinery and a user interface to display multiple cut planes simultaneously. An arbitrary number of cut planes can be defined (by normal direction and offset) and individually shown and hidden. An example is shown in Figure 2.
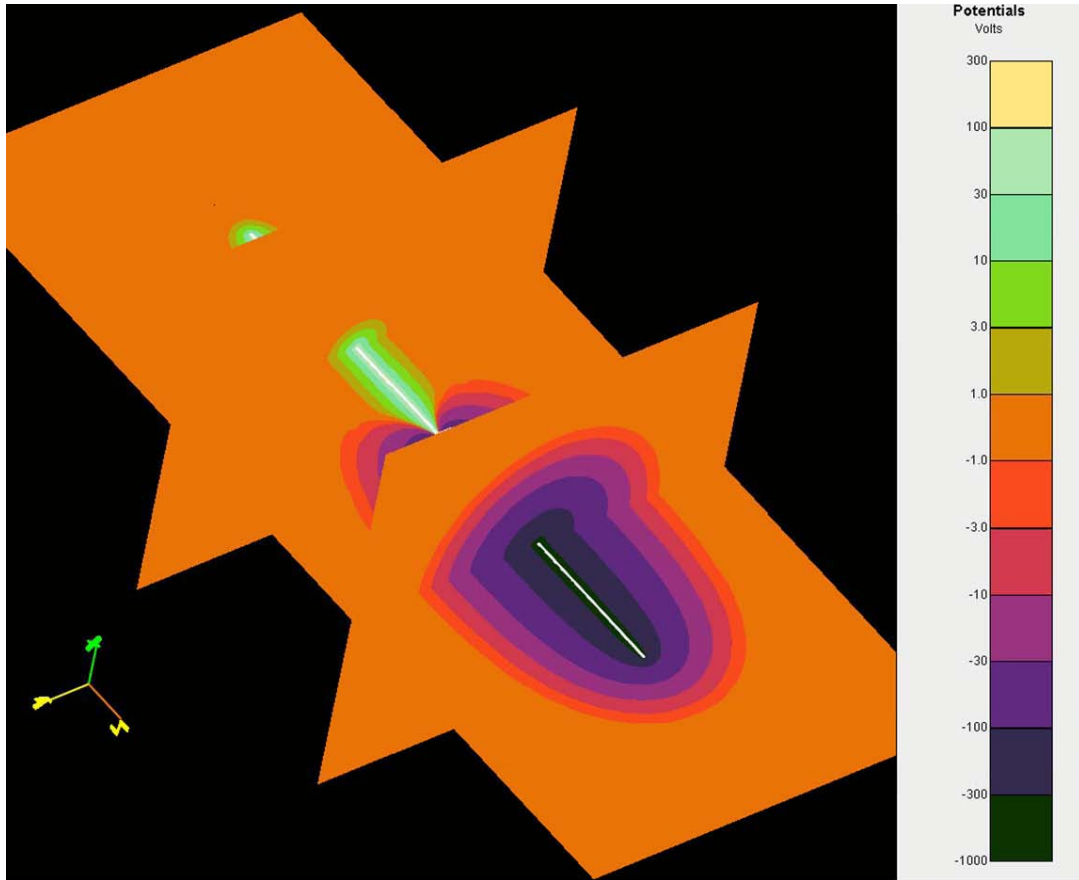
Figure 2. Example of Multiple Cut Plane Display

2.3 Nodal Charge Density

Using an earlier version of *Nascap-2k*, attempts were made to plot the value of the Nodal Charge Density on a cutplane. The plots had non-physical structures, particularly near grid boundaries. Also, the Nodal Charge Density on a plane as displayed on the **3-D Results** tab showed non-physical values along grid boundaries. The reason for the non-physical values is that the Nodal Charge Density as displayed is actually the charge on each node as stored in the database and used in the calculations (an extensive quantity) converted to the charge density (an intensive quantity) for the purpose of display. Extensive quantities exist only on nodes, and therefore it does not make sense to discuss their values at arbitrary points. The correct way to convert an extensive quantity to an intensive quantity is essentially to multiply by the inverse of the volume matrix. Unfortunately, while straightforward, implementing this is quite complex. With a moderate level of effort we were able to implement an improvement to the display of nodal extensive quantities.

We added two grid interface operations to the cut plane display routines. One grid interface operation is before and one after the division of each node by mesh volume. In the first grid interface operation, the extensive quantity on nodes on grid boundaries is transferred from the inner (finer) grid to the outer (coarser) grid. In the second, the intensive quantity (resulting from the division by volume) is interpolated from the outer grid to the inner grid boundary nodes. No adjustment is made to account for the fact that the appropriate volume for grid interface nodes and those near the object is not the cube of the mesh unit.

The nodal charge density, derived from the nodal charge using the old and new approaches for display, is shown in the Figure 3 and Figure 4 for the moving sphere problem. Most of the artificial structures on the grid boundaries have been eliminated.
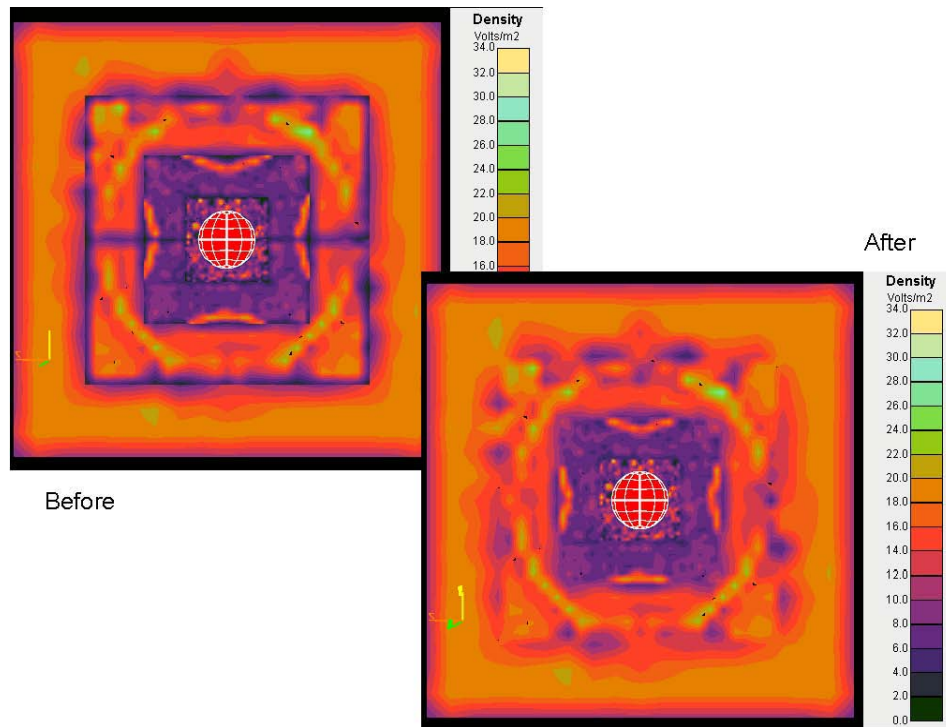
Figure 3. Nodal Charge Density on X = 0 Plane Using Original and Revised Algorithm for Display of Extensive Quantity
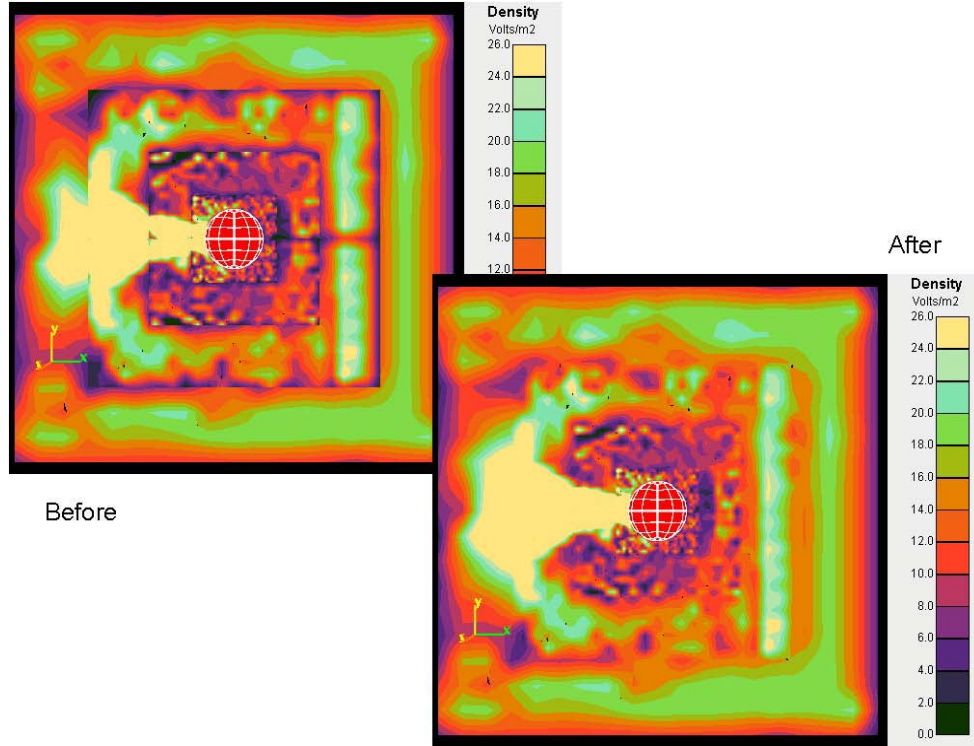
Figure 4. Nodal Charge Density on Z = 0 Plane Using Original and Revised Algorithm for Display of Extensive Quantity

3. SPLITTING AND INJECTING PARTICLES IN *NASCAP-2K*

This section outlines coding and testing performed for splitting of particles in *Nascap-2k*. The desirability of particle splitting has become apparent both to avoid having heavy particles in well-resolved regions and to simulate a thermal distribution. Splitting is done in such a way that merging of particles is straightforward, although it is not obvious that particle merging is needed in *Nascap-2k*. Injecting thermal particles at boundaries is also part of this effort.

3.1 General Principles

1. Particles are split in velocity space only. Because we frequently find ourselves in high-field regions, spatial splitting would raise problems with energy conservation.

2. To be split in velocity space, each particle must carry a temperature. We assume the temperature is always isotropic. The fission products carry half the temperature of the original particle, while the remaining thermal energy appears as kinetic energy of the split particles. PartGenDLL initializes the temperature to the value of TION (even for electrons).

3. For splitting purposes, we define the Z-axis to be along the direction of the particle velocity, the X-axis randomly chosen in the plane normal to Z, and the Y-axis mutually perpendicular.

4. We split into two or three particles with added velocity along each axis, except that we may elect not to split along the Z-direction if the kinetic energy exceeds the thermal energy. Not

splitting along Z helps ameliorate particle proliferation, but makes an error by not preserving the original particle temperature along Z. We thus end up with eight, nine, or twenty-seven new particles.

5. Particle velocity is assumed to be acquired by acceleration rather than actual drift (i.e., spacecraft velocity). If there is actual drift (e.g., ram velocity), then the drift velocity should be removed before splitting the particle, and added back after.

6. If the particle with speed u_0 is split by two along the X or Y axis, the new velocity is $\pm 0.707\sqrt{T/m}$ Along the Z axis, the velocity increment is calculated as if the temperature were $T - 2mu_0^2\left(\sqrt{1 + \dfrac{T}{mu_0^2}} - 1\right)$.

7. If the particle with speed u_0 is split by three along the X or Y axis, there is a zero-velocity central particle and two "probe" particles with velocity $\pm 0.866\sqrt{T/m}$. Along the Z axis, the velocity increment is calculated as if the temperature were $T - 2mu_0^2\left(\sqrt{1 + \dfrac{T}{mu_0^2}} - 1\right)$.

3.2 Implementation

Particle splitting has been implemented in PartGenDLL for particles read from an external file, for space-filling default particles, and for particles injected from the boundary. Particles are split if the keyword SPLIT appears in the input file. Particles read from an external file are split using the default option and the others are split using the eight-particle option.

3.3 Examples

This example was run using the "Sphere Hybrid PIC" problem that we have been using to develop, document, and test PIC currents and charging. A 2.4-m cubic space is filled with H^+ with 1-eV temperature and density 10^{10} m^{-3}. The ions are collected by a 10-cm radius probe biased to -100 V. The collection of ions by the probe and the loss of ions out the sides are monitored, and the final potential and particle configurations are inspected. Conceptual errors were found with the way this problem was set up, mostly relating to the velocity initialization by subroutine INIVEL prior to the splitting of the particles.

Figure 5 shows the initial results, with the calculation performed with the old velocity initialization, with the addition of particle splitting. The collected current, estimated to be 40 µA in equilibrium, rapidly rises to a sustained value of about 100 µA. The escaping current, estimated at 200 µA, averages to a mere 15 µA. Figure 6 shows the potentials after 25 µs. The admirably spherical sheath is surrounded by a ring of positive potentials (~0.3 V).
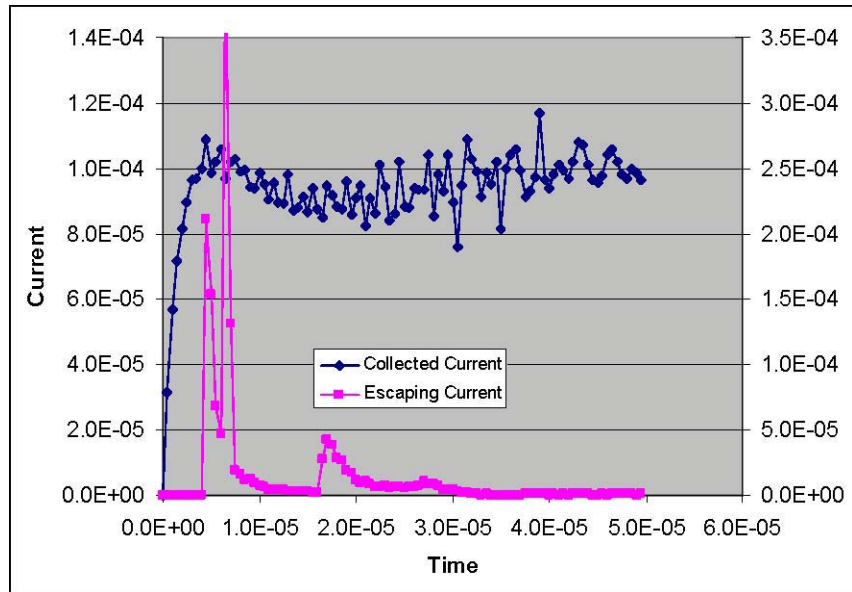
Figure 5. Collected Current (Left Scale) and Escaping Current (Right Scale) Using Default Script and Original INIVEL Velocity Initialization
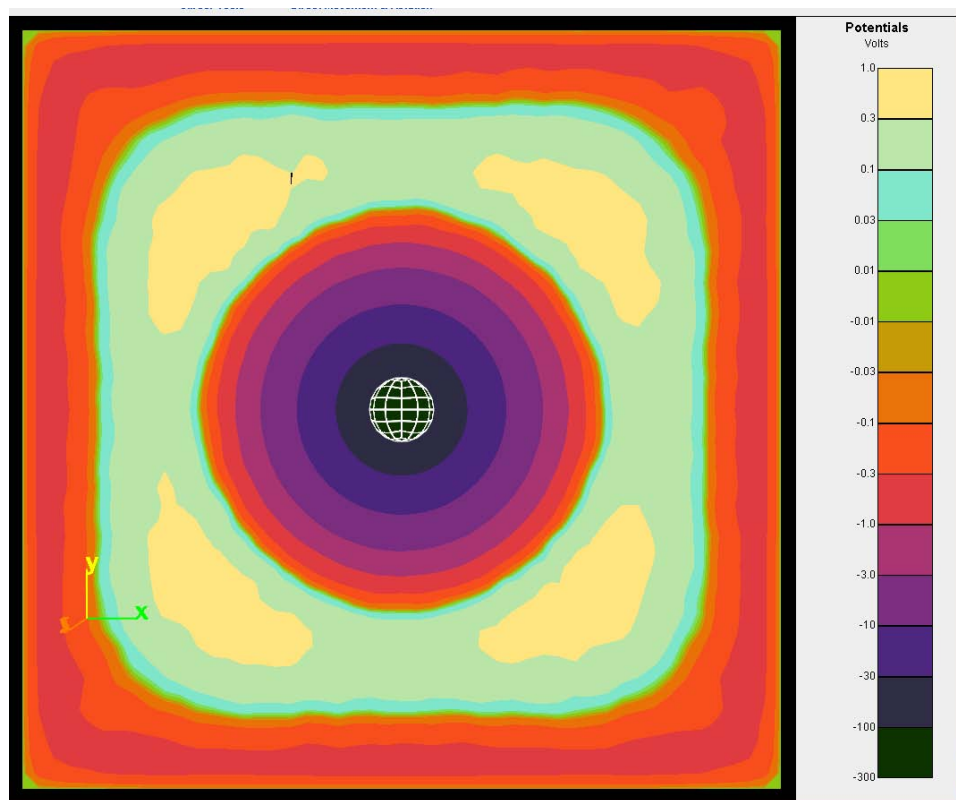
Figure 6. Potentials at 25 µs Corresponding to Figure 5

15

The reason for this behavior is that particles in the field-free region (which does have some small inward field) are initialized with inward velocities comparable to the thermal speed. Convergence of particles moving inward through the field-free region causes the ring of positive potentials, and also explains the higher potentials toward the corners. Also, since particles are moving inward, there is little escaping current.

We changed the code to assign small initial velocities in regions where the fields are small but non-vanishing, while making no change at or within the sheath. The results are shown in Figure 7 and Figure 8. The initial current rise remains as before, because ions within the sheath were initialized in the same way. However, the current drops to a value of about 60 µA, which is much closer to the analytic estimate of 40 µA, especially if we allow for presheath enhancement. The escaping current averages to about 150 µA, which is acceptably close to the analytic estimate of 200 µA. The positive potential region is gone because we have not assigned convergent velocities to the particles in the field-free region. Instead, the initially field-free region has attained a negative potential of about -0.3 V as the ion population is depleted both by being collected and by escaping the grid.
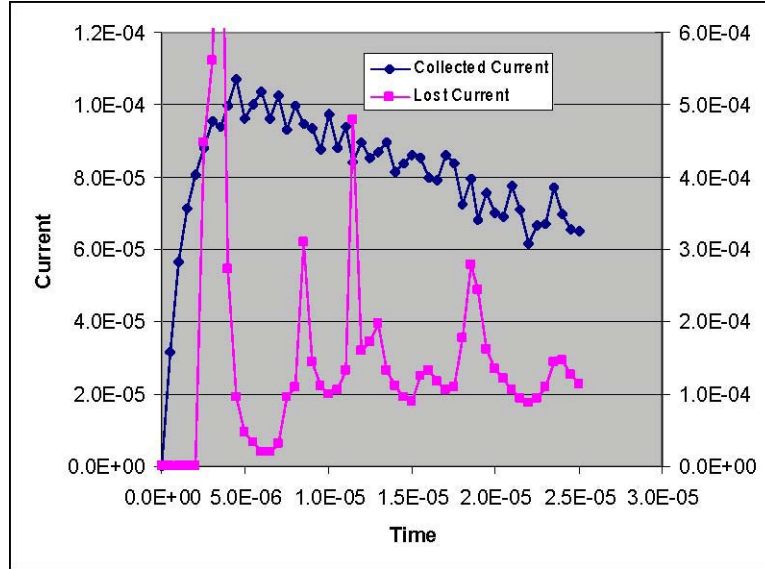
Figure 7. Collected Current (Left Scale) and Escaping (Lost) Current (Right Scale) Using Default Script and Modified INIVEL Velocity Initialization
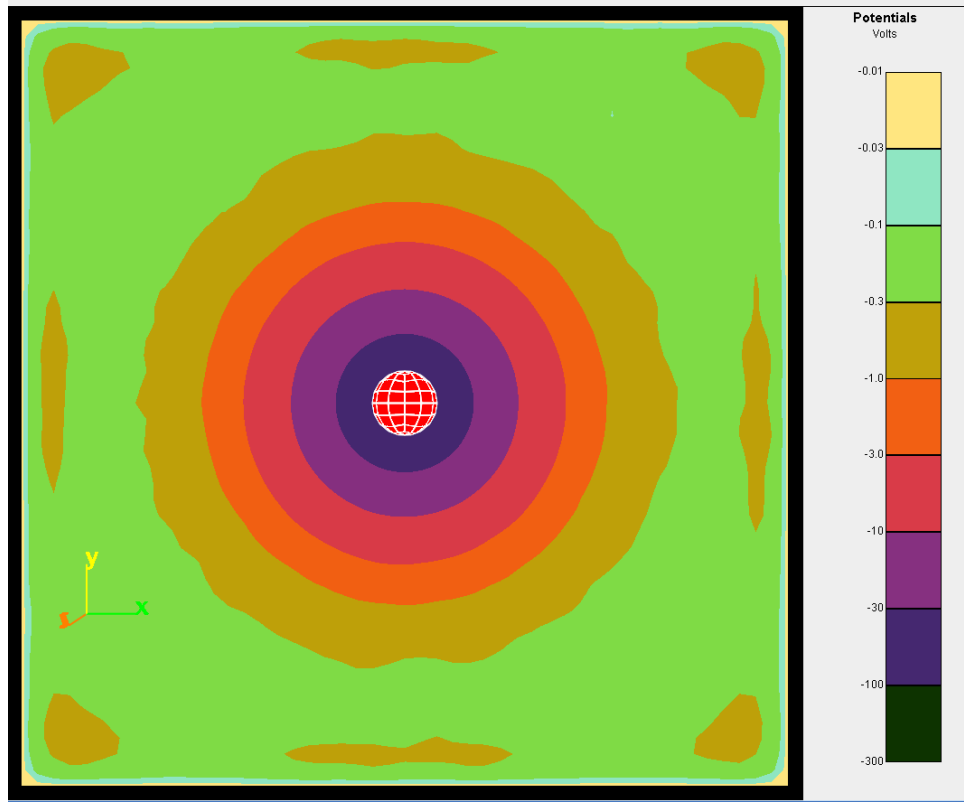
Figure 8. Potentials at 25 μs Corresponding to Figure 7

Finally, in order to perform the calculation intended, we modified the start of the calculation to the following:

1. Initialize the probe to zero potential.

2. Calculate potentials and fields (immediately converging to all zeros).

3. Create (and split) particles. The created particles now have only the velocities that result from the splitting.

4. Reset the probe to -100 V.

5. Recalculate potentials (in Hybrid PIC mode using the created particles).

6. Start tracking.

Results from this calculation are shown in Figure 9 and Figure 10. The results differ from those of the previous calculation only in the slower rise time and lower peak in the current, which occurs because now the ions must be accelerated before they can be collected. Also, the collected current is less noisy.
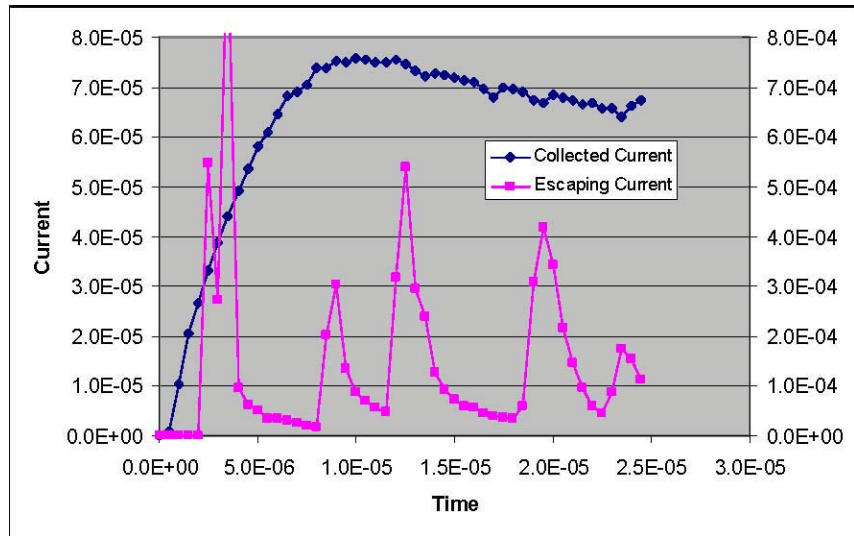
Figure 9. Collected Current (Left Scale) and Escaping Current (Right Scale) after Initializing Velocities by Thermal Splitting Only
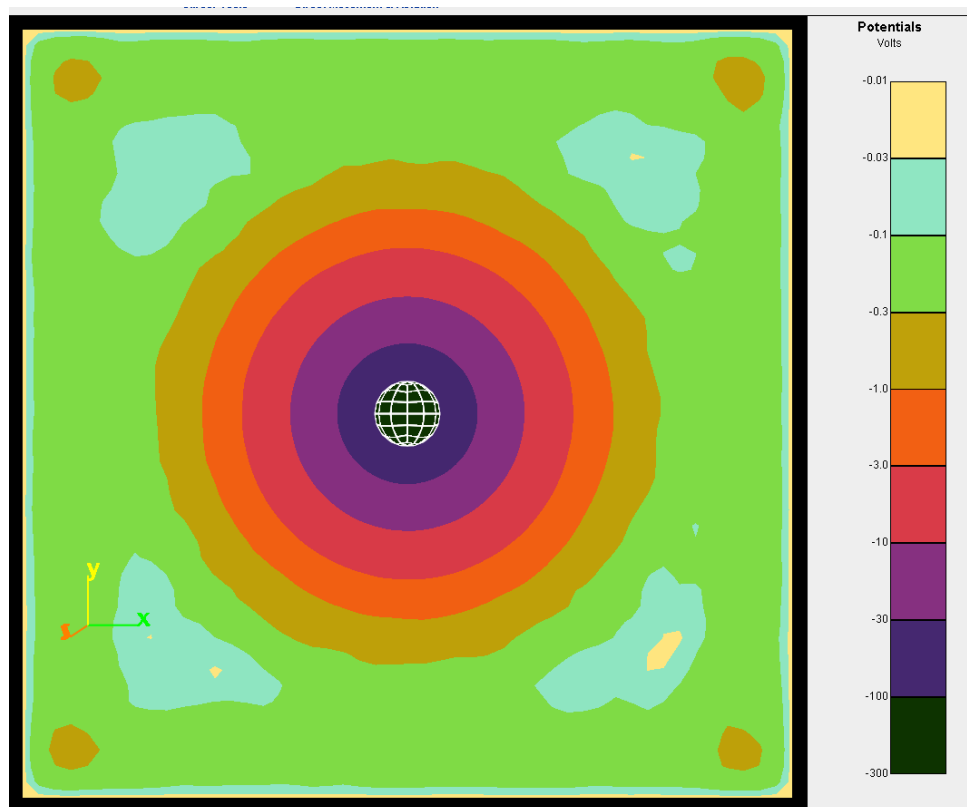
Figure 10. Potentials at 25 µs Corresponding to Figure 9

18

3.4 Boundary Injection

In Figure 11, we note that the field-free region has negative potential mostly in the range of 0.1 to 0.3 V. Presumably, continued collection and escape of ions will lower this potential further. Boundary injection should keep these potentials near zero by replenishing the ions that have been collected or escaped. We implement boundary injection with a new "Create Particles" call at each timestep following the potential solution and preceding the particle tracking. The particle type is "INJECT" and the time interval corresponding to the injection (equal to the timestep if injection is done every timestep) is required in the third field of the "PART_TYPE" input line. As a side effect, the "Create Particles" call results in pruning of the dead and escaped particles, so that injection does not necessarily result in increased particle number.

The implementation is to have an injection point at each quarter-boundary-surface-element. No particle is injected if the electric field directs the particle back towards the boundary. Otherwise, the injected particle has charge equal to the plasma thermal current times the area times the time interval, and velocity equal to $\sqrt{\dfrac{2eT}{\pi m}}$, so that it represents a density of n/2. Optionally, the injected particles can be split into eighths.

Figure 11 shows the collected, escaping, and injected current. The collected and escaping currents are indistinguishable from those seen in Figure 9 without boundary injection; undoubtedly, there would be some divergence if the problem was run longer. The injected current is, on average, slightly greater than the escaping current, and far less than the sum of the collected and escaping currents.
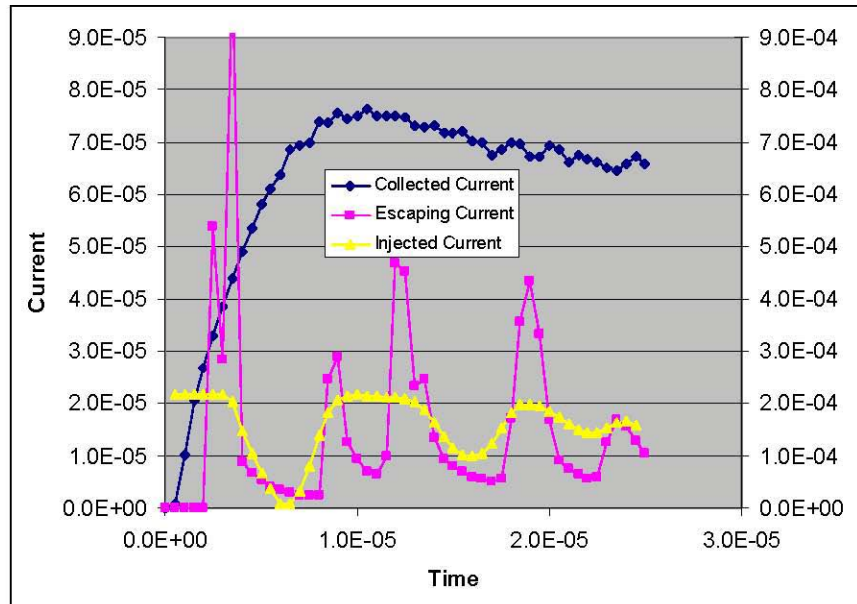
Figure 11. Collected Current (Left Scale), Escaping Current (Right Scale), and Injected Current (Right Scale) Running Problem with Boundary Injection

Figure 12 shows the potentials in the presence of boundary injection. The outermost "clean" spherical contour is at -0.3 V, the same as in Figure 10. In addition, we have a somewhat ragged spherical contour at -0.1 V, and a very ragged (but still recognizable) contour at -0.03 V. The noise in the field-free region is well under ±0.1 V, and mostly under ±0.03 V. By contrast, without boundary injection (see Figure 10) the potential was more negative than -0.1 V in nearly all the field-free region, with islands more negative than -0.3 V near the corners.
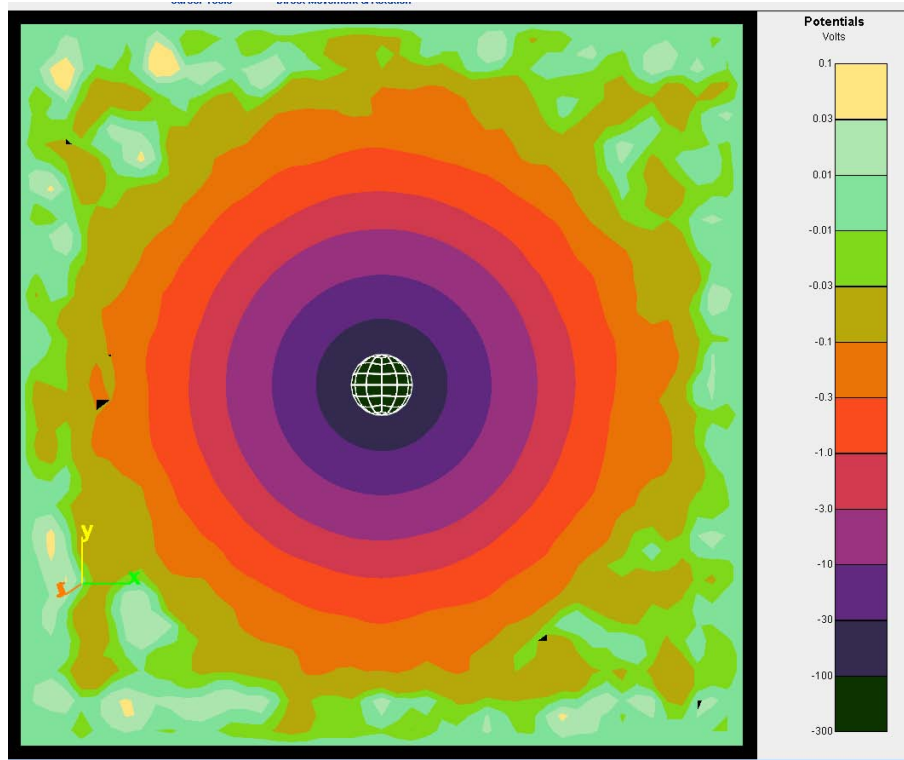
Figure 12. Potentials at 25 µs Corresponding to Figure 9 (Compare with Figure 8)

We next experimented with splitting the boundary injected particles. Figure 13 compares the results using split and unsplit injected ions, run for 50 µs. The collected current shows no significant difference. However, the escaping current at late times is significantly higher (and thus closer to the expected value of 200 µA) when the particles are split.

The difference between split and unsplit injection is more apparent in the final potential contours. Split injection (Figure 15) shows a transition from a spherical contour at -0.3 V to a square contour at -0.1 V, and thence a nearly noiseless path to the problem boundary. Without splitting (Figure 14), the -0.3 volt contour is already beginning to square, and from there to the boundary, there is very noticeable, albeit low-level, noise.

The minor improvement resulting from particle splitting comes at considerable cost. From an initial particle count of 2.4 million, the run with unsplit boundary injection has its particle count decrease to 1.5 million at 50 µs, while the run with split boundary injection sees an increase to 8.1 million at 50 µs.
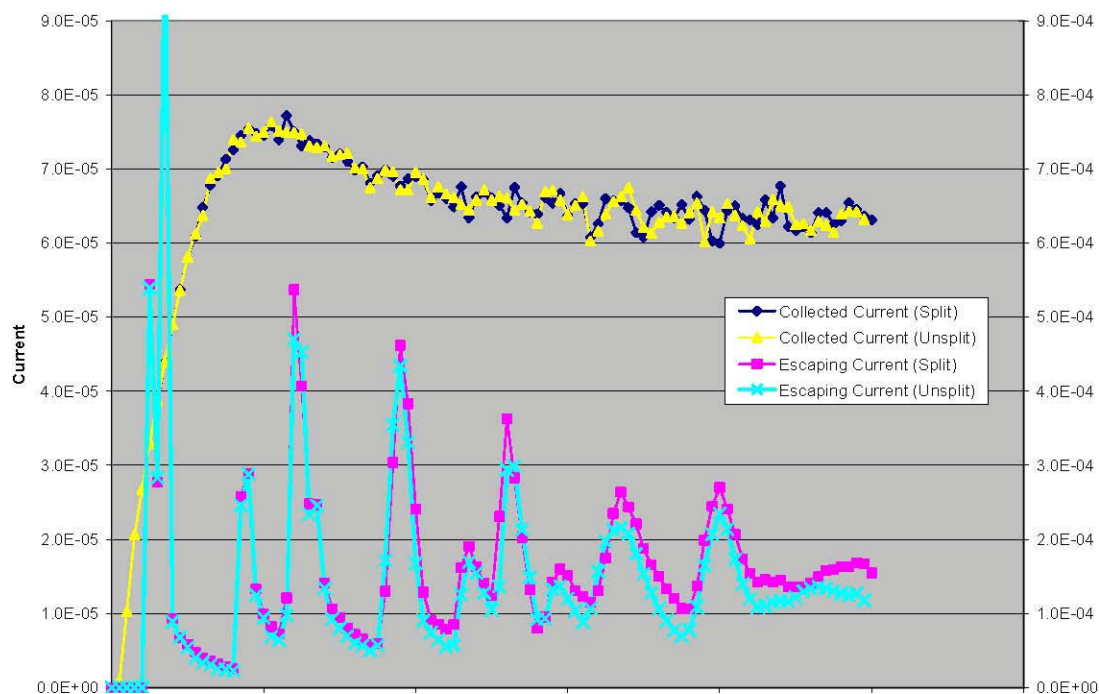
Figure 13. Collected (left scale) and Escaping (Right Scale) Currents for Calculations in which the Boundary Injected Ions are Split or Unsplit
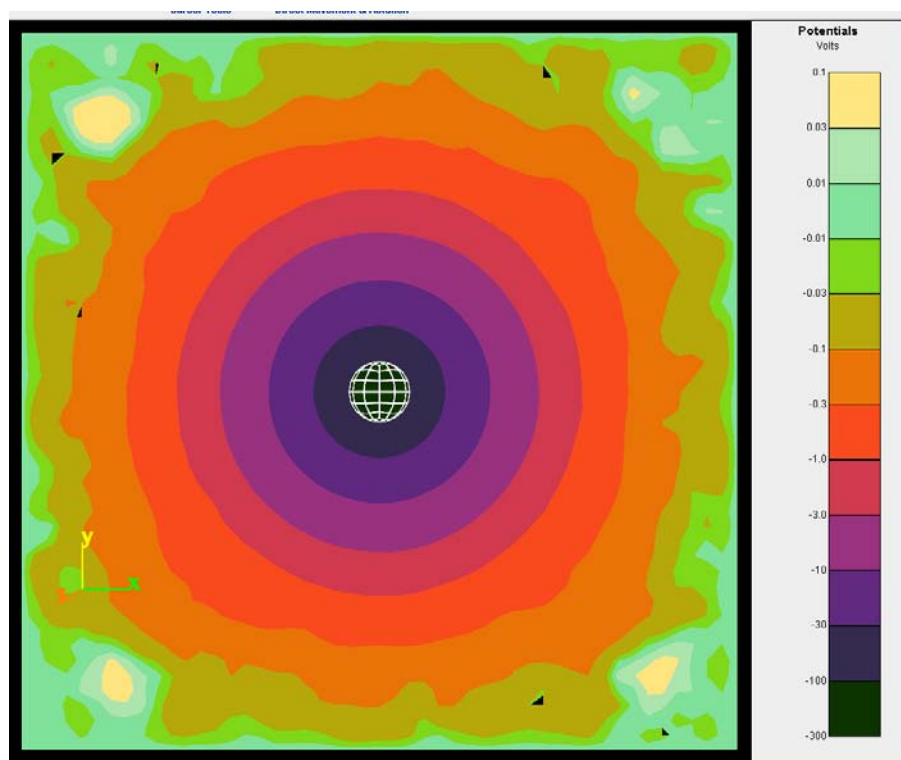
Figure 14. Potential Contours after 50 µs for Unsplit Boundary Injected Ions
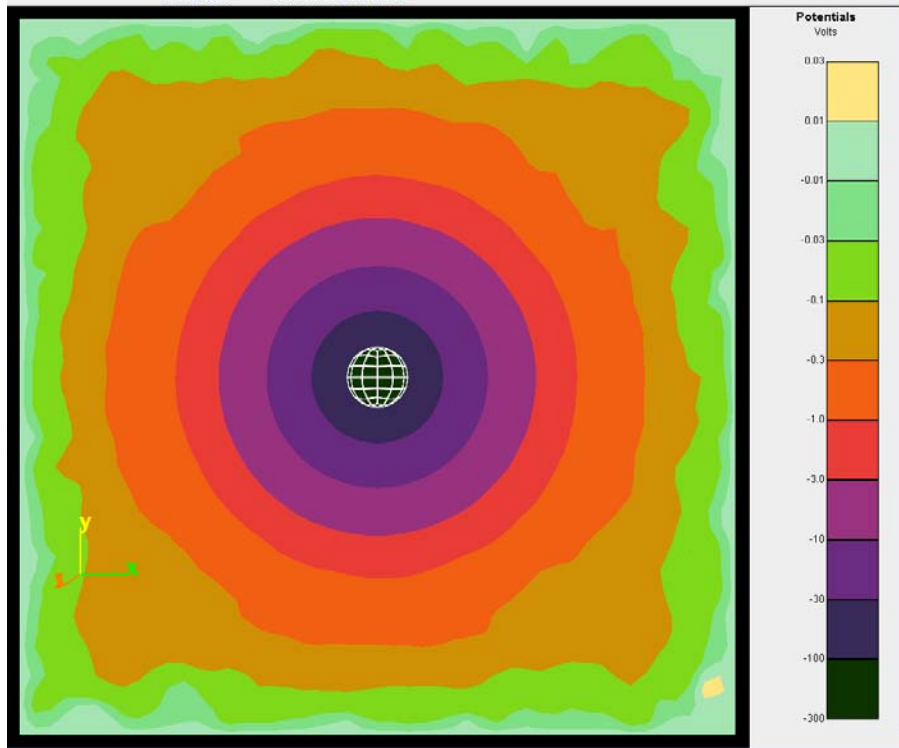
Figure 15. Potential Contours after 50 μs for Split Boundary Injected Ions

3.5 Splitting on Entering a Finer Grid

The real reason for assigning temperatures to particles is so that they can be split repeatedly in mid-flight. Figure 16 shows a quadrant of particles after 9 μs. The particles are initially unsplit, and the code parameters (see below) are set such that ions will be split into nine or twenty-seven particles on entering a finer grid. In Figure 16, ions can be seen entering Grid 2 from Grid 1 at the top and right. Because these ions are moving slowly, they are split both along and normal to their motion direction. By this time, all ions originating in Grid 3 have been "eaten" by the sphere, so that the cloud of ions currently in Grid 3 has entered from Grid 2 and been split. Those that entered most recently were already drifting significantly when they were split, and were thus split only normal to their direction of motion, as described above.
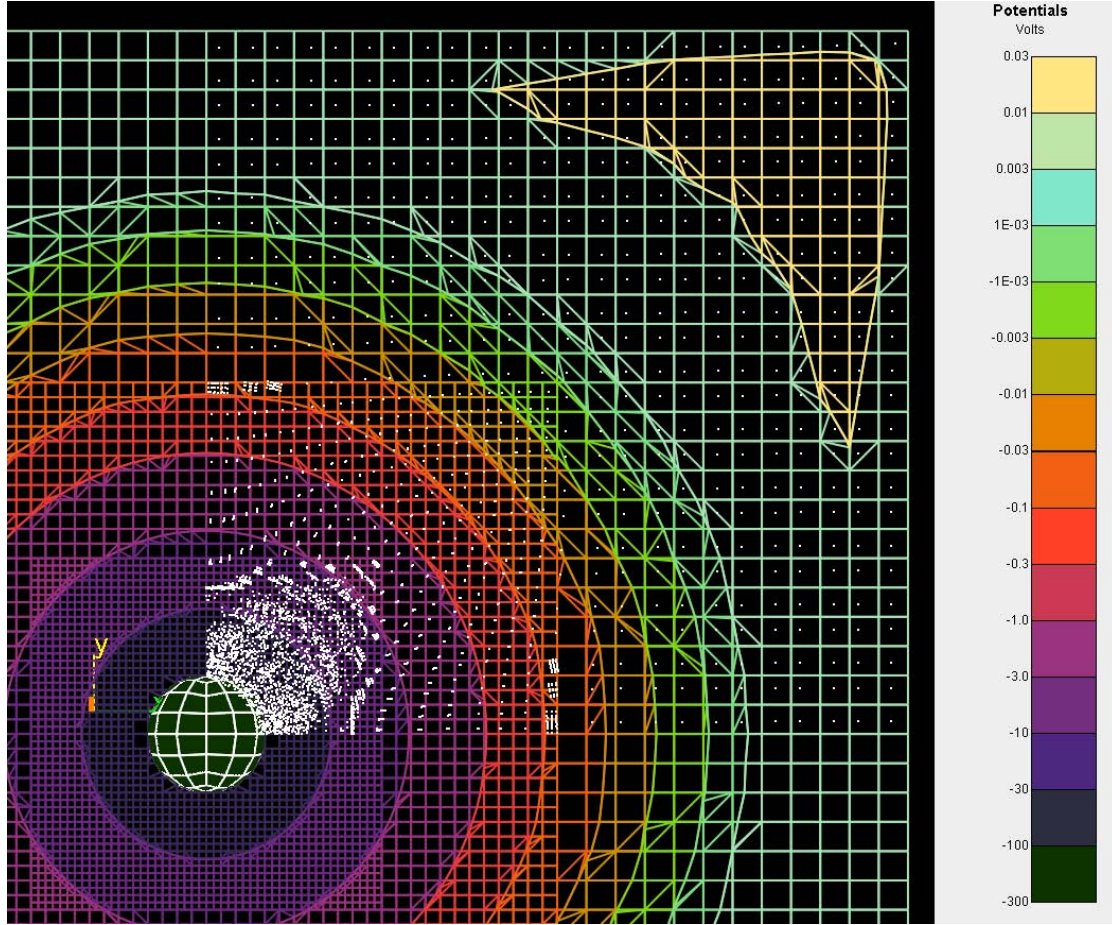
Figure 16. Particle Positions after 9 μs when Particles are Split on Entering a More Finely Resolved Grid

3.6 Moving Frames

It is important to be able to split and inject particles for cases when the spacecraft is moving through the plasma. The calculation is performed in the spacecraft frame (plasma moving with "ram flow"), while the temperature is measured in the plasma frame. Therefore, to split particles requires transforming the velocity from the spacecraft frame to the plasma frame, applying the splitting algorithm outlined above, and re-transforming velocities of split particles back to the plasma frame.

When injecting particles, we compare the inward component of the ram velocity with the usual injection speed, $\sqrt{\dfrac{2eT}{\pi m}}$. If the ram component is greater than the usual injection speed, then we always inject with the ram velocity. Otherwise, the injection velocity is determined by adding the stationary injection velocity to the ram velocity; if this is inward, then we inject only when the electric field is attractive. The weight of the injected particles is calculated from the inward normal component of the vector sum of the ram current and the thermal current. The current and velocity are related in such a way that the density contribution of the injected particles varies from half the ion density for a stationary object to the full ion density for a high mach number object.

Figure 17 shows a hybrid PIC calculation (with no particle splitting) of O+ flow past an uncharged sphere moving at LEO velocity in the (1,1,0) direction. (Geometry and other parameters are the same as used thus far in the document.) Clearly seen are the negative potentials in the object wake and the boundary between the injected particles (diagonal pattern) and the original particles (square pattern). Potential fluctuations on the order of 0.05 V are seen in the first subdivided grid where it is populated by outer grid ions.
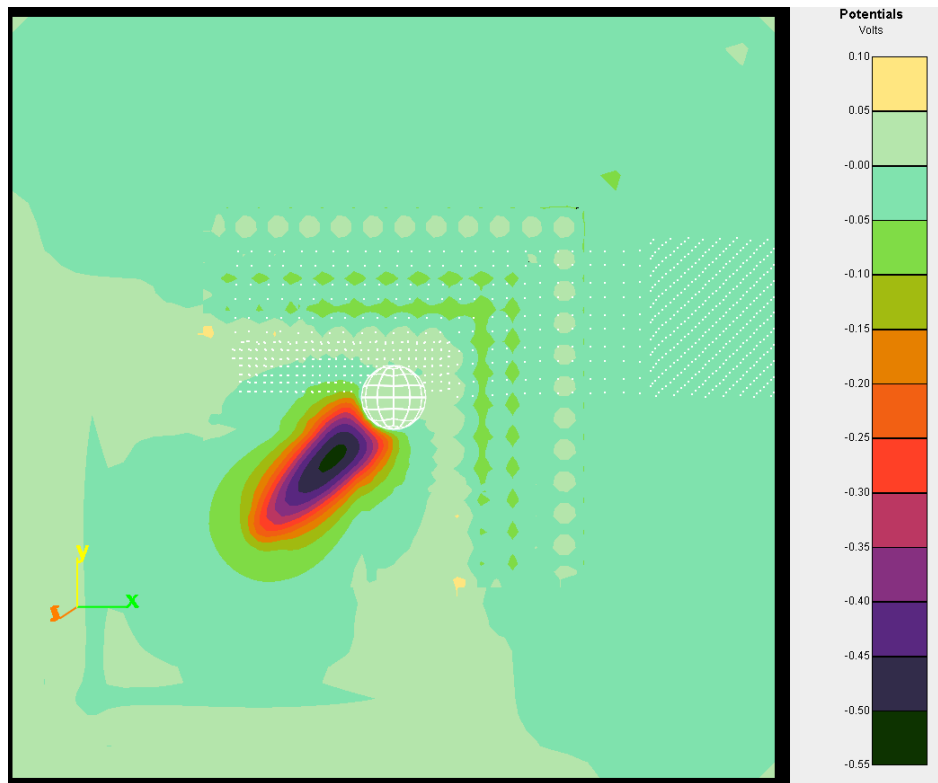
Figure 17. Potentials and Ion (O$^+$) Macroparticles after 80 μs for an Uncharged Sphere Moving in the (1,1,0) Direction (No Splitting of Macroparticles)

Figure 18 shows a similar calculation, now with the sphere once again charged to -100 V. After 80 μs, ions are focused in the wake with sufficient strength to create positive potentials of approximately one volt. This structure persists, as shown in Figure 19, where the potential maximum in the wake has reached nearly the ram energy.
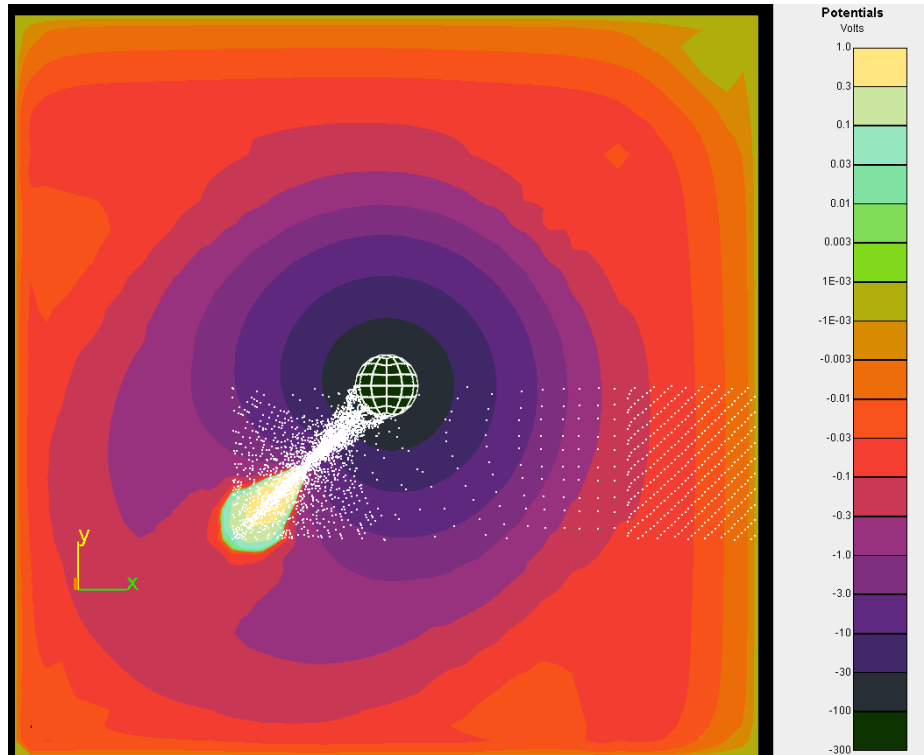
Figure 18. Potentials and Ion (O$^+$) Macroparticles after 80 μs for a Sphere Charged to -100 V Moving in the (1,1,0) Direction (No Splitting of Macroparticles)
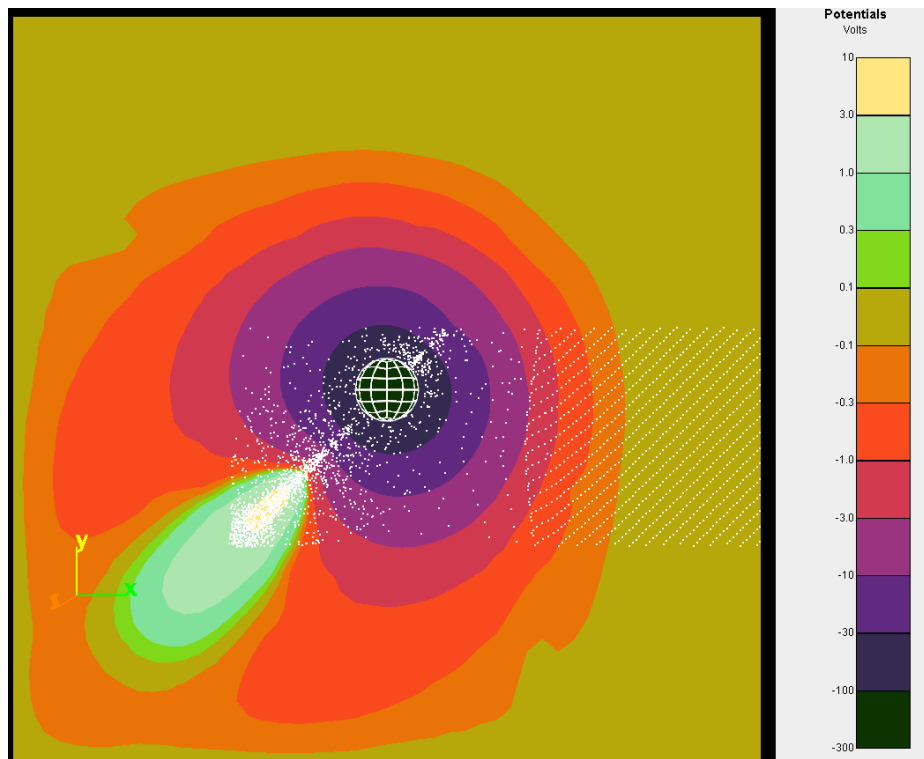
Figure 19. Same Calculation as Figure 18 after 136 μs

Figure 20 shows the charged sphere calculation, now with particles split on entering a refined grid. While the general character of the result is the same, the potentials are much smoother and now show compression of the sheath on the ram side. Figure 21 shows the current to the sphere. After an early peak to nearly 16 µA, the current settles down to a value of fewer than 7 µA, comfortably less than the orbit-limited value of 8 µA. Of course, this improved fidelity comes at a price, with a final particle count in excess of two million in Figure 20, versus under 0.4 million in Figure 19.
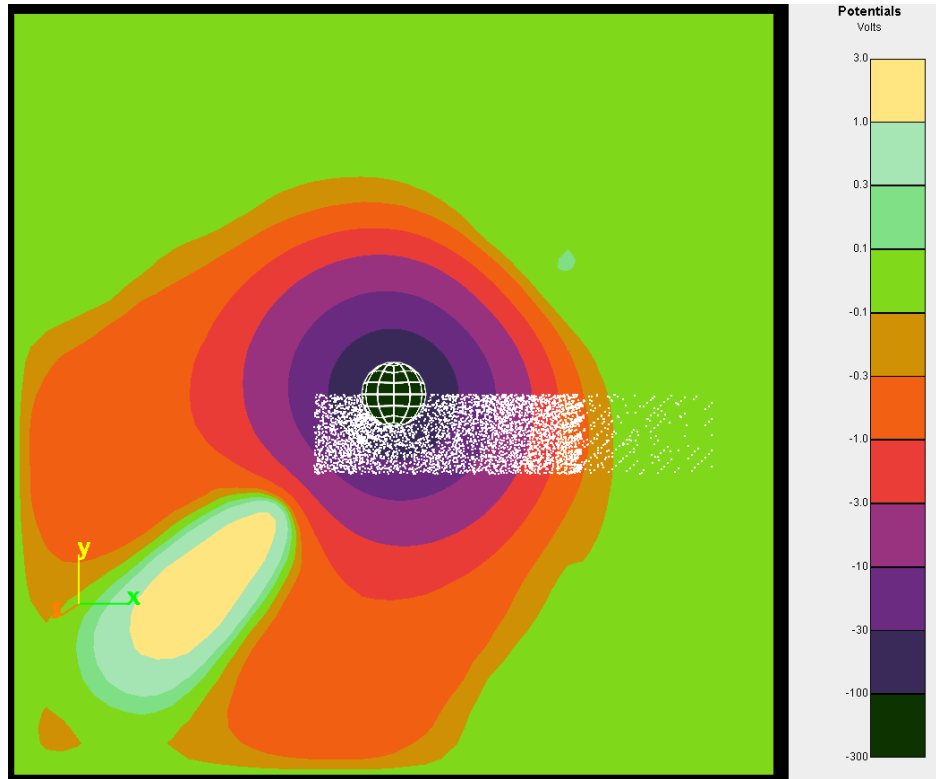
Figure 20. Potentials and Ion (O$^+$) Macroparticles after 160 µs for a Sphere Charged to -100 V Moving in the (1,1,0) Direction – Particles Split on Entering Refined Grid
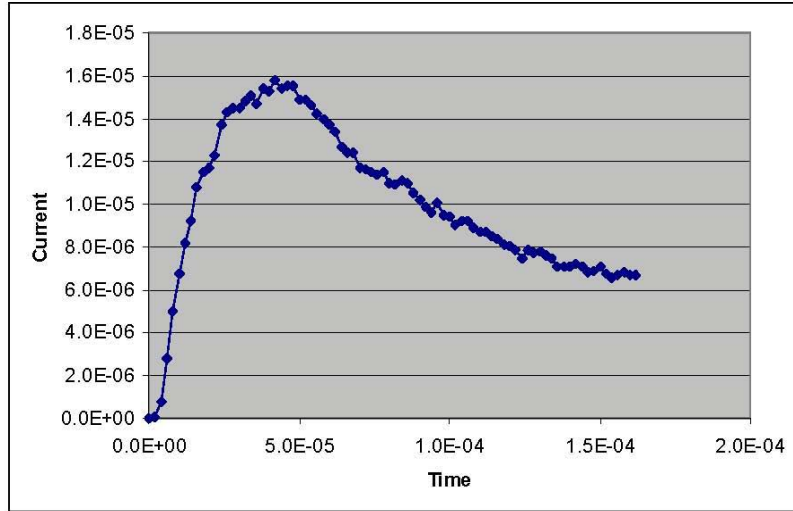
**Figure 21. Current for Sphere Charged to -100 V Moving in the (1,1,0) Direction –
Particles split on Entering Refined Grid**

4. PARTICLE-IN-CELL/CHARGING CALCULATIONS IN *NASCAP-2K*

We made several modifications to *Nascap-2k* to simplify and enhance time-dependent calculations in which the tracked current is used to compute the change in potential of spacecraft surfaces.

New options have been added to the **Problem** tab. Time-dependent problems may be specified as either "Fixed Surface Potentials" or "Self-Consistent Surface Potentials." If "Self-Consistent Surface Potentials" is chosen, either "Tracked Particle Currents Only" or "Tracked Ion & Analytic Electron Currents" can be selected. "Time-Dependent Plasma" calculations with "Fixed Surface Potentials" are calculations of surface currents as a function of time for user specified surface potentials. "Time-Dependent Plasma" calculations with "Self-Consistent Surface Potentials" are the same, with the addition of a charging step. The surface charging is computed either with only the tracked current ("Tracked Particle Currents Only") or with both the tracked current and an analytic electron current ("Tracked Ion & Analytic Electron Currents"). If the second option is chosen, then an environment is set in the charging calculation and an electron current that is a function of the surface area, the electron thermal current, the surface potential, and the plasma temperature is added to each surface when computing the potential.

$$I = \begin{cases} Aj_{th} \exp\left(\phi/\theta\right) & \text{if } \phi \le 0 \\ Aj_{th}\left(1 + \dfrac{\phi}{\theta}\right) & \text{if } \phi > 0 \end{cases} \qquad [1]$$

27

If "Self-Consistent Surface Potentials" is chosen, the default script is as follows and is similar to that used for a LEO charging problem. The **SetEnvironment** command is only included for "Tracked Ion & Analytic Electron Currents." The **ZeroCurDerivAlgorithm** command specifies that the change in potential due to the tracked current in a single timestep is calculated using an explicit algorithm rather than an implicit one. The change in the current due to the change in potential during the timestep is not included when calculating the potential change. The **DoTrackTimeStep** command is the same as the **DoOneTimeStep** command, except that the "Timestep" is the "Tracking time per timestep" on the **Advanced Particle Parameters** dialog box.

```
Charge_Surfaces
        ReadObject
        OpenDatabase
        SetInitialConductorPotentials
        SetInitialPotentials
        WritePotentials
Embed_Object_in_Grid
Potentials_in_Space
Create_Particles
Track_Particles
Charge_Surfaces
        OpenDatabase
        InitializeCalculation
        SetEnvironment
                Environment
                        type  LEO
                        ne1   densityvalue
                        te1   temperaturevalue
        UseTrackedCurrents
        ZeroCurDerivAlgorithm
        PrepareChargeMatrix
        DoTrackTimeStep
Potentials_in_Space
Track_Particles
Charge_Surfaces
        OpenDatabase
        InitializeCalculation
        SetEnvironment
                Environment
                        type  LEO
                        ne1   densityvalue
                        te1   temperaturevalue
        UseTrackedCurrents
        ZeroCurDerivAlgorithm
        PrepareChargeMatrix
        DoTrackTimeStep
Potentials_in_Space
Track_Particles
.....
```

The plasma density and temperature appear in the locations indicated by italics. The value of the "UpdateTime" keyword in the "Track_Particles" command is "No."

The tracked current density appears to be zero on the **3D Results** tab after running the **Charge Surfaces** module because the tracked current is associated with the previous timestep and only the present timestep is displayed. The charging current density (which for this calculation is the tracked current density) is associated with the present timestep and therefore can be displayed. Contributions to the net current from photoemission and secondary electrons are ignored. Under some conditions, both of these terms can be important.

A number of minor changes were made to the way the histories of potentials and currents are saved in order to avoid the display of possible confusing results. The two most visible changes are initialization of the current arrays when the "SetInitialPotentials" command is executed and the saving of the initial surface potentials and currents. Results for time "0.0" are now displayed on the **Results** tab.

There are two aspects of the calculation to be verified. First, that the current to surfaces computed during tracking is used to compute the change in potential and, second, that the current is being used correctly in the calculation of the change in surface potential. The following calculations were used to verify that both of these calculations are done as anticipated.

4.1 Discharge Conducting Sphere of Known Capacitance

The statement of the test case is as follows:

Object: 0.1-m radius "sphere" shown in Figure 22.

Environment: 10^{10} m^{-3}, 1 eV

Initial potential: -100 V

Space potentials: Hybrid PIC charge density model

Particles: Initialize with uniform distribution of Hydrogen ions, 5×10^{-7} s timestep

Charging: Fifty steps of above script without Environment specification.
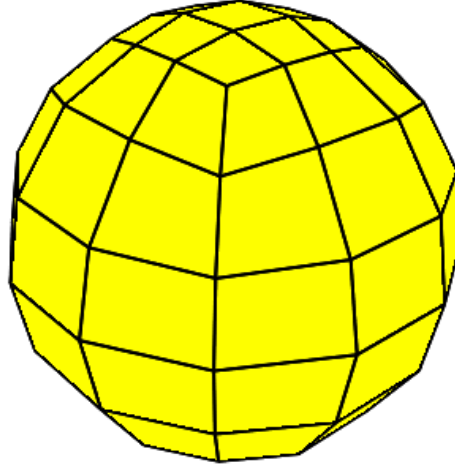
Figure 22. Sphere Object Used in Example

The current collected at each timestep is shown in Figure 23. The tracked current is that printed out by the **Track Particles** module and the charging current is that stored by the **Charge Surfaces** module. This figure verifies that the current deposited on surfaces by the **Tracked Particles** module is used by the **Charge Surfaces** module to compute the change in the surface potentials.
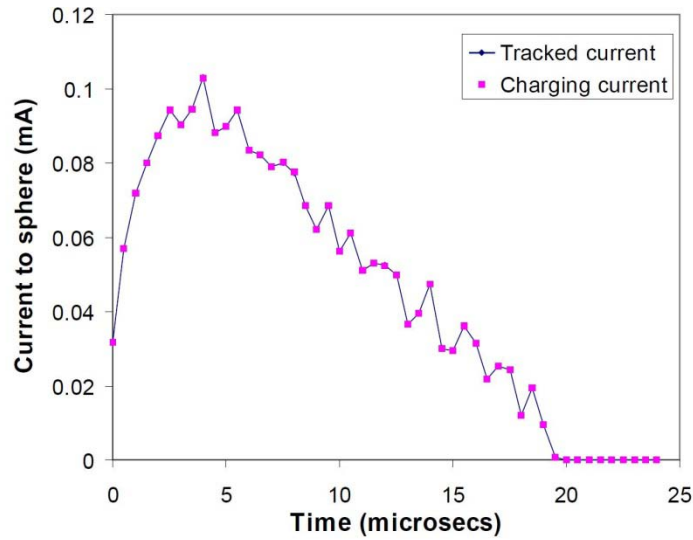
Figure 23. Current Collected at Each Timestep in Discharge Calculation

The change in potential of a sphere of radius r in vacuum due to an incident current I during a timestep of length τ is given by $\Delta\phi = \dfrac{I\tau}{C}$ where $C = 4\pi\varepsilon_o r$. Figure 24 compares the potential computed by *Nascap-2k* with the potential computed from the capacitance of a sphere of radius 0.1 m and the current shown in Figure 23. The figure also shows the potential computed for the capacitance of a sphere of radius 0.09285 m.
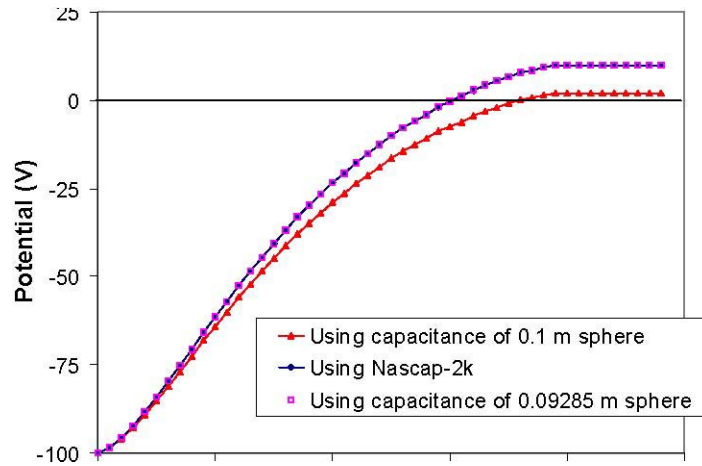
Figure 24. Potential of Sphere During Discharge

The ion current to the sphere does not stop immediately when the sphere goes positive. The ions continue to move toward the sphere, and to be collected, due to the particle momentum. When the electric field is high enough for long enough, the ions are all moving away from the sphere and the current goes to zero. The sphere potential stays constant after this. In real plasma, the more mobile electrons would almost completely eliminate the overshoot effect.

The positions of macroparticles for Z values between 0.0 m and 0.03 m at 5 µs, 10 µs, 15 µs, 20 µs, and 25 µs, are shown in Figure 25 through Figure 29. In the first figure, the positive ions can be seen moving toward negative potential sphere. The ions continue to move toward the sphere until the sphere potential is positive enough long enough for the ions to begin moving away from the sphere.
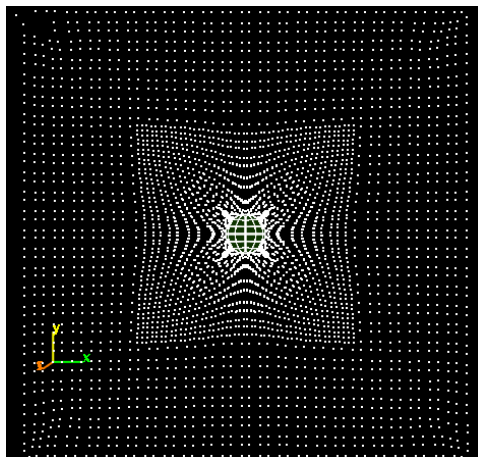
Figure 25. Positions of Macroparticles for Z Values Between 0.0 and 0.03 m at 5 µs. Particles within Sheath Moving Toward Sphere
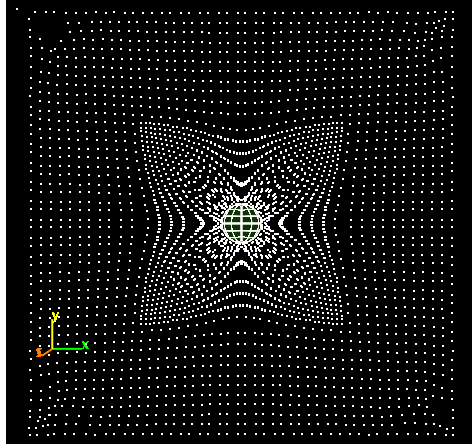
Figure 26. Positions of Macroparticles for Z Values Between 0.0 and 0.03 m at 10 μs
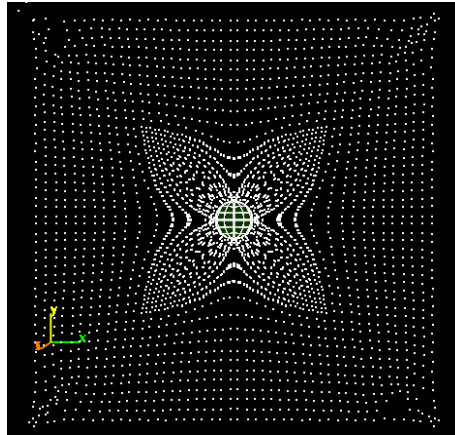
**Figure 27. Positions of Macroparticles for Z Values Between 0.0 and 0.03 m at 15 μs
Surface Potential Near Zero – Particles Moving Toward Sphere**
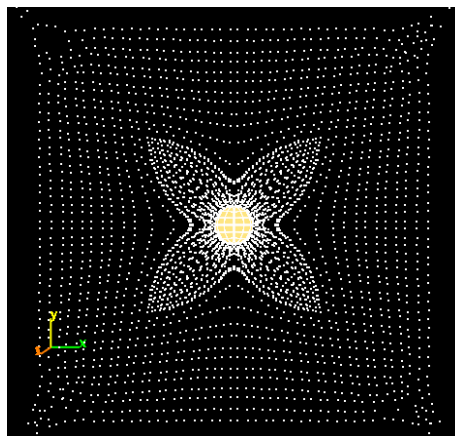
**Figure 28. Positions of Macroparticles for Z Values Between 0.0 and 0.03 m at 20 μs
Surface Potential Positive – Current Goes to Zero as Potentials Overcome Particle
Momentum**
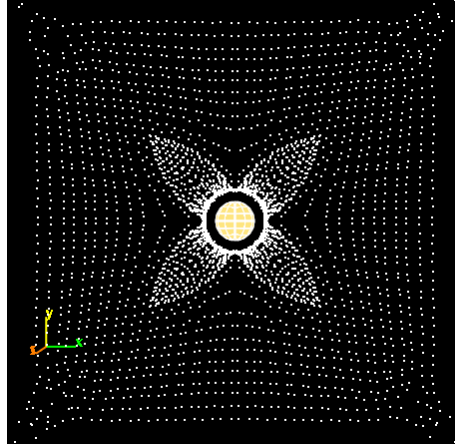
Figure 29. Positions of Macroparticles for Z Values Between 0.0 and 0.03 m at 25 μs Particles Moving Away from Positive Potential Sphere

The results of repeating the above calculation with the inclusion of the electron current are shown in Figure 30 and Figure 31. Without the contribution of the electron current, the sphere rises to nearly 10 V positive before the ion current drops to zero. With zero incident current, the sphere potential remains at 10 V positive. With the electron current, the total current drops to zero as the potential becomes positive, and the potential is held near zero by the incident electrons. The ion current remains fairly constant rather than dropping to zero, as the ions are no longer repelled. Since the ion current is, on average, slightly less than the raw electron thermal current, the potential, on average, is slightly negative.
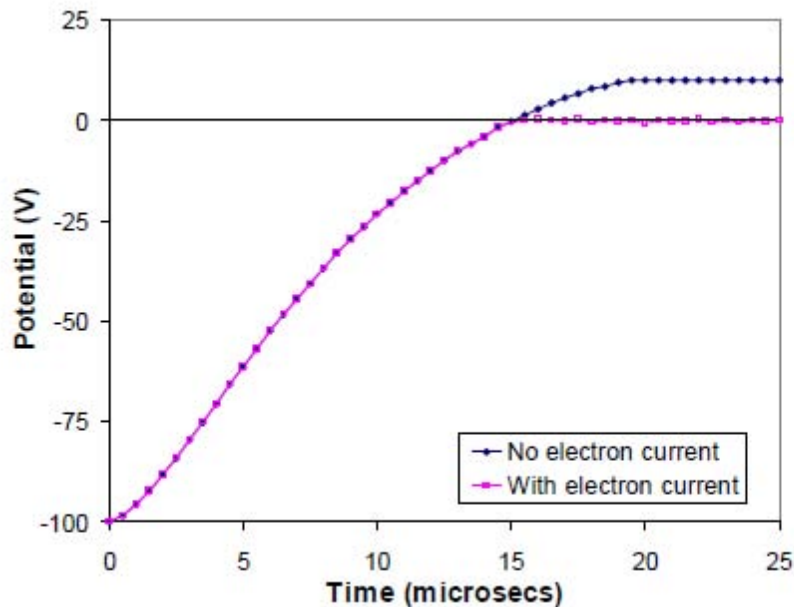
Figure 30. Comparison of Sphere Potential During Discharge with and without an Analytic Electron Current Included in the Calculation
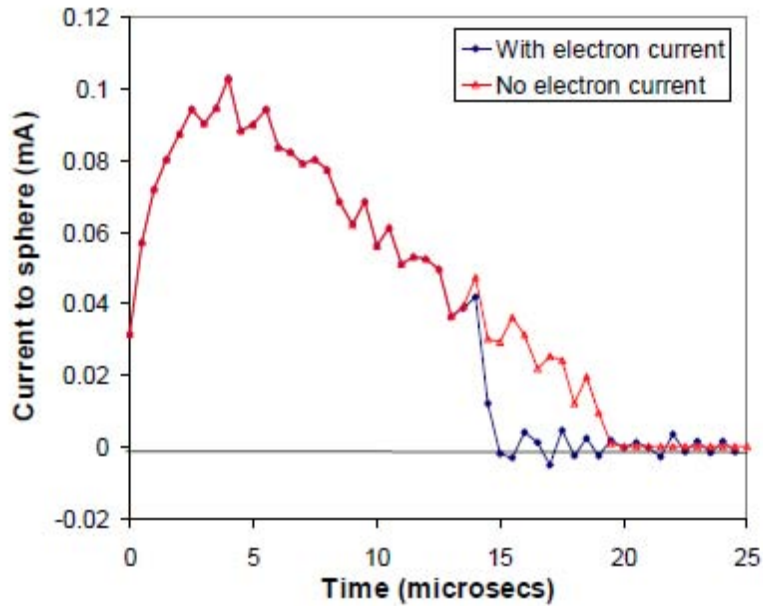
Figure 31. Comparison of Current Collected at Each Timestep in Discharge Calculation With and Without an Analytic Electron Current Included in the Calculation

4.2 Differential Charging of Insulating Sphere Surface

The statement of the test case is as follows:

Object: 0.1-m radius Teflon "sphere" with the same geometry as shown in Figure 22. A dielectric constant of 2 and a thickness of 0.1 m (completely unphysical) were used to make the capacitance across the Teflon near the capacitance to infinity.

Environment: 10^{10} m^{-3}, 1 eV

Underlying conductor potential: Fixed at -100 V

Space potentials: Hybrid PIC charge density model

Particles: Initialize with uniform distribution of Hydrogen ions, 5 x 10^{-7} s timestep

Charging: Thirty steps of above script with the addition of a "FixGroundPotential" command with an argument of -100 V.

The current collected at each timestep is shown in Figure 32. The tracked current is that printed out by the **Track Particles** module and the charging current is that stored by the **Charge Surfaces** module. A surface area of 0.121 m^2 is used to make these currents match.

34
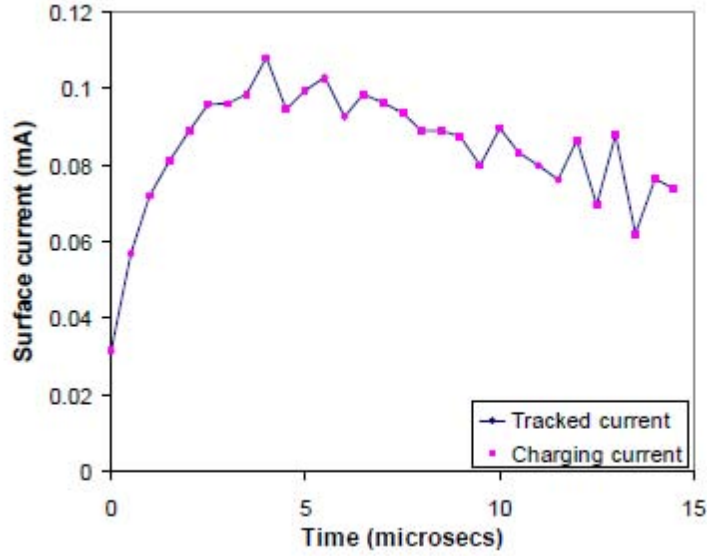
Figure 32. Current Collected at Each Timestep in Discharge Calculation

The capacitance between the surface and infinity and the capacitance between the surface and the underlying conductor are in parallel, therefore, the capacitance that controls the charging of each Teflon surface is their sum. The capacitance to the entire surface is then the sum of the contributions of each surface and equals the capacitance between the sphere and infinity, $C = 4\pi\varepsilon_o r$, and the capacitance between the surface and the underlying conductor, $C = \kappa\varepsilon_o A/d$, where κ is the relative dielectric constant of the Teflon, A is the surface area, and d is the thickness of the Teflon.

Figure 33 compares the potential computed by *Nascap-2k* with the potential computed from the ideal capacitance and the current shown in Figure 32.
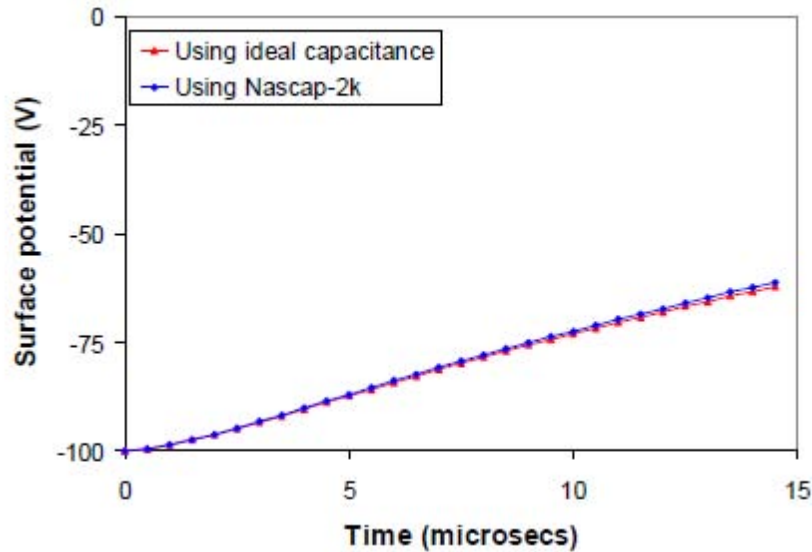
Figure 33. Potential of Sphere During Discharge
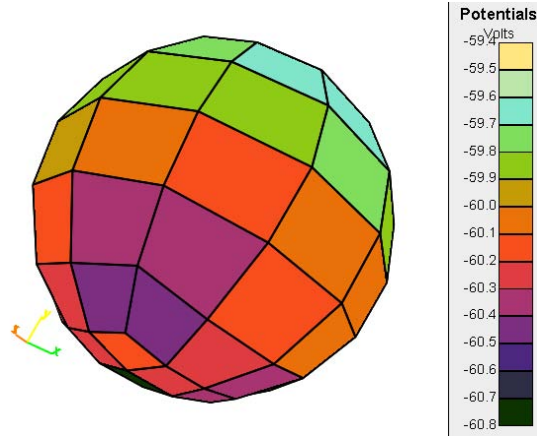
Figure 34. Surface Potentials on Insulating Sphere after 15 μs

4.3 Further Work

Two additional features to the analytic electron current should be considered.

1. Consider the electron collection for positive potentials. Presently it is enhanced by the three-dimensional orbit limited (1+V/T). However, for short Debye length it should not be enhanced. Also, there are cases where the two-dimensional formula (something like $(1+V/T)^{1/2}$) would be more appropriate.

2. In some significant cases (e.g., VLF antenna) electron collection by the positive surfaces is blocked by the negative potential sheath. There ought to be a way to approximate this effect using the electric field and maybe the Debye length, but it is not obvious.

The inclusion of the contributions to the net current from photoemission and secondary electrons should be considered.

5. SELF-CONSISTENT POTENTIALS AND CHARGE DENSITIES FOR CHAWS PROBLEM USING HYBRID PIC APPROACH

In the 1990s we developed a technique to self-consistently compute the potentials and charge densities about the Wake Shield Facility, a free flying shuttle payload, with the biased CHAWS probe. The technique, referred to as the full trajectory approach, is to iteratively solve for potentials and ion charge densities. First space potentials are computed. Then a thermal distribution of macroparticles representing ram ions is tracked from the problem boundaries. Each macroparticle is tracked until it either leaves the computational space or hits a surface. At each step, charge is deposited into the volume element containing the macroparticle at the end of the step. After all of the macroparticles are tracked, the resulting charge density is used to solve Poisson's equation for the space potentials. Ion charge densities and potentials are iteratively computed until a steady state solution is reached. To reach convergence, we found that at each step it is necessary to use a charge density composed of 70% of the previous charge density and 30% of the most recently computed charge density. A similar sharing of candidate potential solutions within a single potential computation is also done. The potentials and charge densities that result from this computation are shown in Figure 35 and Figure 36.

Figure 35. Potentials in Space for CHAWS Problem – Self-consistent Potentials and Charge density Computed Using Full Trajectory Approach

Figure 36. Ion Charge Densities for CHAWS Problem – Self-consistent Potentials and Charge Density Computed Using Full Trajectory Approach

Several improvements have been made to *Nascap-2k*'s particle-in-cell capabilities, such that now the same problem can be solved using a Hybrid PIC approach. The original implementation of the charge stabilization approach for the solution of potentials in Hybrid PIC problems was found to be inadequate. With the implementation of **N2kDB**, we are able to save both nodal and volume charge densities, which allows us to compute the electron charge density, including charge stabilization, for a Hybrid PIC problem using the same formulas as for the full trajectory approach.

Using the new formulation for computing the electron contribution to the charge density with charge stabilization, we found that while the solution is convergent, the tracked ions contribute little to the charge density behind the WSF disk. This is because the method originally developed to inject macroparticles at the problem boundary in the full trajectory approach does a better job capturing the wings of the thermal distribution and creates a higher density of macroparticles near the disk edge than does the method originally developed for Hybrid PIC problems.

Another improvement to the standard Hybrid PIC approach is "orbit averaging." In this approach, rather than depositing charge to the nodes for the ion density contribution of the charge density and to volume elements for the computation of the electron contribution to the charge density and the charge stabilization at each timestep, charge is deposited at each substep of the trajectory and accumulated through the timestep. This allows for timesteps longer than the time to cross a single volume element. Using orbit averaging, the charge density behind the disk is represented a little better, although the plasma still fills the wake too quickly on the side away from the probe. In addition, the potential solution is less well behaved. The results for the above approaches were reported in the May-August 2009 quarterly report, with plots of potential and ion charge densities illustrating the behavior described above.

Recently, the flexible macroparticle specification coding, originally developed for full trajectory calculations, was modified so that it can also be used in Hybrid PIC calculations. Note that presently, the new thermal distribution splitting capability is inconsistent with the other particle splitting algorithms. With a better representation of the thermal distribution and a spatial particle distribution with increased density of macroparticles near the disk edge, the potentials and charge densities computed using the Hybrid PIC approach are closer to those obtained using the full trajectory approach. The results are shown in Figure 37 and Figure 38, with noticeably increased agreement with the results of the full-trajectory approach (see Figure 35 and Figure 36) as compared to previous efforts.
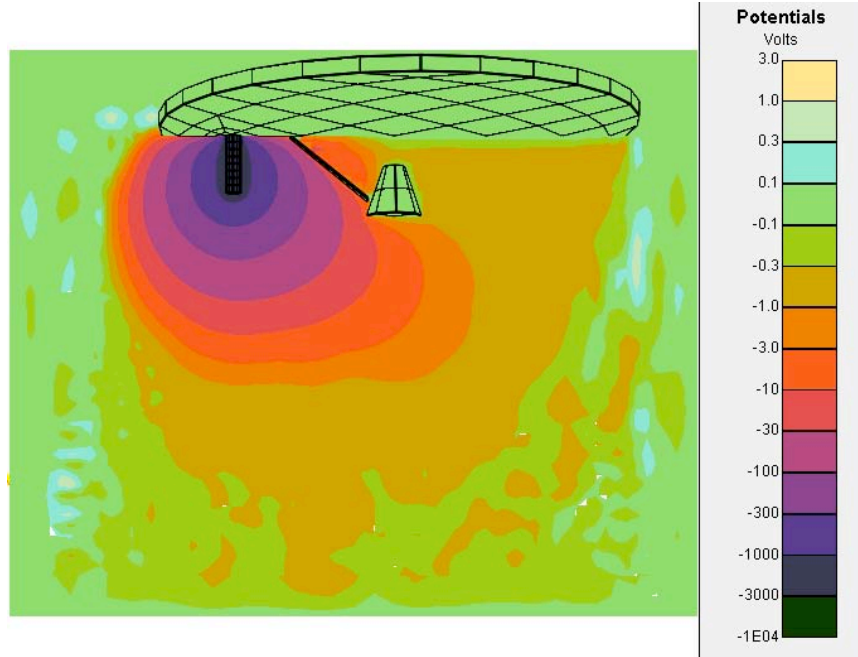
Figure 37. Potentials in Space for CHAWS Problem – Self-consistent Potentials and Charge Density Computed Using Hybrid PIC with Orbit-averaging Approach with a 5 µs Timestep, after 1000 Timesteps (5 ms)
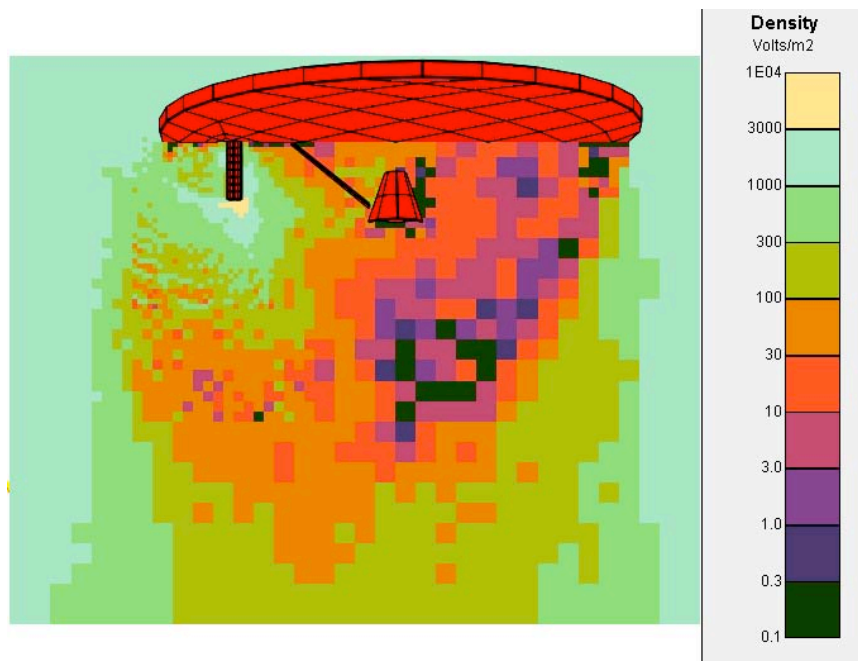
Figure 38. Ion Charge Densities for CHAWS Problem – Self-consistent Potentials and Charge Density Computed Using Hybrid PIC with Orbit-averaging Approach with a 5 µs Timestep, after 1000 Timesteps (5 ms)

With orbit averaging, the results of this static problem should be nearly independent of the timestep used. With a spacecraft velocity of 7.8 km/sec, it takes 650 □s for an ion to cross the grid. In calculations with timesteps near and larger than 650 □s, most of the ions cross the entire grid within each timestep—increasing the resemblance to the original static full trajectory approach. The results for different timesteps are shown in Figure 39 through Figure 44. As the timestep is increased the wake region becomes more compact and the results more unstable. In the shorter timestep calculations, the probe-side potential contour shape and potential gradient are fairly stable from timestep to timestep—after the initial macroparticles are able to cross the entire gird. With longer timesteps the results are less stable. The potentials are less smooth and they vary more from timestep to timestep.
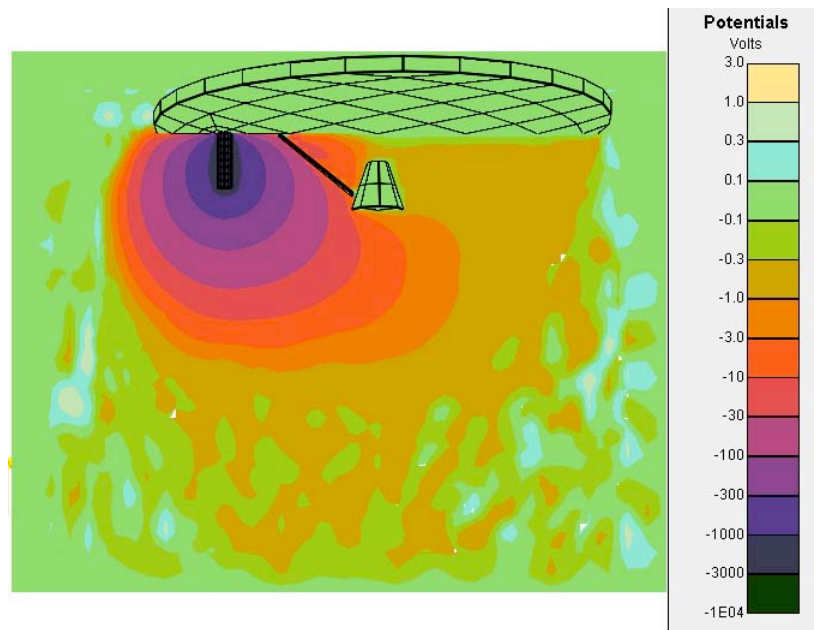
Figure 39. Potentials in Space for CHAWS Problem – Self-consistent Potentials and Charge Density Computed Using Hybrid PIC with Orbit-averaging Approach with a 50 μs Timestep, after 120 Timesteps (6 ms)
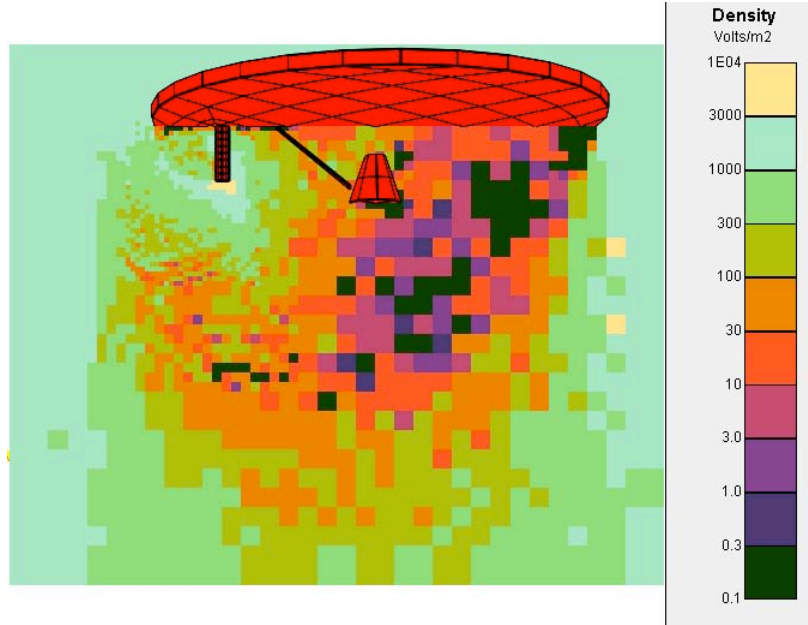
Figure 40. Ion Charge Densities for CHAWS Problem – Self-consistent Potentials and Charge Density Computed Using Hybrid PIC with Orbit-averaging Approach with a 50 μs Timestep, after 120 Timesteps (6 ms)
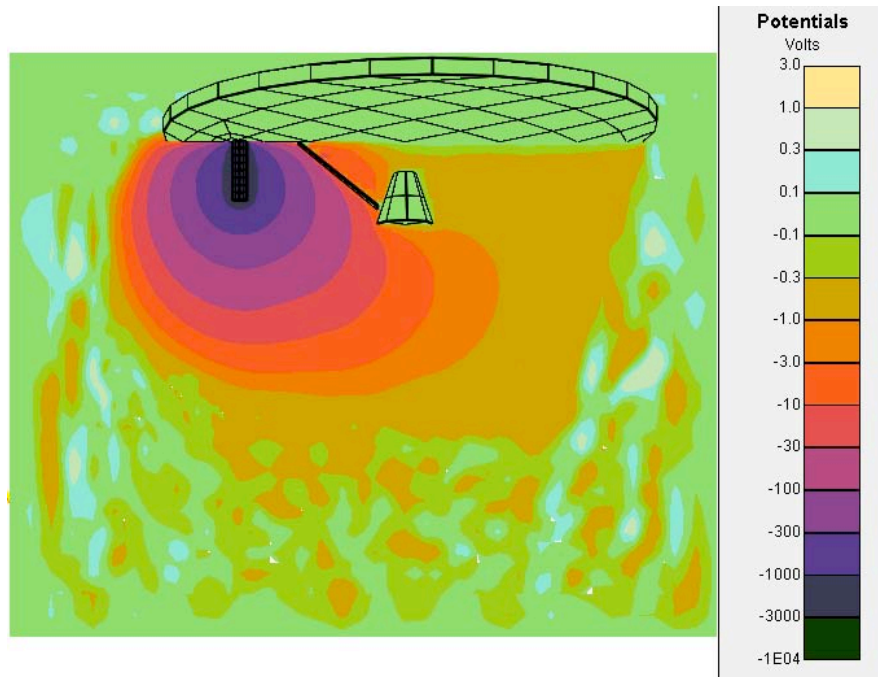
Figure 41. Potentials in Space for CHAWS Problem – Self-consistent Potentials and Charge Density Computed Using Hybrid PIC with Orbit-averaging Approach with a 500 μs Timestep, after 20 Timesteps (10 ms)
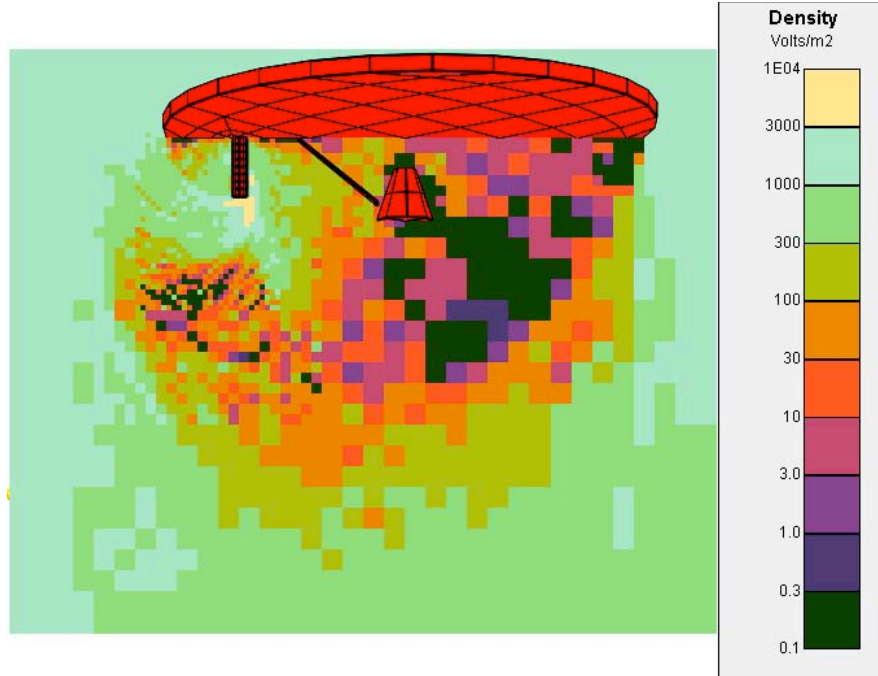
Figure 42. Ion Charge Densities for CHAWS Problem – Self-consistent Potentials and Charge Density Computed Using Hybrid PIC With Orbit-averaging Approach with a 500 μs Timestep, after 20 Timesteps (10 ms)
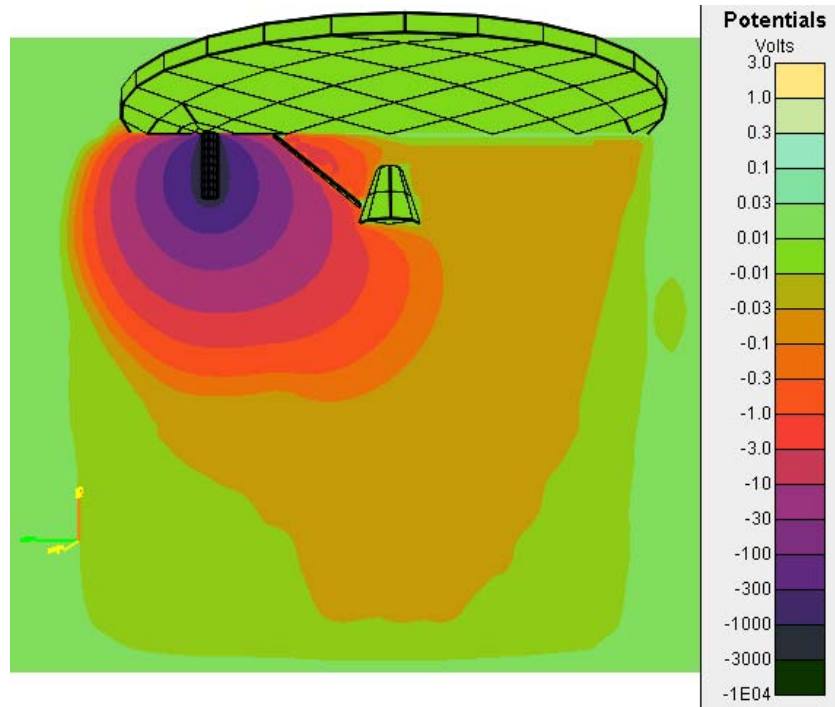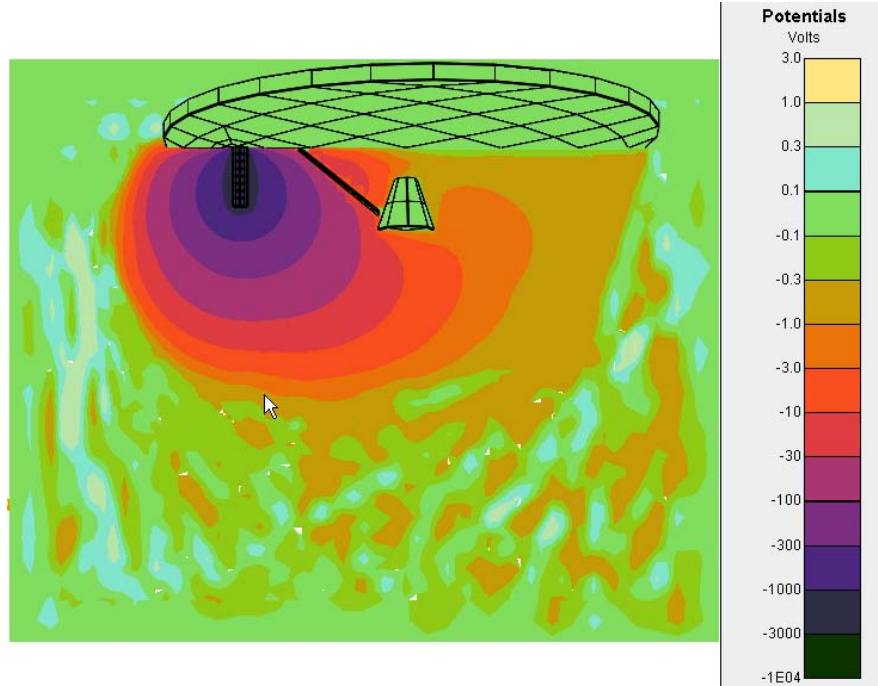

Figure 43. Potentials In Space for CHAWS Problem – Self-consistent Potentials and Charge Density Computed Using Hybrid PIC with Orbit-averaging Approach with a 5 ms Timestep, after 10 Timesteps (50 ms)
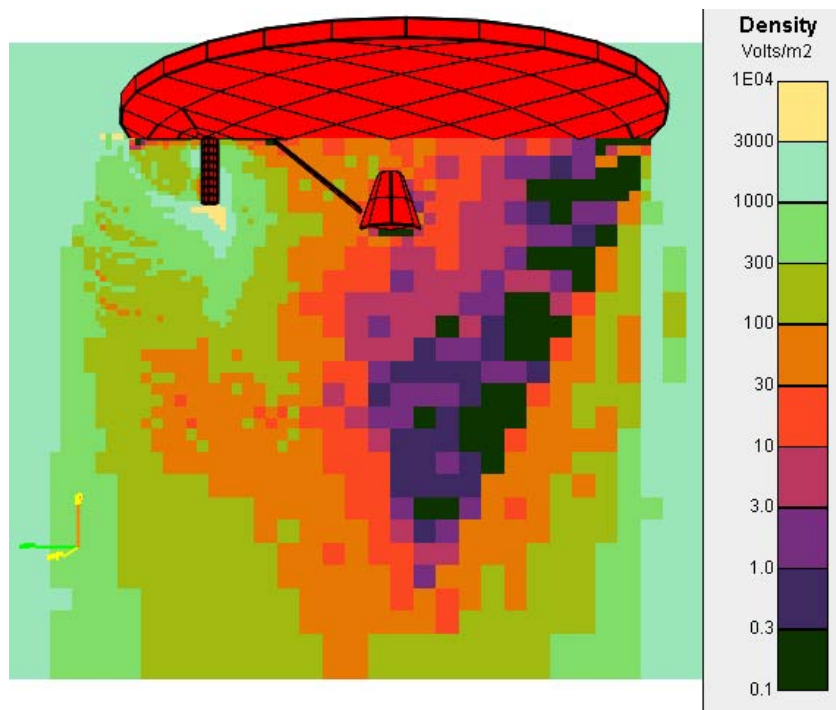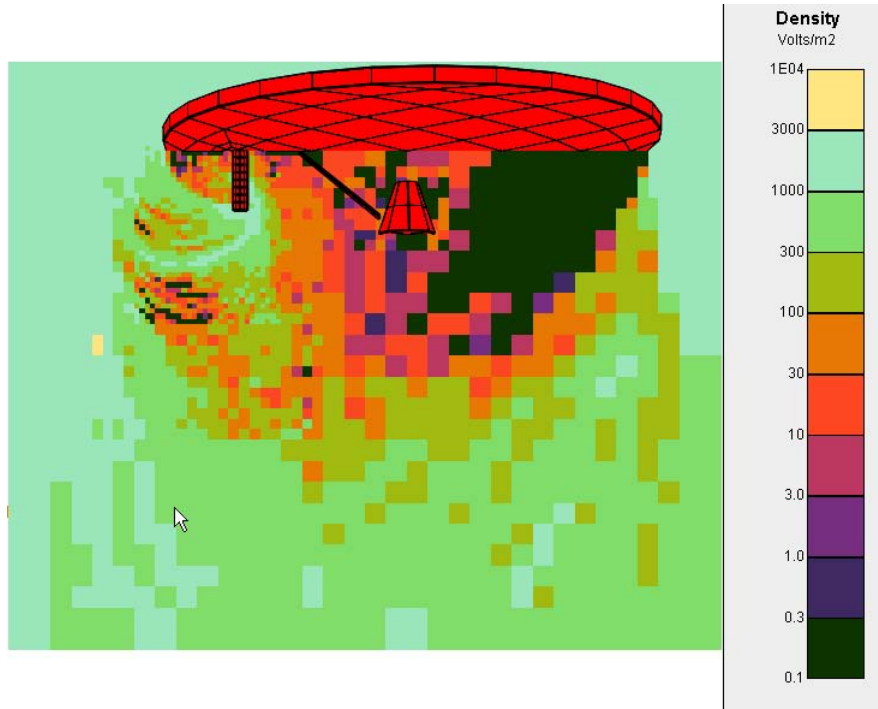
Figure 44. Ion Charge Densities for CHAWS Problem – Self-consistent Potentials and Charge Density Computed Using Hybrid PIC with Orbit-averaging Approach with a 5 ms Timestep, after 10 Timesteps (50 ms)

Another way to view the fidelity of the simulation is the current to the CHAWS probe. The probe current from the full trajectory calculation and from Hybrid PIC orbit-averaged calculations with 5, 50, 200, 500, 1000, and 5000 μs timesteps are shown in Figure 45 as a function of timestep (or iteration for full trajectory). With a timestep of 650 μs an ion crosses the computational grid in a single timestep, and so these calculations span static and dynamic extremes of many timesteps per grid crossing to several grid crossings per timestep.

The full trajectory approach yields a rapidly and smoothly converging probe current. Note that the densities are computed using the "sharing" approach: 70% of the previous charge density and 30% of the most recently computed charge density as described above. A few calculations were done with sharing of charge densities between timesteps in the same manner as for the full trajectory calculations. The probe current is unaffected by the presence/absence of sharing. (Those with sharing denoted 'WS' in the Figure 45 legend). Figure 46 illustrates the convergence for three shorter-timestep calculations (5, 50 and 200 μs timesteps), plotting probe current as a function of simulation time.
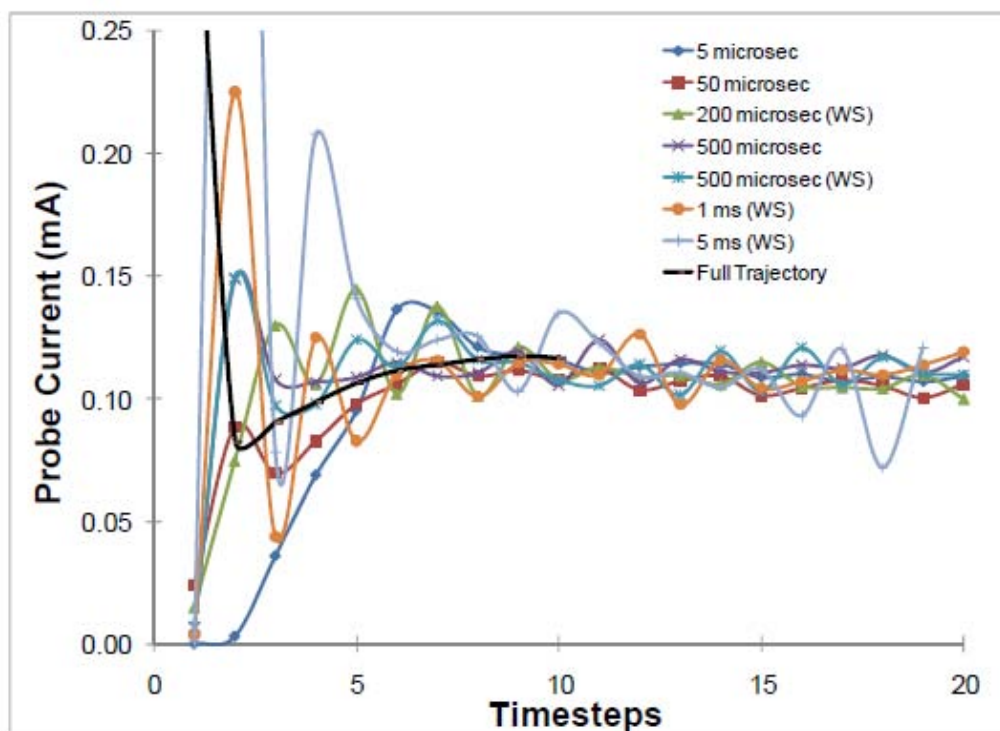
Figure 45. Ion Current to Probe as a Function of Timestep, for Various Timestep Values and as a Function of Iteration for the Full Trajectory Calculation
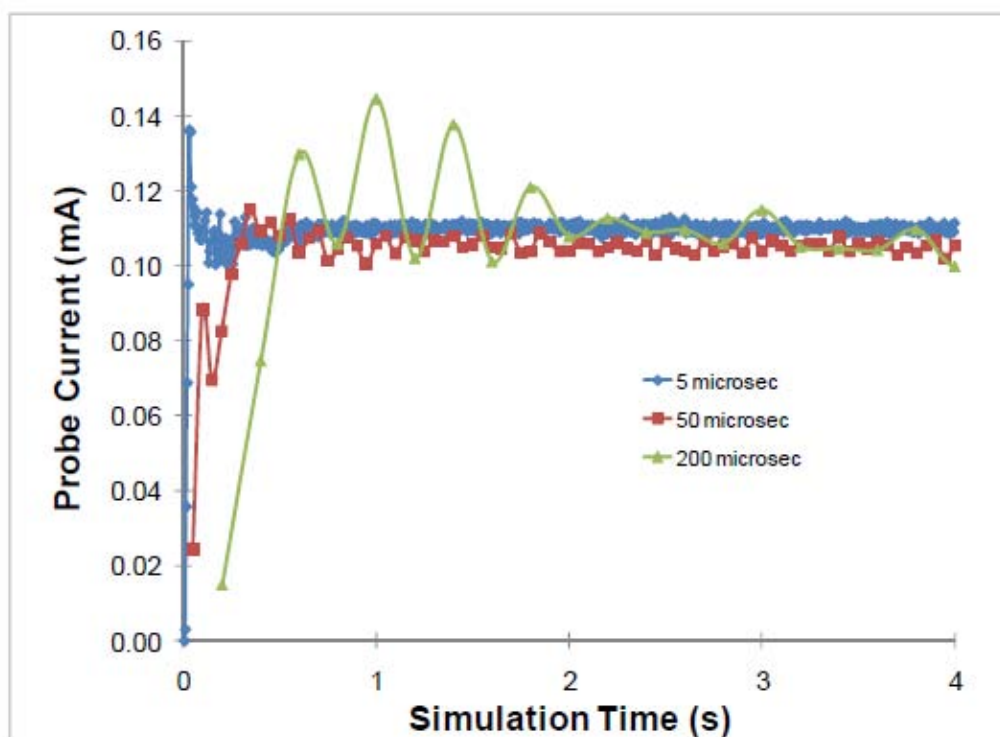
Figure 46. Ion Current to Probe as Function of Simulation Time for 5, 50, and 200 μs Timesteps

As seen from Table 1, the total running time using the Hybrid PIC approach increases significantly when a large number of timesteps are needed. Note that large-timestep calculations experience greater step-to-step noise even at late-time convergence, consistent with the less stable potentials as seen in Figure 39, Figure 41, and Figure 43.

Table 1. Representative Runtimes for Different Timestep Lengths

Timestep/Params	Minutes to Convergence
Full Traj	160
5 µs	1800
500 µs	340
5000 µs	250

6. ORBIT AVERAGING

We are using current collection by a sphere to explore the advantages and drawbacks of *Nascap-2k*'s orbit averaging technique to compute charge densities as part of a Hybrid PIC calculation of potentials in space.

We computed ion collection by a 100 V, 0.1 m radius sphere from a 10^{10} m^{-3}, 1 eV plasma in four different ways. The results are shown in Figure 47.
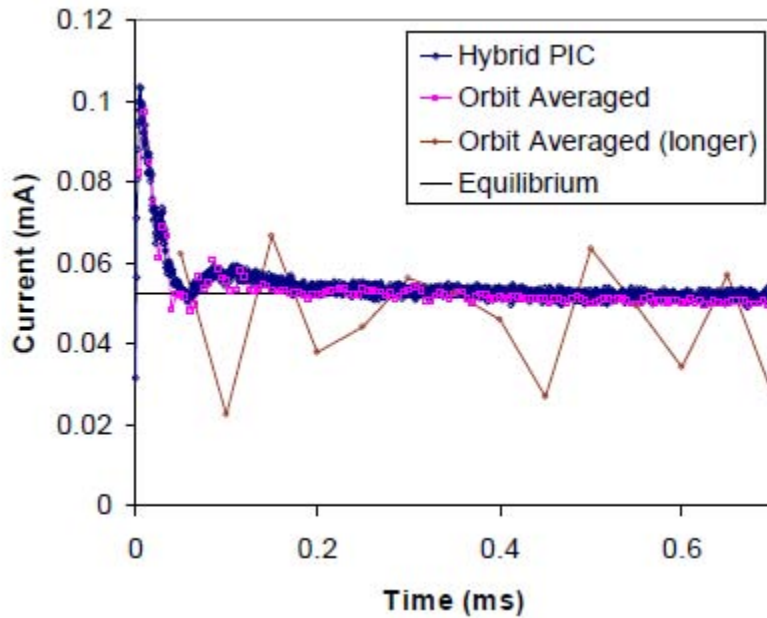
Figure 47. Ion Current to -100 V Sphere Computed Using Four Different Techniques

The equilibrium current is computed by using the analytic space charge approximation and tracking macroparticles from a 0.7 V sheath edge. (Since all the macroparticles are collected, this result is just the area of the sheath surface.) Since this approach doesn't include presheath enhancement, the result is then multiplied by a factor of 1.45, to give 52.5 µA.

The Hybrid PIC solution is computed by initially filling the computational space with a thermal distribution of macroparticles, tracking all of the macroparticles for 0.5 µs, computing potentials using the ion charge density at the end of the tracking step, and then repeating the tracking and potential computation steps for 0.7 ms (1400 timesteps). When a macroparticle reaches a grid boundary, it is split into multiple macroparticles, if it carries too much charge for the new grid. A thermal distribution of new macroparticles are injected from the boundary every tenth timestep in order to compensate for the current collected by the sphere. The equilibrium solution is reached in about 0.2 ms. This is about as long as needed for most of the macroparticles incident on the boundary at the first timestep to reach the sphere.

The Hybrid PIC, orbit-averaged solution is computed in a similar manner to the Hybrid PIC solution. The difference is that rather than depositing charge to the nodes for the ion density contribution of the charge density and to volume elements for the computation of the electron contribution to the charge density and the charge stabilization at each PIC timestep, charge is deposited at each step of the trajectory and accumulated through the timestep. This allows for timesteps longer than the time to cross a single volume element. With a 5 µs timestep and boundary current injection at every timestep, the current to the sphere is similar to that given by the standard Hybrid PIC approach. As macroparticles are injected every timestep, rather than every 10 timesteps, the number of macroparticles is similar to that in the standard Hybrid PIC. The total running time is about the same, as the potential computation is only 5% to 10% of the total execution time.

We also computed the current to the sphere using the Hybrid PIC, orbit-averaged approach and a 50 µs timestep. This calculation has large variations in the collected current from cycle to cycle. Using the present algorithms, the Hybrid PIC solution to ion current collection by a negative sphere at constant potential reaches the equilibrium solution rapidly. The orbit averaging technique gives the same results and requires about the same amount of computational time if the integration time is a fraction of the time need for the bulk of the ions to either be collected or leave the computational space.

The role of initialization and adjustments to the technique needed to accommodate timesteps comparable to and longer than the time needed to cross the computational space remain to be explored.

7. PSEUDOPOTENTIAL ALGORITHMS FOR SIMULATION OF VLF PLASMA ANTENNA CURRENT FLOW

We developed pseudopotential approaches (similar to the velocity potential used to describe potential flow [1] in fluid dynamics) to the computation of transverse surface currents on a spacecraft acting as an antenna and to the computation of electron currents in the sheath and near sheath about the spacecraft. These approaches have been implemented within *Nascap-2k*.

The transverse surface current algorithm in *Nascap-2k* is used to calculate the current flowing along an antenna element or other object, accounting correctly for both local capacitance and incident plasma current. The surface is divided into many surface elements. The change in charge on a surface element during a timestep is that which is needed to accomplish the change in surface electric field, which is obtained from the *Nascap-2k* potential calculation. The current to each surface element consists of the transverse surface current from neighboring surface elements and the current provided by the plasma, which is provided by the *Nascap-2k* PIC (particle-in-cell) simulation. The current continuity equation is solved using a pseudopotential approach. As a boundary condition, one surface element of each antenna element is specified as connected to the biasing power supply. With pseudopotential values assigned to each surface element, the solution provides the currents crossing edges between surfaces needed to satisfy the problem dynamics. This approach excludes solutions with circulating currents. The vector transverse surface current in each surface element is taken as that which provides the best fit to the edge currents.

The volume current algorithm is used to calculate electron currents within and near the sheath about a VLF antenna or other high-voltage object. Within the *Nascap-2k* framework, local equilibrium electron densities are generated for each volume element as part of the PIC ion dynamics algorithm, and their time derivatives are the main drivers for volume currents. Space outside the calculation boundary can act as either a source or a sink for electrons, and object surfaces may act as electron sinks.

The example used here is a *Nascap-2k* simulation of the DSX transmitting antenna in low density hydrogen plasma. Parameters of the calculation are shown in
Table **2**. Note that the 1000 V square wave bias is approximated by the sum of the first and third harmonics, so that the actual peak-to-peak voltage is closer to 1200 V.

Table 2. Parameters For DSX Antenna Simulation

Antenna Length (tip to tip)	81
Antenna Diameter	0.1 m
Bias Voltage (Peak to Peak)	1000 V
Bias Frequency	10 kHz
Plasma Density	10^8 m^{-3}
Plasma Temperature	1 eV

7.1 Mathematical Formulation

The basic equation to be solved is $\mathbf{\nabla} \cdot \mathbf{J} + \frac{\partial \rho}{\partial t} = 0$, where J is the surface or volume current density due to electrons, and ρ is the surface or volume electron charge density. Note that the solution for the current is non-unique to the addition of any divergence-free current field. We assume that,

provided appropriate boundary conditions are implemented, such circulating currents are not of concern to the problem being solved.

A solution having no circulating currents is guaranteed if we assign a pseudopotential value to each element of surface or volume and take the current across their common boundary (edge or face) to be proportional to the difference in their pseudopotentials. (In that case, current that flows "downhill" would need to flow back "uphill" in order to "circulate.") The current is also taken as proportional to the interface area (edge length or face area) and inversely proportional to the distance between the centers of the elements.

The result of the above treatment is a matrix that multiplies the vector of pseudopotentials to describe the buildup of charge in the surface or volume elements, which is then set equal to the source vector generated from *Nascap-2k* results at each timestep. This system of equations is then solved using the ICCG (Incomplete Cholesky Conjugate Gradient) [2] algorithm.

7.2 Application to Surface Currents

The spacecraft has two or more antenna elements (represented by conductor numbers in *Nascap-2k*) that are biased in a programmed way (generally periodic) by an amplifier. Typically the spacecraft will have passive elements as well. The amplifier injects current at a specified location on each antenna element to maintain the programmed voltage. The injected current, modified by current collected from the plasma, flows on the spacecraft surfaces so as to maintain the specified potential difference between each surface element and ambient plasma.

Figure 48 shows graphically the quantities that make up the surface current equation for each surface element. Moving the surface currents to the left side of the equation, and all other (known) quantities to the right, and expressing the edge currents as proportional to pseudopotential differences, results in a sparse symmetric matrix that is amenable to solution using the ICCG algorithm once the surface element connected to the power supply (denoted the "injection element") is set to a fixed potential. The current required to bias the conductor may be obtained by evaluating the equation associated with the injection element and can be verified to be the sum of the total change in charge less plasma currents for all the remaining surfaces of the conductor. Surface currents are solved separately for each electrically isolated component.
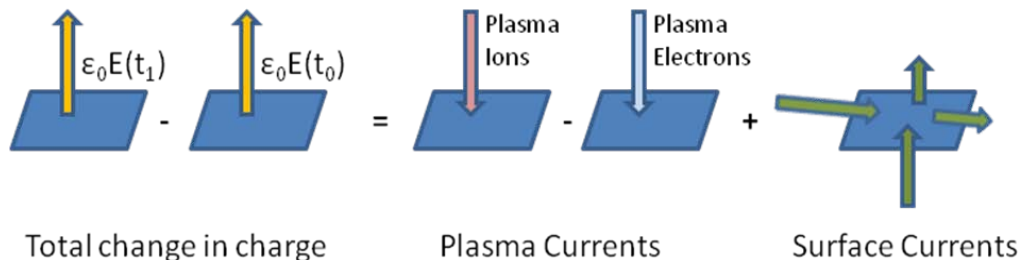
Figure 48. The Change in Charge on a Surface Element is Made Up of Plasma Currents and Surface Currents

The following figures show surface currents from a simulation of the DSX model at the time of peak surface current in the antenna elements, *i.e.,* the surface current while the bias polarity is switching. A close-up of the portion of the antenna elements near the roots with surfaces color-coded by surface current magnitude is shown in Figure 49. The height of each cone is proportional to the square root of the surface current density and to the square root of the surface element area. Note that the current flows in the same direction on both antenna elements. Figure 50 shows the full length of both antenna elements. The current is a maximum at the antenna element roots (*i.e.,* at the power supply) and decreases toward the tips. The current magnitude as a function of location along the antenna element is plotted in Figure 51, with the spatial derivative of surface current plotted using the scale on the right. This shows that the current varies linearly over most of the antenna elements, with a large amount of capacitive loading near the root and a smaller amount near the antenna element tip. Figure 52 illustrates the time dependence of the surface current, plotted together with the applied voltage. As expected for a capacitive system, the surface current is the time derivative of the potential (with very small modification due to incident plasma current), and this is largest when the two antenna elements are switching polarity, and strongly emphasizes the third harmonic frequency.

$$A(\mathbf{r}) = \frac{\mu_0}{4\pi} \sum_{cells} \frac{Area_{cell} \times \mathbf{j}_{cell}}{|\mathbf{r} - \mathbf{r}_{cell}|}$$
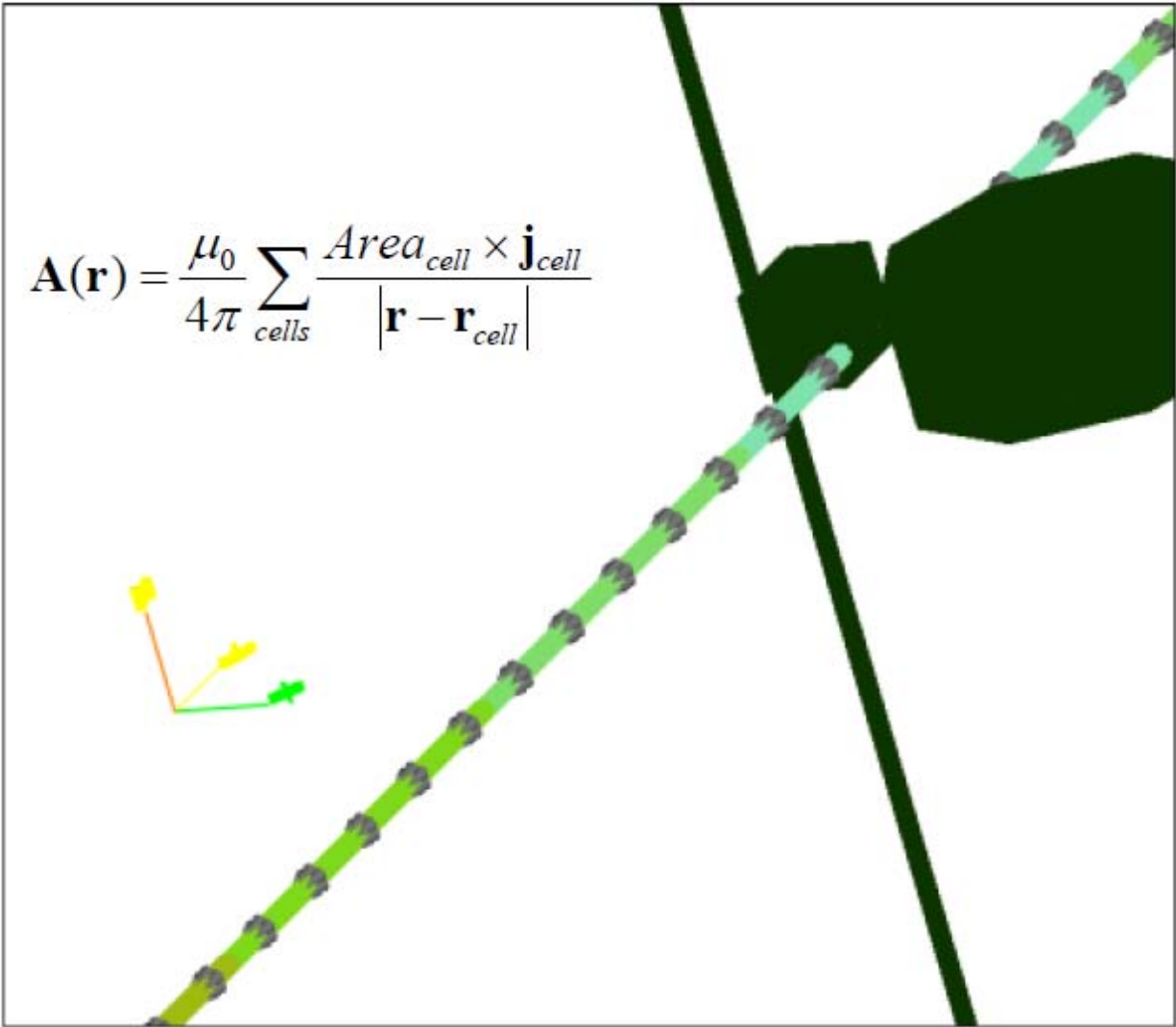
Figure 49. Graphical Display of Transverse Surface Currents, with Equation Relating Element Surface Currents to Vector Potential
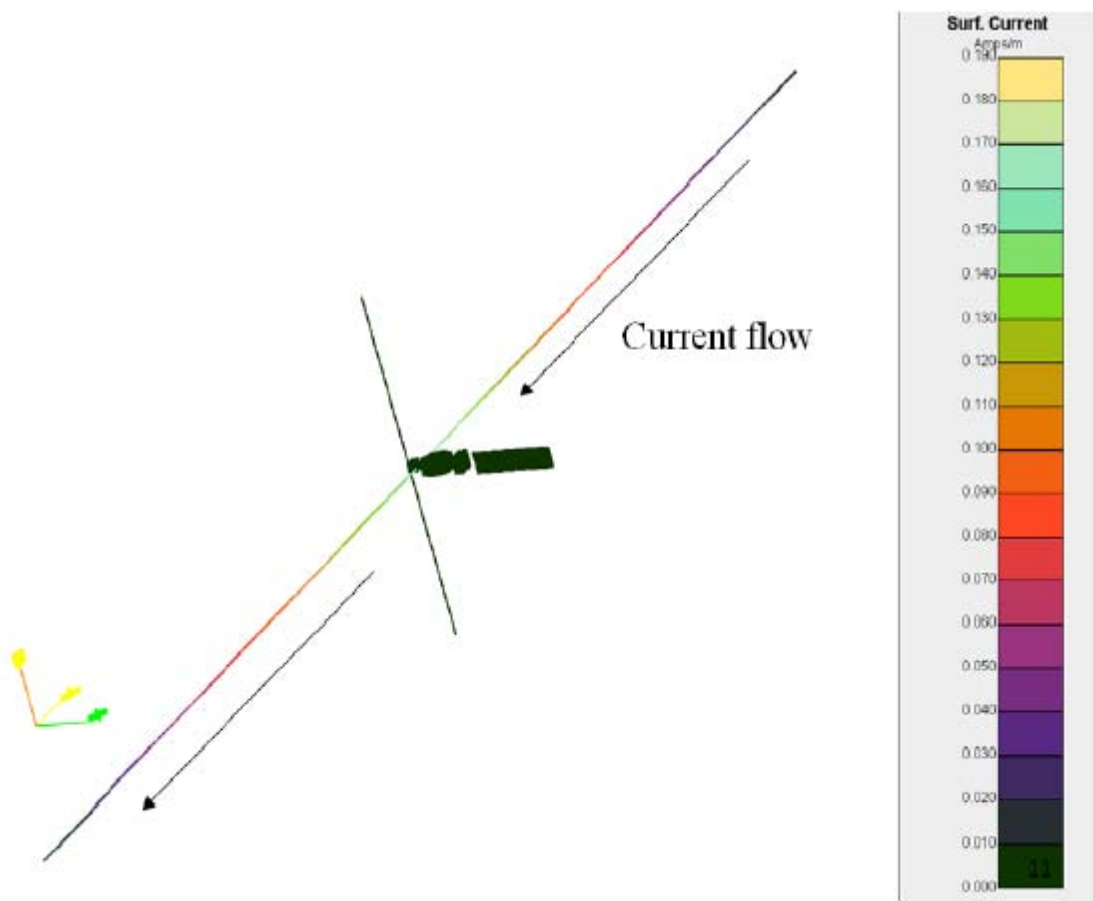
Figure 50. Another Graphical Display of Surface Current Flow on Antenna Elements, Showing Current Maximum at Antenna Element Roots Decreasing Toward Tips
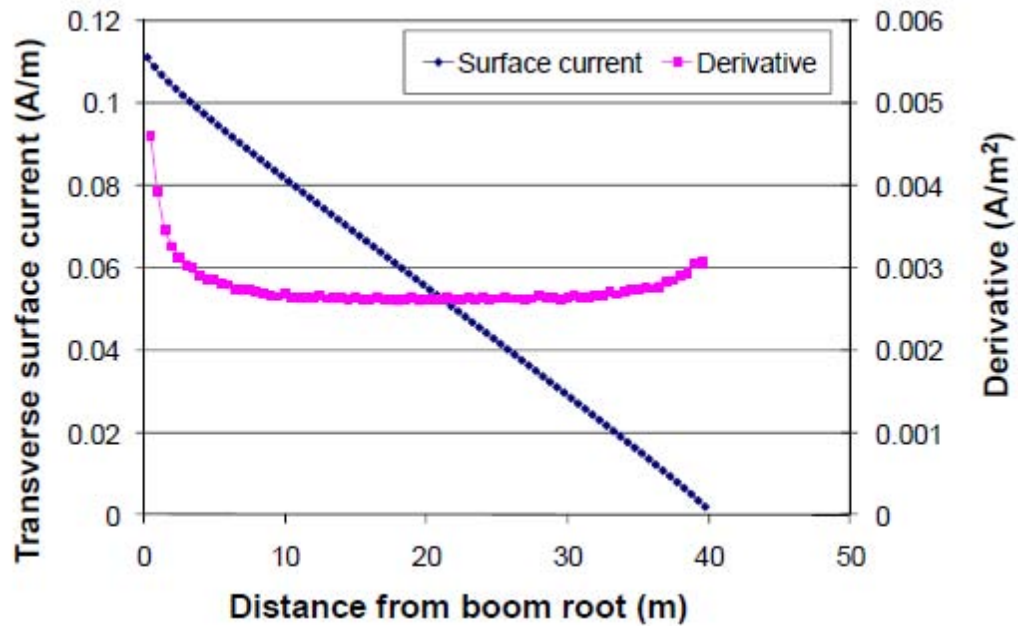
Figure 51. Plot of Surface Currents Corresponding to One Antenna Element of Figure 50, Showing that Current Varies Nearly Linearly Along the Antenna Element, With Capacitive Loading at Ends
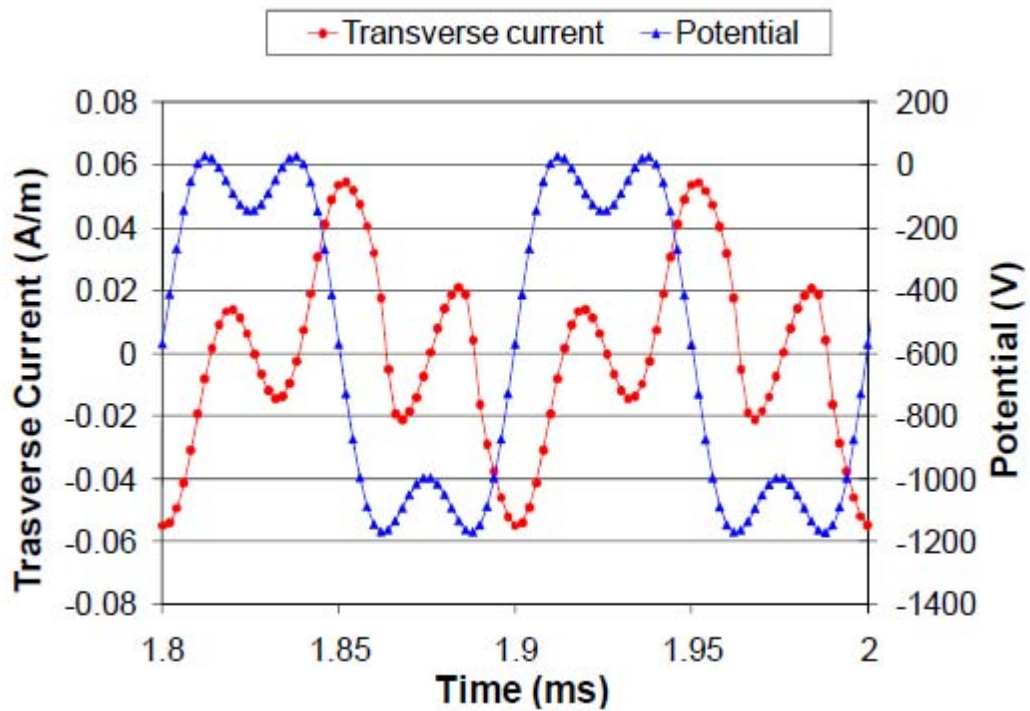
Figure 52. Variation of Average Transverse Current in One Antenna Element Over Two Full Cycles

7.3 Application to Volume Electron Currents

Generation of propagating waves in plasma is due primarily to electron currents flowing in the bulk cold plasma. While plasma ion currents can be generated directly by the PIC ion simulation used to obtain the sheath dynamics, it is impractical to simulate electron macroparticles to obtain electron currents. The calculation we use as an example is a simulation using greater than 6×10^7 ion macroparticles. If electrons were tracked as well (instead of using a "fluid" or "local equilibrium" approximation), a much larger number of electron macroparticles would be required, as well as a shorter timestep. The plasma ion current patterns, obtained directly from the ion tracking, are discussed in Section 10.

The main requirement for application of the pseudopotential approach to the calculation of volume electron currents is that the electron density for each volume element (as used in the calculation of electrostatic potential during the PIC calculation) be stored (or computable) for each timestep. In addition, we need to establish boundary conditions at the external boundary and near the spacecraft, develop a local conductivity tensor that reflects the non-uniform and anisotropic nature of the plasma, and do extra bookkeeping for currents crossing grid boundaries. We have thus far restricted application of the pseudopotential method to cubic (empty) volume elements and allow current flow through the six faces of each cube, *i.e.*, in the X, Y, and Z coordinate directions.

The volume external to the computational space is assigned a single pseudopotential with value fixed at zero. This allows the external space to be a source or sink of electrons at each element of the external boundary surface.

In *Nascap-2k*, the object is surrounded by "special," (*i.e.*, non-cubic) volume elements. At the interface between an empty element and a special element, we allow the special element to be a sink, but not a source, of electrons. Specifically, if the electric field in the empty element points toward the special element, we take the electron current crossing the interface to be zero. If the electric field points away from the special element, we take the electron current crossing the interface to be the plasma thermal current at the empty element's density. This treatment represents the collection of electrons by positive surfaces.

The treatment must also recognize that electron current flows along paths with an electron population that can support such current and not along paths that are devoid of electrons (such as the interior of a sheath). To that end, we set the conductivity to be proportional to the square root of local electron density (*i.e.*, to the electron density divided by a scattering rate taken to be proportional to the electron plasma frequency). The conductivity is expressed as a tensor so that anisotropy due to magnetic field can be taken into account.

To illustrate the behavior of this algorithm, we use a DSX transmitting antenna simulation having the parameters shown in Table 2. The current pattern at the time that the antenna elements are switching is shown in Figure 53. At this point in time both antenna elements are at -577 V, with the upper element becoming more negative so that its sheath is growing and expelling electrons, and the lower positive element becoming less negative so that its sheath is shrinking with electrons filling in the formerly negative space. In the left (X-component) portion of the figure, the light area at upper left indicates current moving to the right, or electrons to the left, away from the upper antenna element. Similarly, the light and dark areas in the remaining

quadrants all show electrons moving away from the upper antenna element and toward the lower antenna element. The Y-component currents at the same time show upward current (downward electron motion) in the neighborhood of the sheath edge. Note that there is negligible current in the interior of the sheath. If the conductivity tensor does not account for the low electron density in the sheath, the entire sheath is filled with substantial upward current, which is unphysical since electrons are excluded from the region.
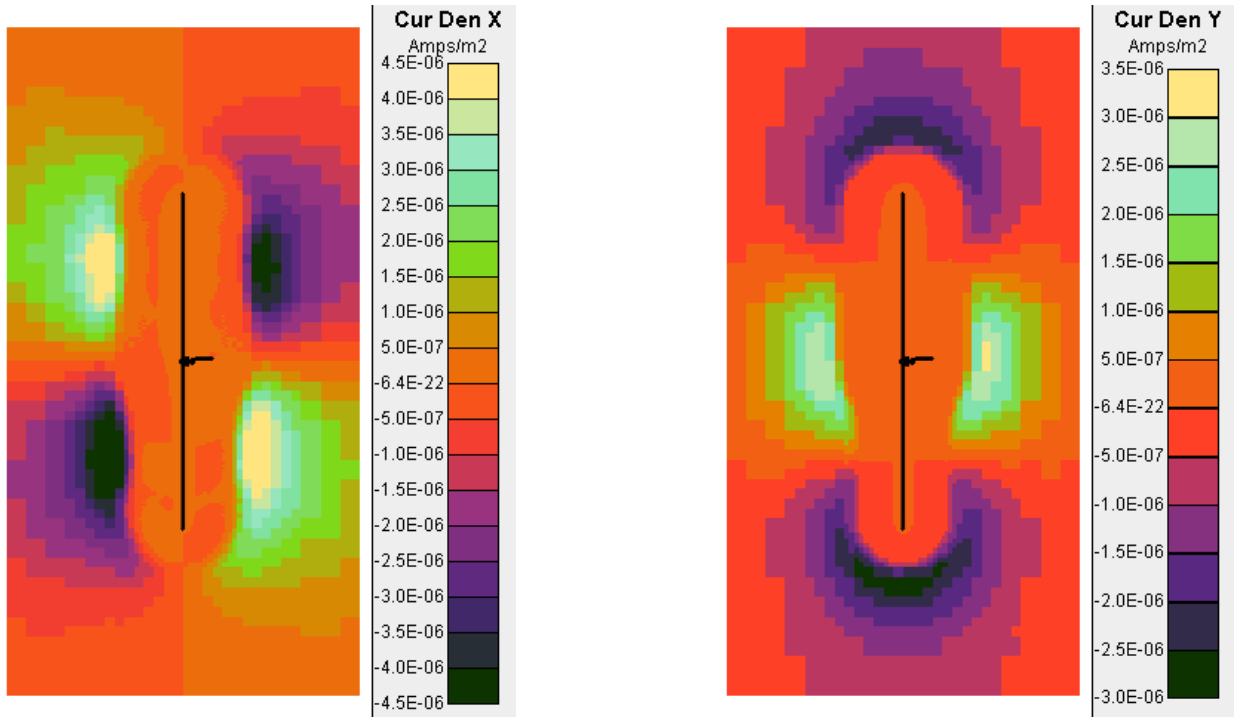
Figure 53. X (Left) and Y (Right) Component of Current (Am^{-2}) when Antenna Elements are Switching – See Discussion in Text

Figure 54 shows the electron currents generated when the lower antenna element is positive and collecting electron current. The outward current (inward electron flow), which is needed both to supply the electrons collected by the antenna element and to fill in the contracting sheath, fills a large volume around the antenna. When the currents are plotted on a log scale, the smaller outward electron flow can be seen near the still-expanding sheath edge around the negative antenna element. Figure 55 shows that a short time later the electron current has reversed sign as the lower antenna element has become negative and is expelling electrons from its sheath.
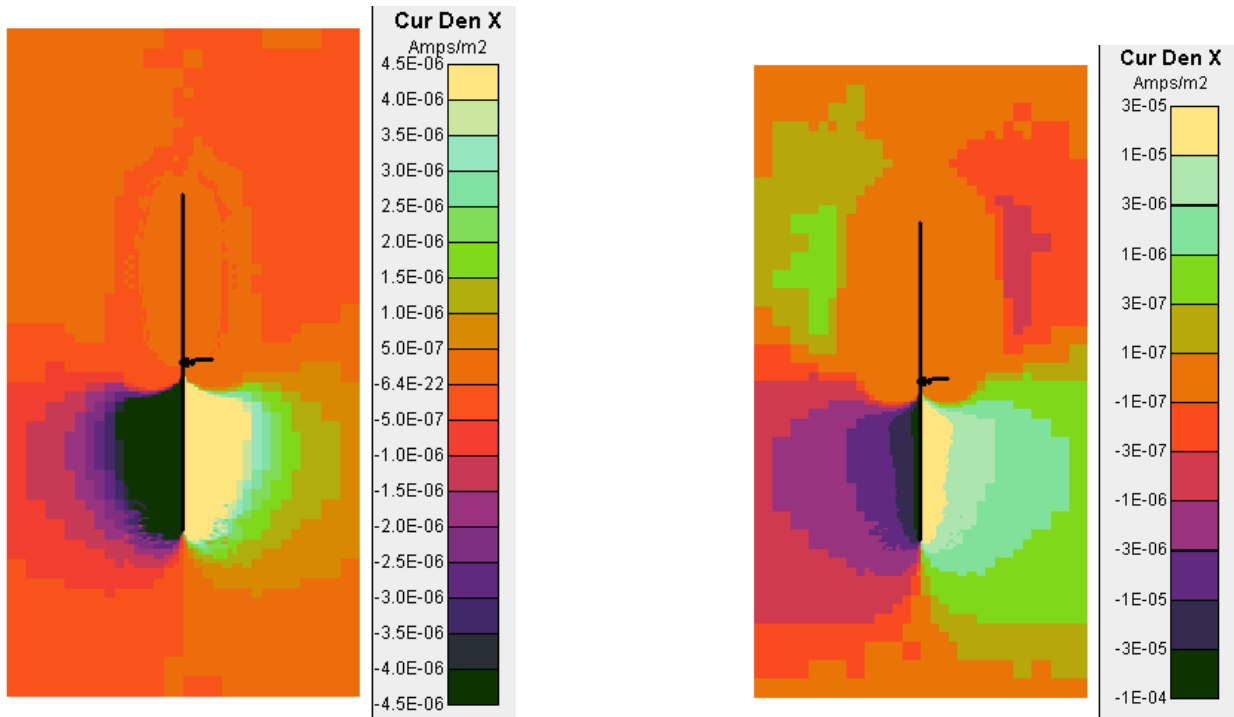
Figure 54. X Component of Electron Current on Linear and Log Scales when Lower Antenna Element is at +0.16 V – Electrons are Collected by Lower Antenna Element
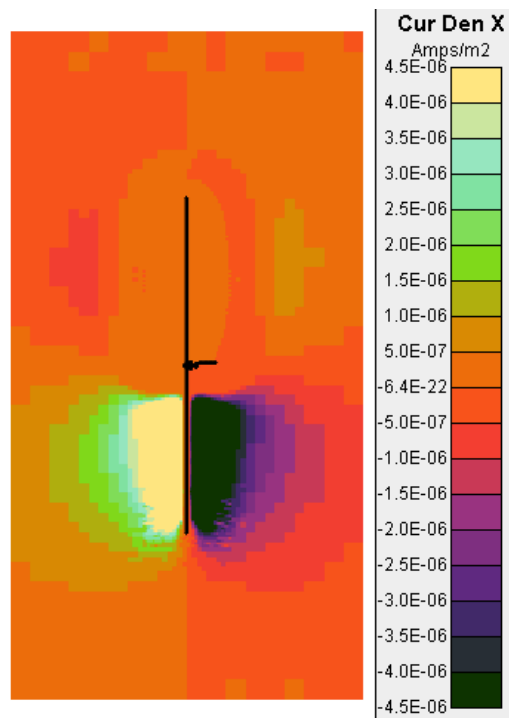
Figure 55. X Component of Electron Current when Lower Element Switches from Positive to Negative Potential (Here at -13 V) – Electrons are Expelled from the Near-Antenna Region to Form a Sheath, and Flow Outward

Figure 53 (left panel) indicates electrons moving outward into ambient plasma in the upper half of the figure and inward in the lower half. These counterstreaming electron currents are commonly associated with whistler waves. The right panel of Figure 53 suggests that the closing Y-component current is small at the boundary so that the counterstreaming currents have considerable extent. If the magnetic field is in the X-direction, then the closing Y-component current is suppressed and the extent of the counterstreaming currents enhanced.

7.4 Summary

We have demonstrated the use of pseudopotential methods to calculate surface currents and volume electron currents. The source terms for these currents are obtained from *Nascap-2k* dynamic sheath calculations. Boundary conditions are imposed based on physical considerations.

The source terms for the surface current algorithm are the rate of change of surface electric field at each surface element and the incident plasma currents. The fixed pseudopotential boundary condition of an active antenna element is applied at the location of the power supply connection (antenna element root). For a passive object component any surface element's pseudopotential may be fixed, as this object component's total charge changes only due to incident plasma currents.

The source term for the volume electron current algorithm is the calculated rate of change of electron charge in each volume element. The external space is held at fixed pseudopotential so that it can act as either a source or a sink for electrons. Positive surfaces act as sinks for electrons. A local conductivity tensor is used to reflect the ability of the electron population to carry current, embodying the effects of magnetic field and local electron density.

A surface current example was presented showing calculation of current on the DSX transmitting antenna. Results showed that the current varied linearly over most of the antenna element, with capacitive loading at the root and tip.

Volume electron currents were illustrated by the same DSX calculation and showed counterstreaming electron currents in the distant plasma.

8. PROTOTYPE OF NASCAP-2K REALTIME

Nascap-2k RealTime Prototype computes surface potentials on spacecraft in response to tabular spectra provided in real time. It is a stand-alone Java application and uses a robust version of the Boundary Element Method (BEM) charging algorithms developed for *Nascap-2k* and originally implemented in Java in the *SEE Interactive Spacecraft Charging Handbook*. The charging algorithms used are only appropriate to the low density plasma environments found at geostationary altitude. The algorithm used to determine the sun direction is also only appropriate to spacecraft at geostationary altitude.

Nascap-2k RealTime Prototype executes in response to the command line prompt
java –jar Nascap2kRT.jar -prefix *MiniDSCS* -envFileName *SW199610500900sat_01.0.MSM* -satConfFileName *satel_C01.01* where the options are specified in Table 3.

Nascap-2k RealTime Prototype requires four input files:

- *Object Toolkit* description of spacecraft, including specification of rotating solar arrays. (*prefix*Object.xml)

- List of times, plasma environments, and positions of the spacecraft. The environment can be expressed either as a table of fluxes in various energy bins or as a Maxwellian. (MSM file or XML file)

- Previously computed potentials for each surface at each timestep and the environments used to compute the potentials. (*prefix*Steps.xml)

- Satellite configuration file used only to determine the heading of the output file.

Nascap-2k RealTime Prototype creates two output files:

- Computed potentials for each surface at each timestep and environment used to compute the potentials. (*prefix*Steps.xml)

- Table of chassis potential, minimum differential potential, and maximum differential potential for the times specified in the input file. (SUR file)

The format of the MSM, SUR, and configuration files are given in *Interface Control Document for The SEEFS Satellite Charging/Discharging Product* dated May 11, 2005. The format of the Maxwellian environment and *prefix*Steps.xml files are given in the examples.

The calculation consists of five steps:

- Object initialization

- Read environments

- Initialize calculation

- Timestepping

- Write output files

Table 3. Options for Running *Nascap-2k RealTime Prototype*

Option	Meaning	Default
-prefix *prefix*	The *Object ToolKit* file for the object must be in the run directory as *prefix*Object.xml. Calculated potentials are written to and read from *prefix*Steps.xml.	None
-envFileName *EnvFile*	Name of the environment file to use. Either an MSM file or a Maxwellian in an xml format.	None
-satConfFileName *satConfFile*	Name of the satellite configuration file to use (e.g. satel_C01.01).	None
-dir *Directory*	Specifies the directory in which all input and output files appear.	Local directory
-maxDataSaveTime *maxSaveTime*	The maximum time span to save data in *prefix*Steps.xml file; specified in hours.	6 hours
-timeStep *TStep*	Timestep (in seconds). Presently must be an integer.	10 seconds
-advanceTime *advTime*	Minutes to continue the calculation past the last environment in the environment file. Presently must be an integer.	0 minutes
-minsToUpConf *confUpdateTime*	Number of minutes the calculation runs without a bad result before the confidence level is increased. This is a real number.	1 minute

8.1 Calculational Steps

8.1.1 Read Command Line Input and Initialize Object

The first step of the calculation is to read the command line options and attempt to create a lock file, *prefix.lck*. If the file *prefix.lck* already exists, the code exits. This test insures that for a single directory and single *prefix*, only one instance of *Nascap-2k RealTime Prototype* can execute at one time. The code then reads the configuration file and then the geometry from the *Object ToolKit* file *prefix*Object.xml. If the geometry has rotating parts like solar arrays, the rotating surfaces are specified in the object file in the standard way. The BEM matrix elements are computed for the object without rotation. If the object definition includes rotating components, the matrices are later recomputed for each sun direction provided.

8.1.2 Read Environments

The environments are read from the file specified in the command line. That the environment is given as a table of fluxes in a set of energy bins is indicated by any extension *except* xml in the file name. That the environment is specified as a Maxwellian is indicated by an extension of xml

in the file name. The environment is then specified by a list of densities, temperatures, spacecraft positions, and associated times.

If there are lines in an MSM file that do not produce valid environments, these lines are ignored and the code uses only the valid lines. Invalid environments can occur if the data is incomplete, has negative fluxes, etc.

The spacecraft position is used to determine both the orientation of any rotating components and the direction to the sun for the computation of photoemission.

Once all the environments are read from the file, the environments are ordered by time for use in the calculation.

8.1.3 Initialize Calculation

The initialization step begins by reading any previously computed results from the *prefix*Steps.xml file.

If there are no previous results, the time is set to the earliest time in the environment file, the environment is set to the environment at that time, and all the surface potentials are set to 0.0 V.

If there are previous results, the environments in the file are compared with those used in the previous calculations for the corresponding time. For tabular environments, the comparison is between the corresponding flux values, bin edge values, and eclipse indicators. For Maxwellian environments, the comparison is between the corresponding densities and the temperatures. Previously computed results for which the new environment is different from the one used in the previous computation are discarded. The time is set to the latest time for which the previously computed results are kept. The potentials on all the surfaces are set to the previously computed values at this time. The environment is set to the new environment for this time if one is available. If not, the environment is set to the environment for this time saved with the previous results.

Finally, any rotating surfaces are rotated and new BEM matrix elements are computed.

8.1.4 Time Stepping

The heart of the calculation is the time stepping through the time period specified in the environment file. The length of each timestep is set to the shorter of the timestep specified in the argument list and the time between the present time and the time associated with the next specified environment.

At each timestep, the code records the time, the maximum potential, the minimum potential, the conductor potentials, the confidence level, and the potentials on each surface in xml format. This information is written to the *prefix*Steps.xml file when the code is done (not during execution). The code continues to run until the present time reaches the time associated with the latest environment in the input file plus the time period specified in the argument list.

At the end of each timestep, the code checks for a new environment for the present time. If one exists, the spacecraft position is used to compute the position of any rotating surfaces and the sun direction. New BEM matrix elements are computed for the new spacecraft configuration.

8.1.4.1 Algorithm for the Computation of Confidence Level

The code uses four confidence levels; 0, 30, 50, and 70. When a new calculation is started and the potentials are all set to 0, the confidence level is set to 0.

If the potential on any surface after a timestep is NaN (not a number), all potentials are set to 0 and the confidence level is reset to 0. (We expect this to be infrequent.)

At the end of each timestep, if there is a surface potential > 20 V or $< -10,000$ V, the confidence is decreased one level. If the chassis potential changes more than 1 kV over one minute while the satellite is sunlit, the confidence level is decreased by one. If the differential potential increases or decreases by more than 500 V over one minute, the confidence level is decreased by one. If the confidence level has not changed for the specified period of time, it increases by one level.

8.1.4.2 Surface Currents

For environments specified as a table, the surface currents are computed from the following expression.

$$
\dot{J}_{surface}^{electron}(\phi) = \sum_{\left(E_i^{binMin} + \phi\right) > 0} \left(1 - Y\left(E_i^{center} + \phi\right) - B\left(E_i^{center} + \phi\right)\right) F_i \left(\frac{E_i^{center} + \phi}{E_i^{center}}\right) \Delta_i
$$

$$
+ \left(1 - Y\left(E_n^{center} + \phi\right) - B\left(E_n^{center} + \phi\right)\right) F_n \left(\frac{E_n^{center} + \phi}{E_n^{center}}\right) \left(\frac{1}{2}\right) \left(E_n^{binMax} + \phi\right) \quad [2]
$$

$$
\text{where the second term is included only if } \left(E_n^{binMin} + \phi\right) < 0 < \left(E_n^{center} + \phi\right)
$$

$$
\text{where} \left(E_{i-1}^{binMax} = E_i^{binMin} = \sqrt{E_{i-1}^{center} E_i^{center}}\right)
$$

The first term corresponds to the orbit limited collection and the second to the orbit limited collection from energy bins that are partially excluded.

8.1.5 Create Output Files

At the completion of execution, the code writes two files; the *prefix*Steps.xml, which contains the time, the maximum potential, the minimum potential, the conductor potentials, the confidence level, and the potentials on each surface at each timestep in XML format, and the .SUR file, which contains the chassis and differential potentials along with the confidence estimate at the times specified in the input MSM file.

8.2 Objects

Three geometric objects are included; a Kapton coated sphere (Figure 56), a DSCS-like spacecraft with only insulating surfaces (Figure 57), and a DSCS-like spacecraft with ITO coated solar arrays (Figure 58).
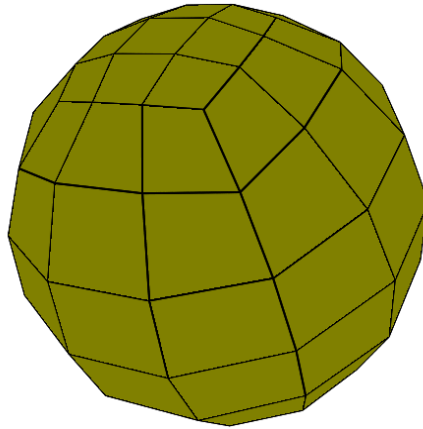

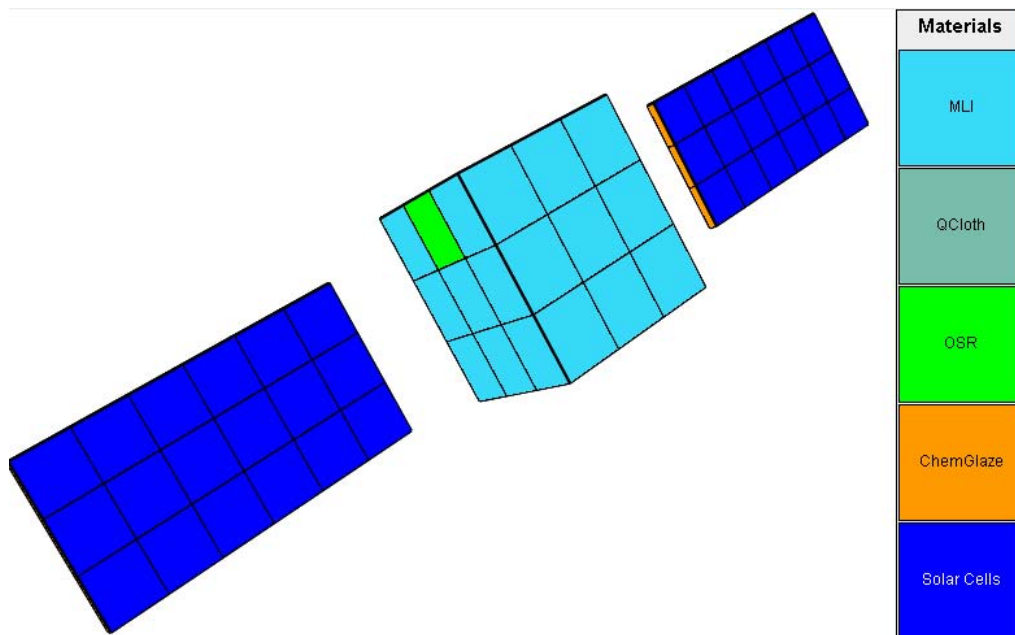**Figure 56. Spherically Shaped Object Available for Calculations**

Figure 57. DSCS-Like Spacecraft Geometry Available for Calculations – the Solar Arrays Rotate About the Long Axis in Order to Track the Sun
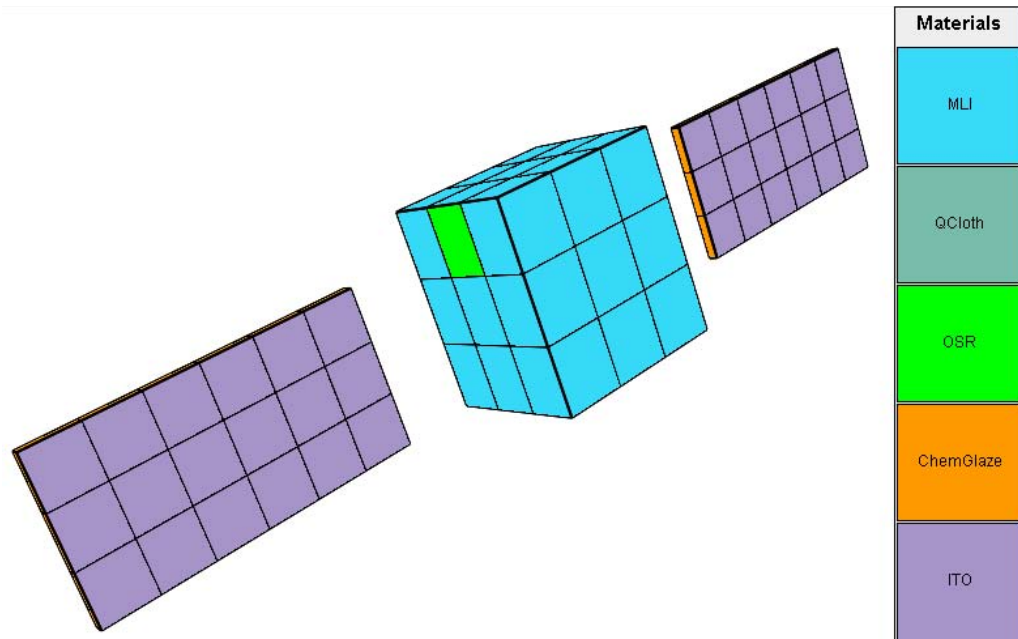
Figure 58. Second DSCS-Like Spacecraft Geometry Available for Calculations – the Solar Arrays Rotate About the Long Axis in Order to Track the Sun

8.3 Supporting Software

For convenience in viewing results or plotting, there is a MakeDataFile.jar that takes an output xml file as input and produces a text file in which each line has the time in seconds from the first time, the chassis potential, the minimum potential, and the maximum potential.

java –jar MakeDataFile.jar *prefix*Steps.xml

8.4 Verification

In order to verify that *Nascap-2k RealTime Prototype* is calculating spacecraft surface charging correctly, we compared results computed using the new code with results computed using the SEE *Interactive Spacecraft Charging Handbook*. As the *SEE Handbook* has restrictive geometry, the *Object ToolKit* object developed for early cross code comparisons was used. The spacecraft is taken to be at 0° longitude and 0° latitude. The date is January 1, 2000. The environment is the NASA Worst Case surface charging environment. The results for midnight and for 6 a.m. (solar array orientation and sun direction) computed using the *SEE Handbook*, using *Nascap-2k RealTime Prototype* and a Maxwellian environment expressed as a density and temperature, and using *Nascap-2k RealTime Prototype* and a Maxwellian environment expressed as a table of fluxes and energy bins are shown in Figure 59 and Figure 60. The results can only be as close as shown if all aspects of the charging calculation are done correctly. The same comparison, redone with ten-second timesteps in *Nascap-2k RealTime Prototype*, is shown in Figure 61 and Figure 62.

Figure 59. Comparison of Minimum, Maximum, and Chassis Potentials as a Function of Time Computed in Three Different Ways for Midnight on January 1, 2000

Figure 60. Comparison of Minimum, Maximum, and Chassis Potentials as a Function of Time Computed in Three Different Ways for 6 a.m. on January 1, 2000

Midnight; January 1, 2000; NASA Worst Case environment
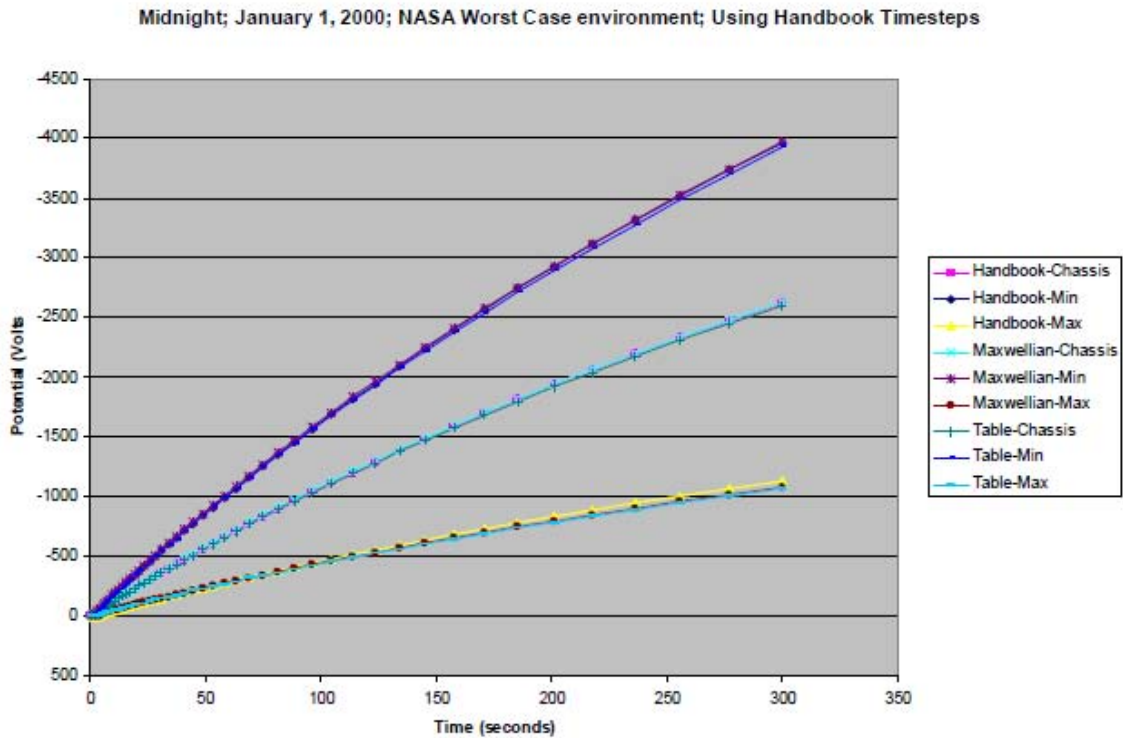
Figure 61. Comparison of Minimum, Maximum, and Chassis Potentials as a Function of Time Computed in Three Different Ways for Midnight on January 1, 2000

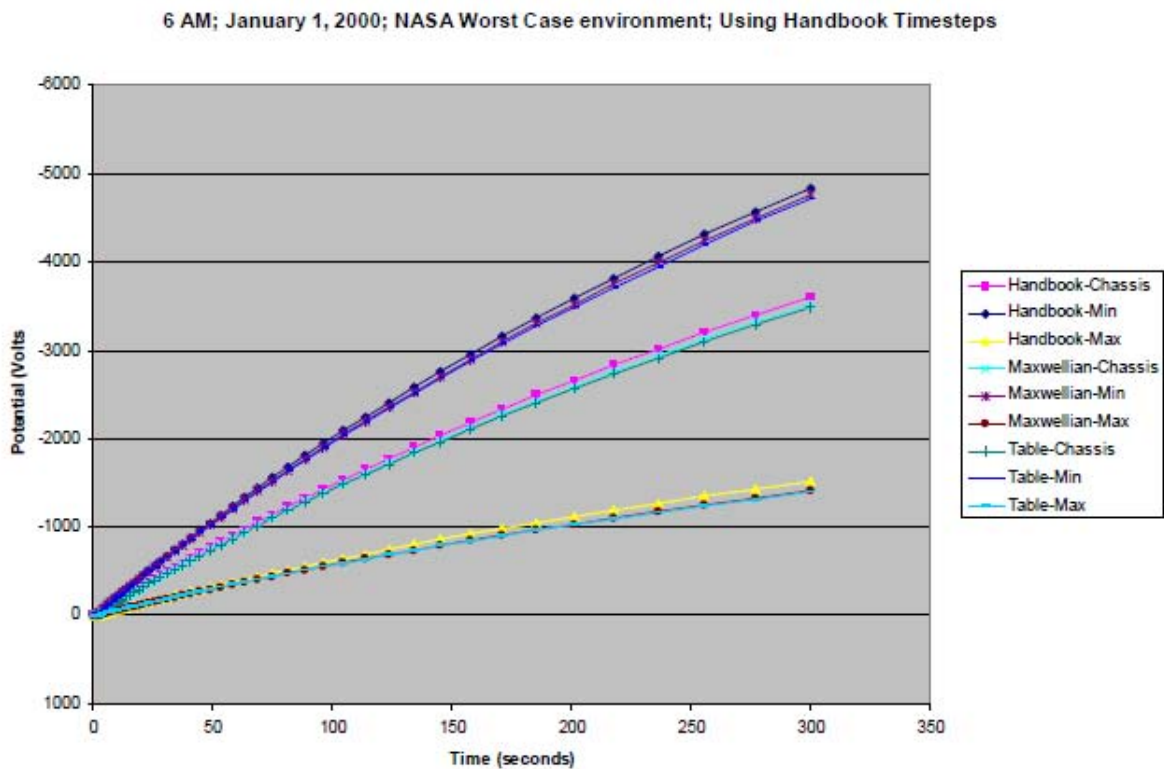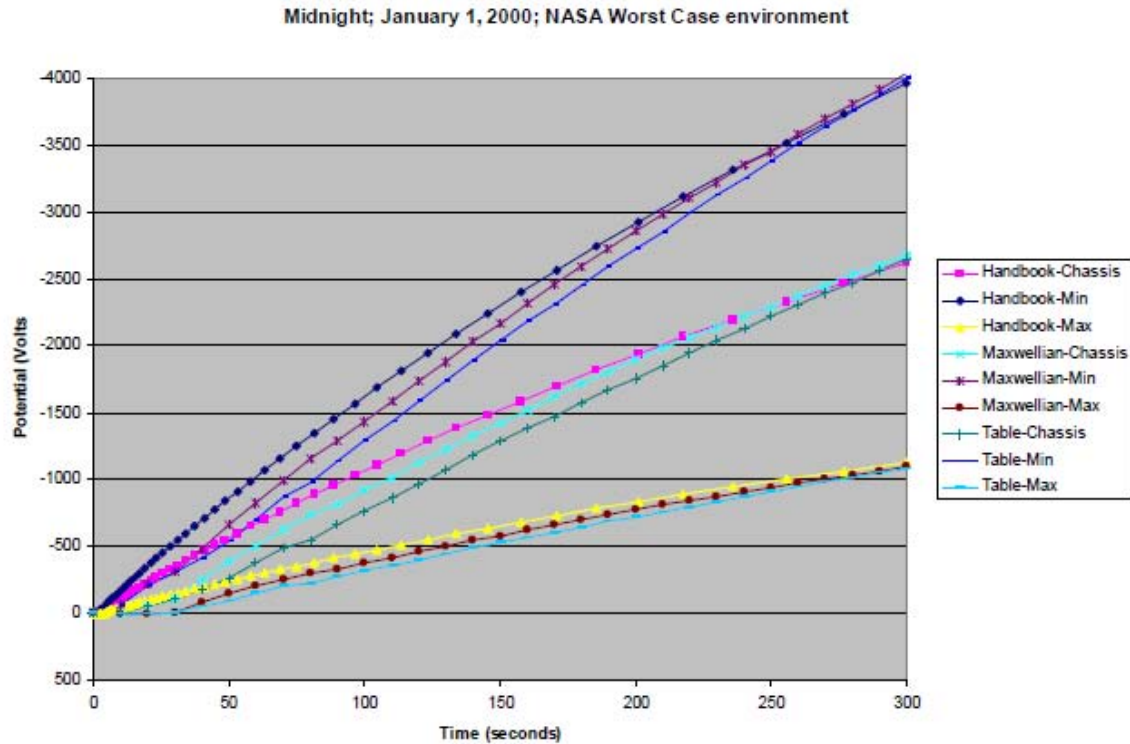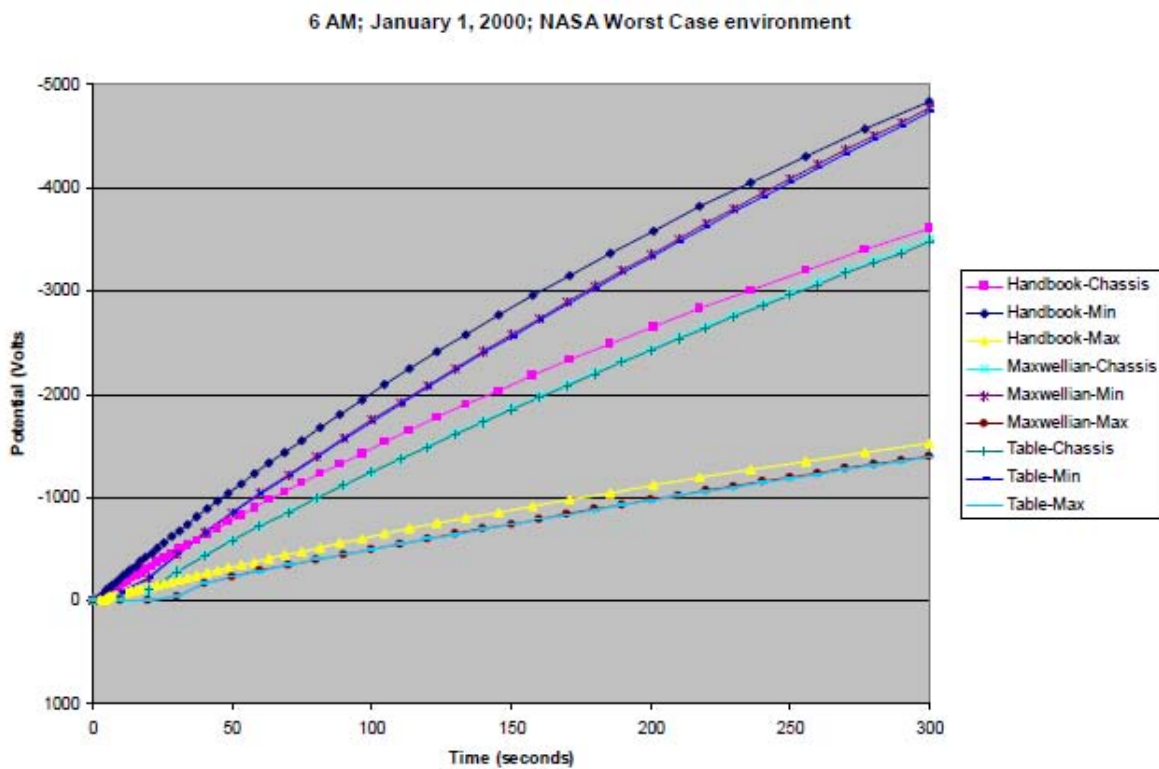6 AM; January 1, 2000; NASA Worst Case environment

Figure 62. Comparison of Minimum, Maximum, and Chassis Potentials as a Function of Time Computed in Three Different Ways for 6 a.m. on January 1, 2000

64

8.5 Details of Selected Classes

Nascap-2k RealTime Prototype is pure java and is based on the code used in the *SEE Interactive Spacecraft Charging Handbook*. The code that performs the calculations is contained in the packages BEM, lapack and SEE. The main driver code that handles reading and writing of files, setting up the calculations, etc., is in the package com.saic.charging. The code also uses some classes in the SAIC libraries Utils, SpaceXML, and MxOrbits. The entire source is included, so the code can be modified and new jars can be built.

The main driver class is *com.saic.charging.ChargeMain*. The method *run()* handles initialization and time stepping of the calculations.

The configuration file is read in and its data is stored in the class *SatelliteConfigFileReader*. The environments are read using the *EnvironmentMapReader* class. The method that handles reading in the tabular data is *EnvironmentMapReader.getEnvironmentMapFromTextFile()*. This method reads data from an MSM file and produces a map that contains *EnvironmentData* objects calculated from the data on the file with the dates of the environments as the keys for the map.

This method is strongly tied to the format of the data supplied in the environment file and this method will need to be changed with any change to that format.

The *EnvironmentData* objects can hold either a Maxwellian or a tabular environment along with the position and additional environment data that is stored in the java class *ExtraEnvironmentData*. The *ExtraEnvironmentData* class currently has the Eclipse indicator that is used in the charging calculation along with the lsh and bb0 values that are read from the MSM files, but not used in the calculations. The *EnvironmentData* class has a method *hasSameValuesAs()* that is used to determine if two environments are the same. This method may need to be modified if there are changes to the format of the Environment data. It also has a method *writeToXml()* to write the environment to the output data files.

The class *SystemStateRecorder* handles writing the state of the system to the xml files and can be changed to modify what is written.

The SUR file contains the data that the real-time charging code provides to the analysis system. It is written in the method *writeSURFile()* of the main class *ChargeMain*. The file name, data written and format of the data are as described in *Interface Control Document for The SEEFS Satellite Charging/Discharging Product* dated May 11, 2005. The data in the SUR file that is calculated by the real-time charging code are the chassis potential, the largest magnitude positive and negative potential differences from the chassis potential and the confidence levels.

9. MEO RADIATION

We performed an extensive analysis of the data from the CRRES MEA and HEEF electron detectors, obtaining pitch-angle distributions of the form $j(\alpha) = j_{90} \sin^n \alpha$, where:

α = particle pitch angle, degrees

$j(\alpha)$ = directional flux at pitch angle a (*e.g.*, in #/cm^2-s-sr-keV)

j_{90} = directional flux at a pitch angle of 90°; also called j_{perp}.

n = anisotropy factor

The parameters j_{90} and n were obtained by performing a least-squares fit to the measured pitch-angle distributions. In performing these fits, we also identified cases where (a) the measured distribution was classified as a "butterfly" distribution, *i.e.*, the flux measured near $\alpha \approx 45^\circ$ was higher than that near 90°; and (b) the measured distribution could not be adequately described as a butterfly distribution or a sin^n α distribution.

These pitch-angle fits were performed on one-minute averages of the raw data. Once the one-minute averages were fit, the fits were binned in L. In order to investigate the effect of geomagnetic conditions, the fits were also binned in Kp. The results of these statistically averaged and binned fits are shown in Figure 63 to Figure 66. These figures show the HEEF measurements at 1.6 MeV and the MEA measurements at 1.58 MeV. The following observations are made from these figures:

- For both HEEF and MEA, n tends to increase with geomagnetic activity

- For both instruments, j$_{\text{perp}}$ is weakly dependent on geomagnetic activity, peaking for Kp of about 3-4.

- For both j_{perp} and n, both instruments agree reasonably well for L > 4. For L < 3.5, the two instruments give very different results.

Figure 67 and Figure 68 compare the HEEF and MEA average n and j_{perp} as a function of energy at one L value. The energy ranges of the two instruments overlap from approximately 0.65 to 1.6 MeV. In this overlap range, the anisotropy parameter n is consistent between the two instruments, within the uncertainty in the averages, but the n derived for HEEF increases with energy, while that for MEA remains fairly constant. The energy spectrum in Figure 68 shows that the value of j_{perp} derived from the two instruments is consistent within the range of overlap, but that the flux drops off quickly with energy at energies above the region of overlap. This trend may be consistent with other measurements and models.

Figure 63 to Figure 68 show results of binned and averaged PAD fits. Figure 69 to Figure 72 show details of individual 1-minute average PADs. Figure 69 and Figure 70 compare directional fluxes and PAD fits for MEA and HEEF at two energies. In these figures, the symbols represent the measured directional flux, and the pink lines show the PAD fit.

The fitting parameters are given at the top of the figure. Figure 71 shows a "typical" butterfly PAD (in this case measured by MEA), and Figure 72 shows a typical PAD which was rejected by the fitting procedure.

Figure 63. Average Anisotropy Parameter n as a Function of L and Kp for HEEF 1.6-MeV Channel
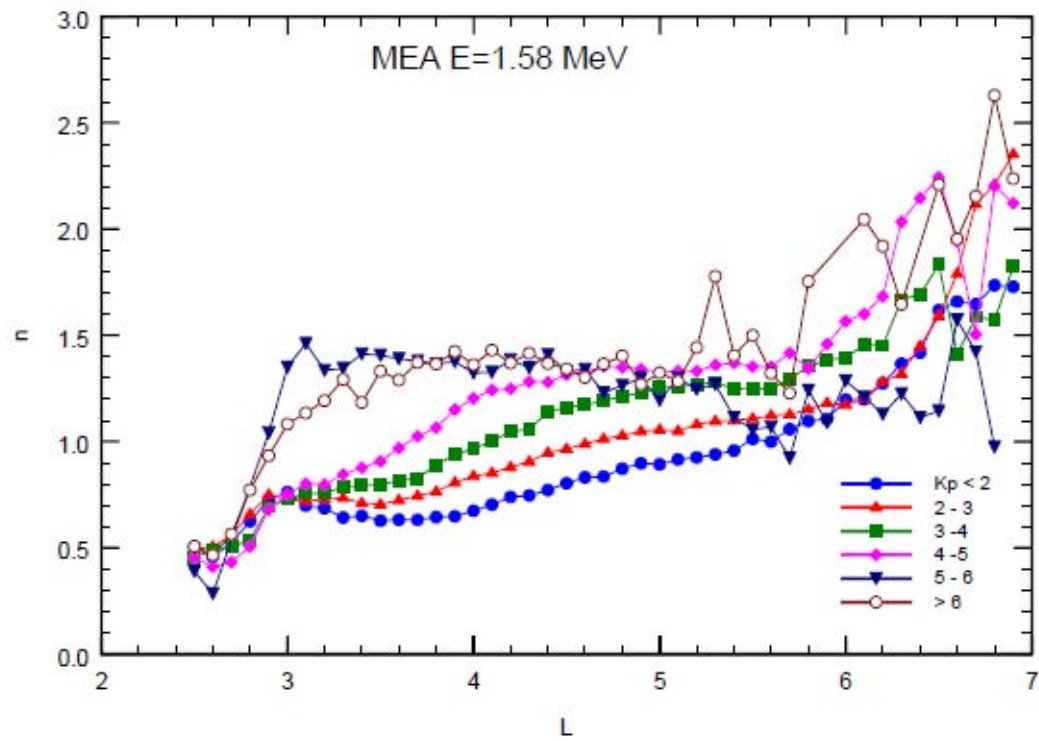
Figure 64. Average Anisotropy Parameter n as a Function of L and Kp for MEA 1.58-MeV channel

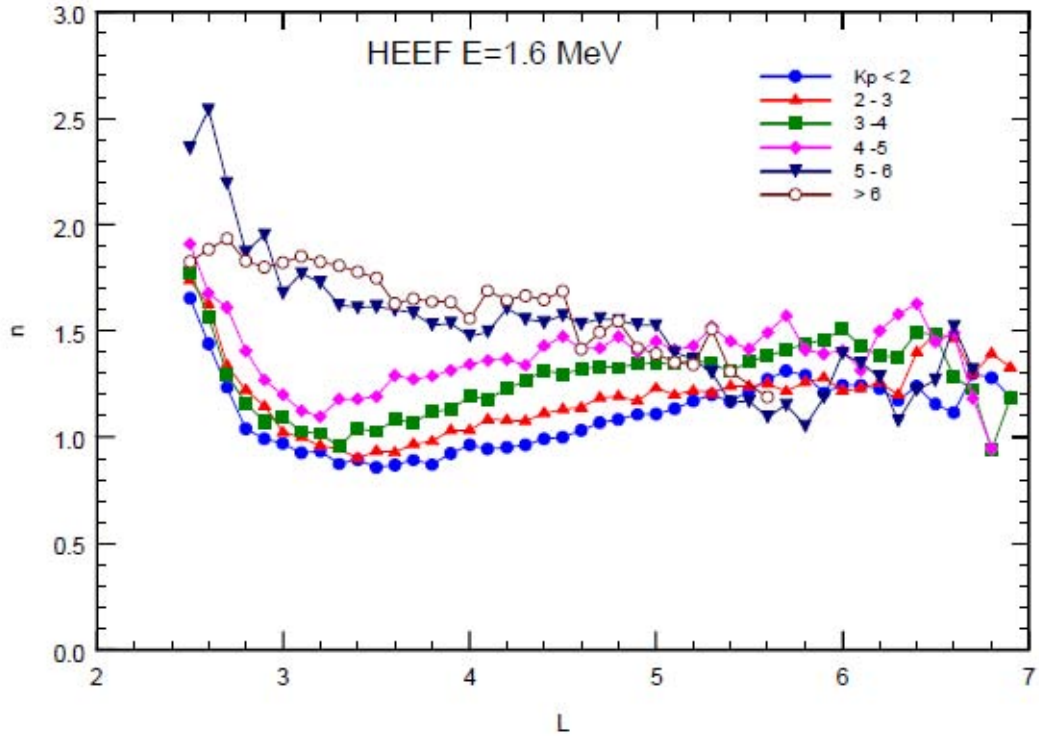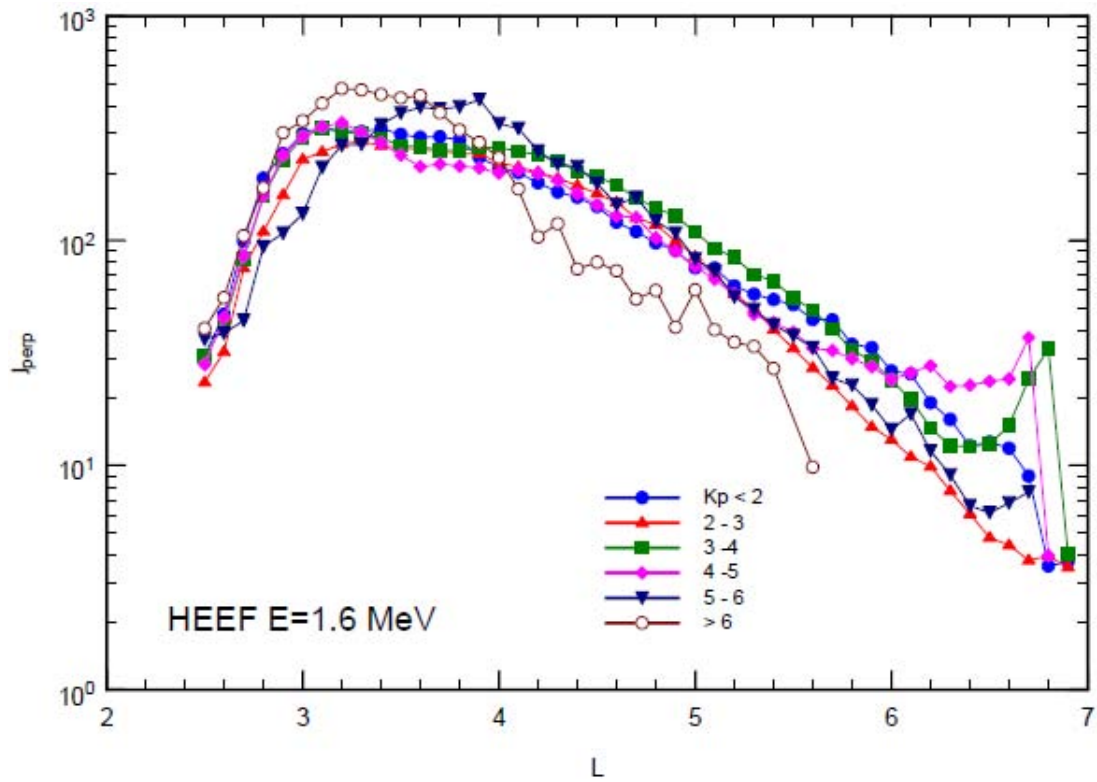**Figure 65. Average jperp as a Function of L and Kp for HEEF 1.6-MeV Channel**
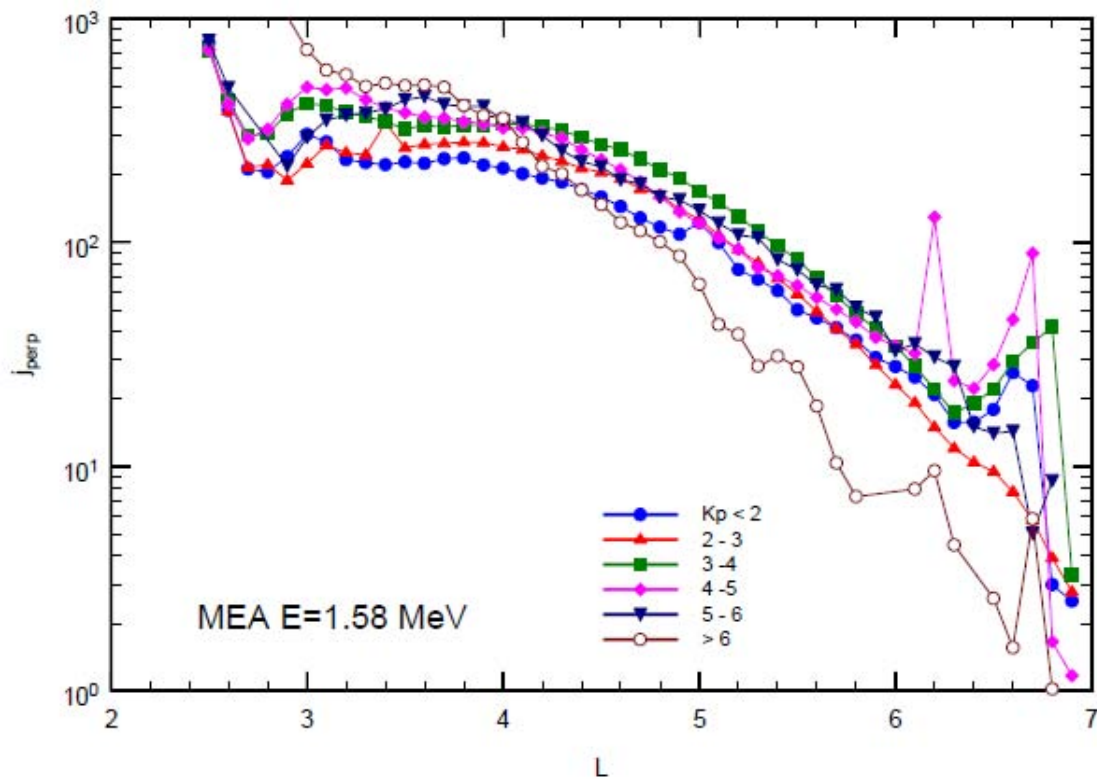
Figure 66. Average jperp as a Function of L and Kp for MEA 1.58-MeV Channel
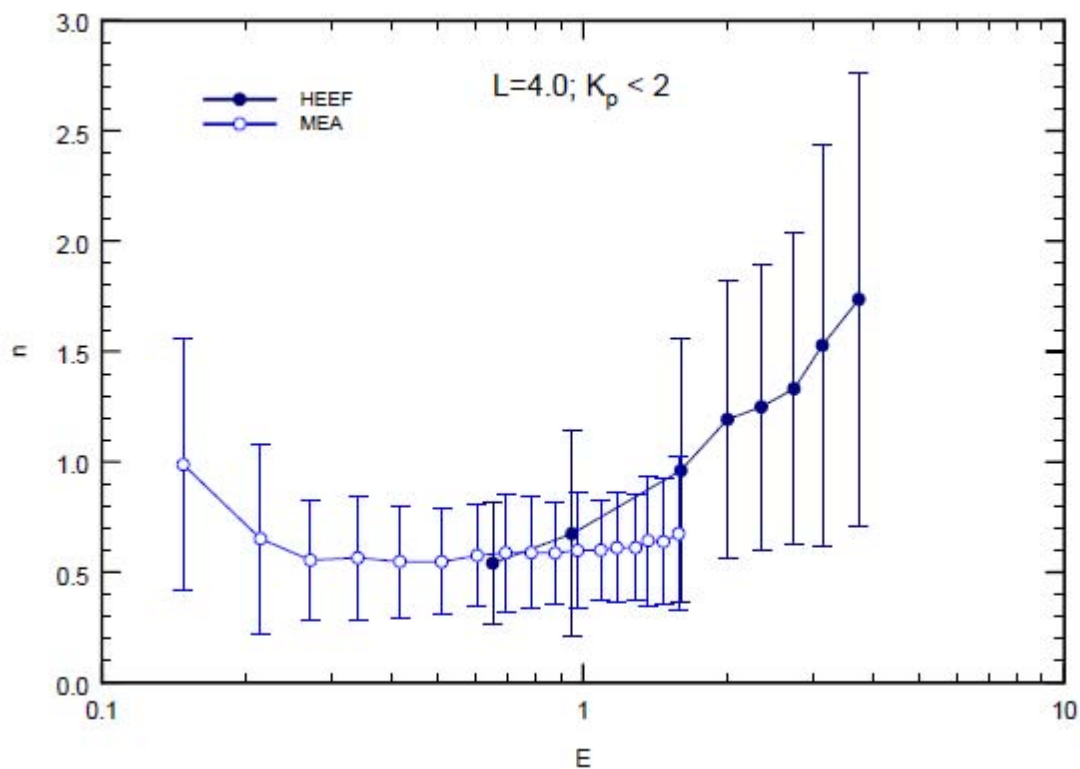
Figure 67. Average Anisotropy Parameter as a Function of Energy for HEEF and MEA
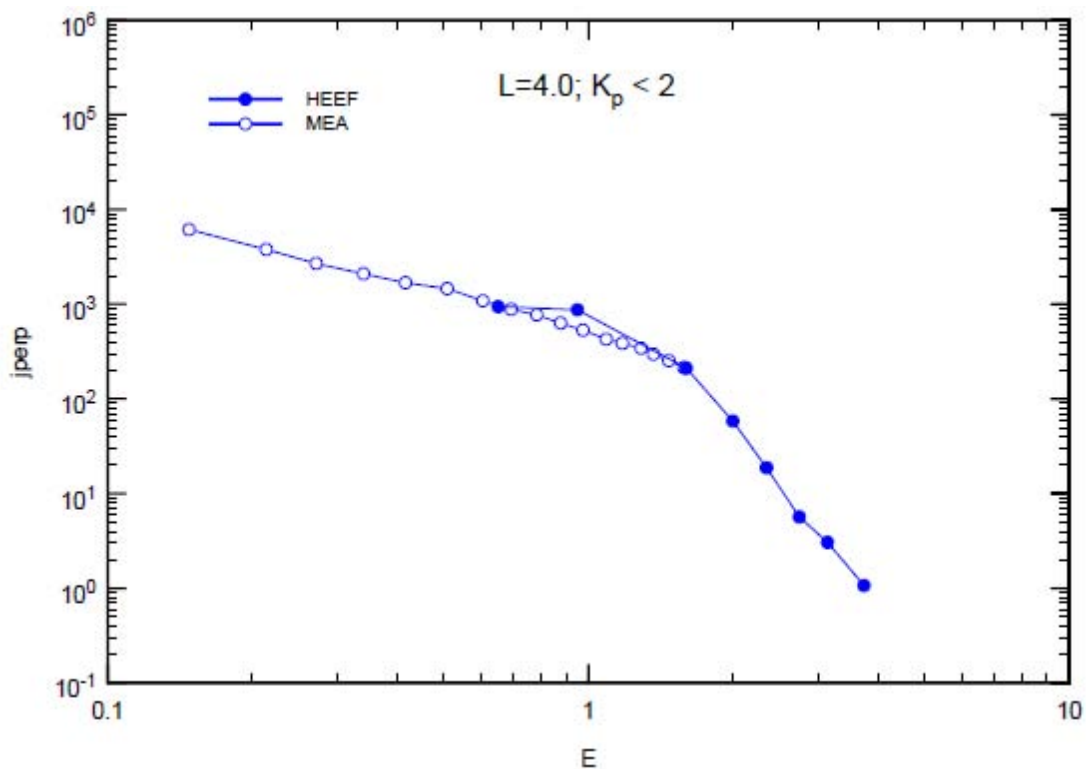
Figure 68. Average jperp as a Function of Energy for HEEF and MEA
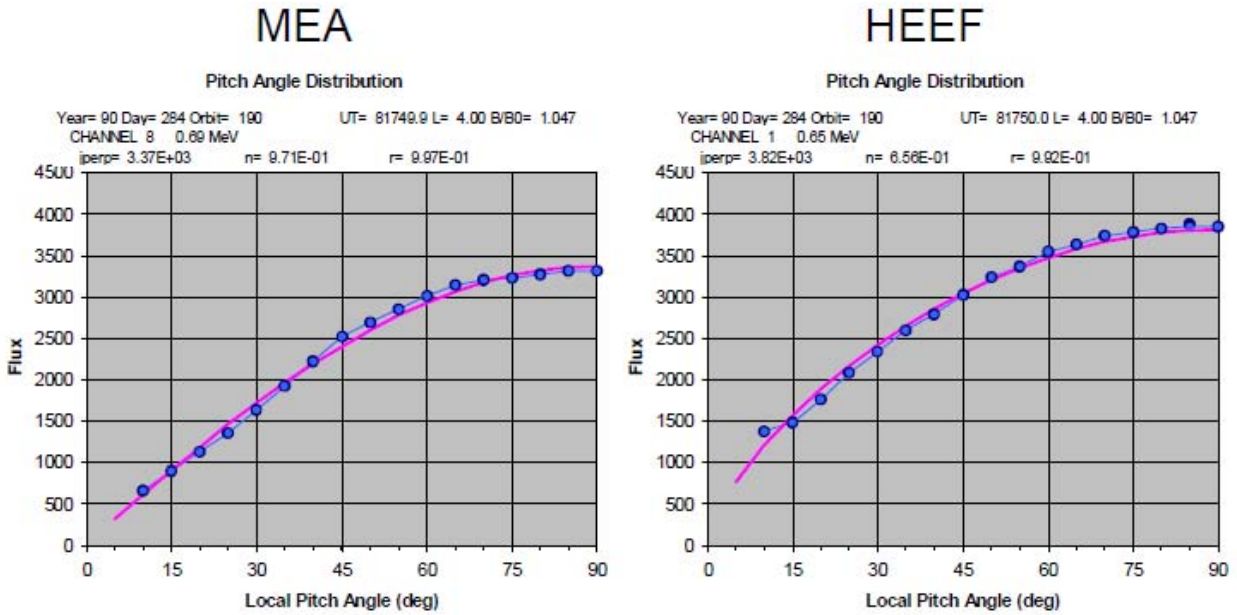
Figure 69. Comparison of "Typical" Pitch-Angle Distributions for MEA (Left) and HEEF (Right), ~ 0.67 MeV
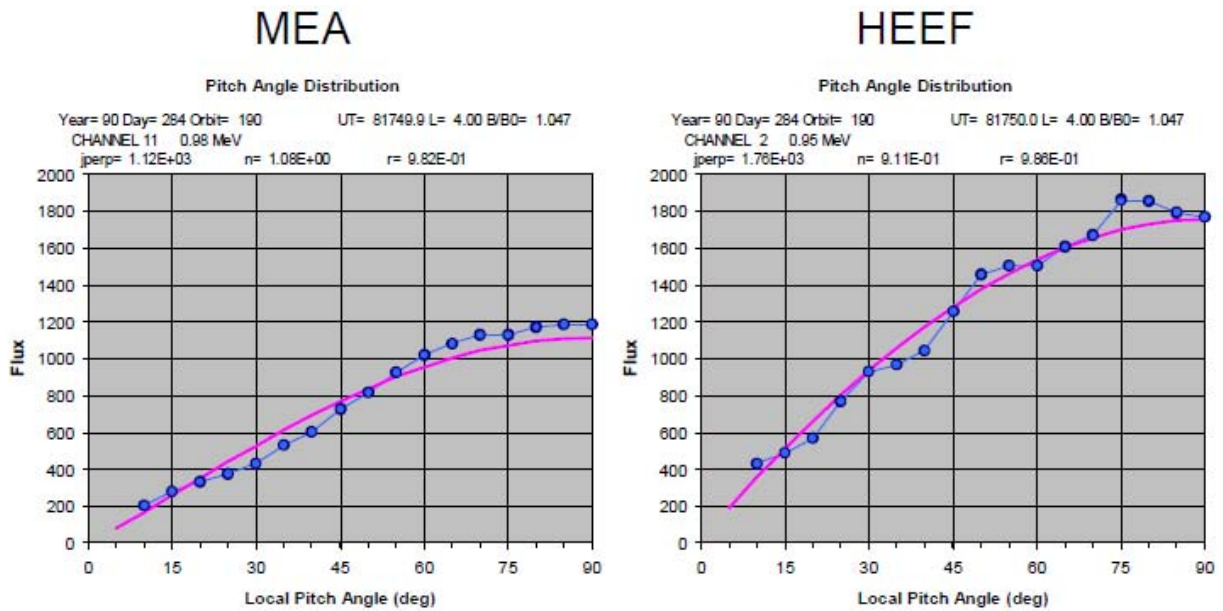
Figure 70. Comparison of "Typical" Pitch-Angle Distributions for MEA (Left) and HEEF (Right), ~ 0.96 MeV

Pitch Angle Distribution

Year= 90 Day= 284 Orbit= 190   UT= 80370.1 L= 3.28 B/B0= 1.012
CHANNEL 8   0.69 MeV
jperp= 1.02E+02   n= 6.33E-01   r= 9.19E-01
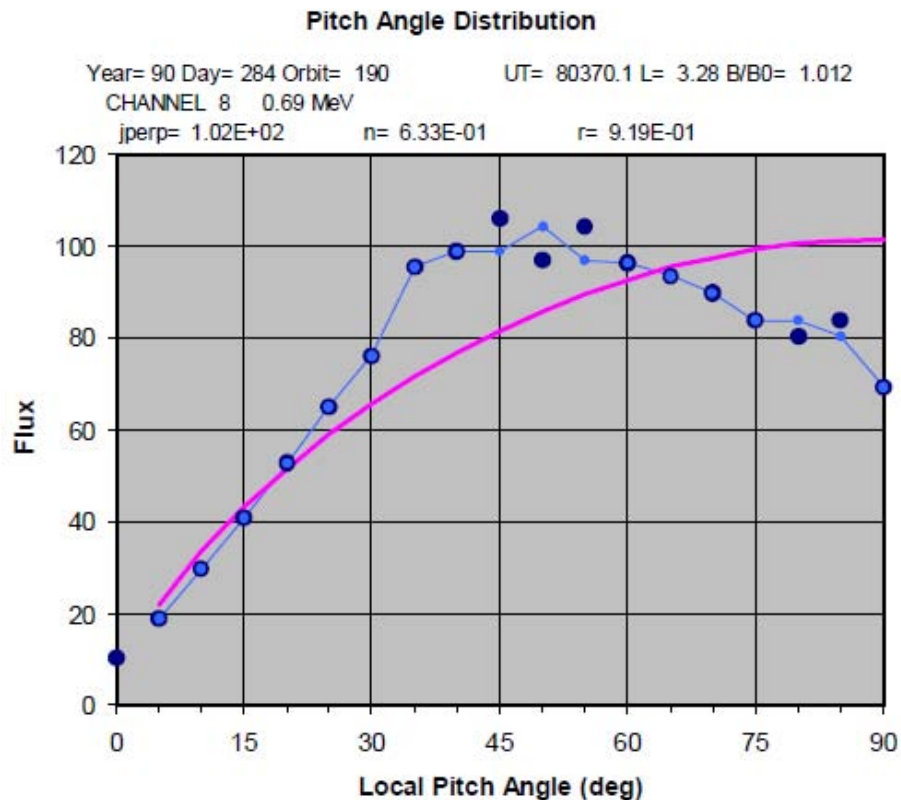
Figure 71. "Typical" Butterfly Distribution (from MEA 0.69 MeV Channel)

Pitch Angle Distribution

Year= 90 Day= 284 Orbit= 190   UT= 79650.0 L= 2.86 B/B0= 1.001
CHANNEL 8   0.69 MeV
jperp= 1.02E+00   n= -2.28E-01   r= -2.10E-01

Figure 72. "Typical" Rejected Pitch-Angle Distribution

71

10. SELF-CONSISTENT DSX CALCULATIONS

The DSX dipole antenna transmitter has two elements, each several centimeters in diameter and 40 meters long. Due to the ease of electron collection by positive objects, the positive element is at near zero or small positive potential relative to the ambient ionosphere, while nearly the full applied potential appears on the negative element. Because the frequencies of interest are comparable to the ion plasma frequency, the sheath structure is at some intermediate state between the "ion matrix" or "frozen ion" limit (which assumes the ions are stationary and contribute ambient ion density to the space charge) and the equilibrium space charge limit (in which the ions assume a steady-state space charge limited distribution of charge and current). Thus, calculation of the sheath structure and of ion collection by the antenna elements requires dynamic (specifically, particle-in-c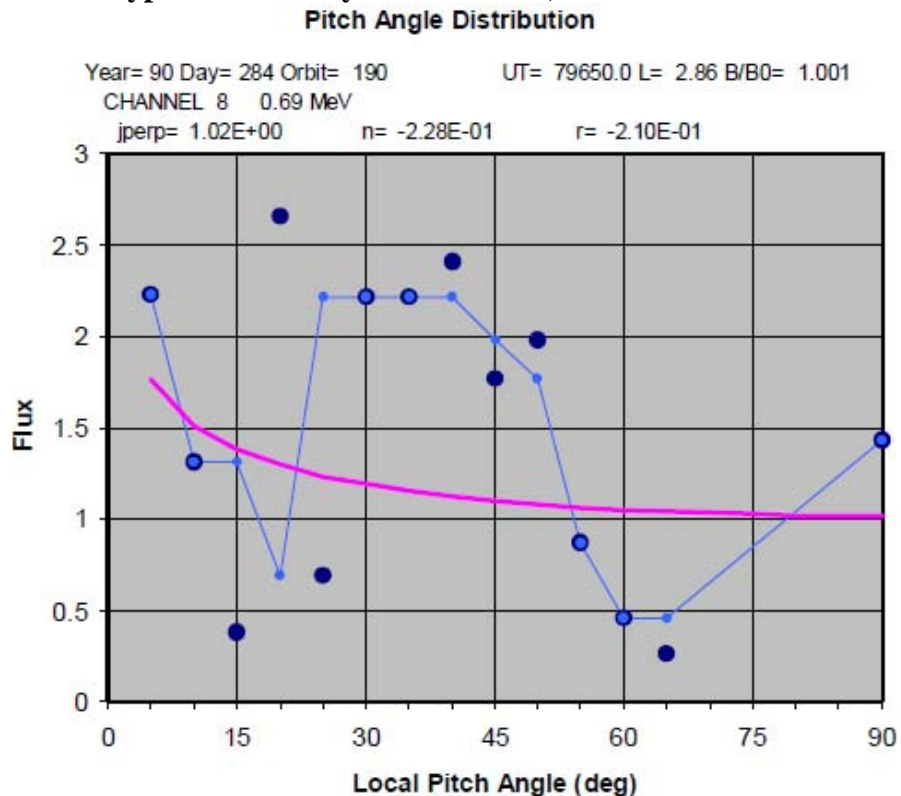ell, PIC) treatment, at least for the ions. *Nascap-2k* can be used to perform all four simulations of interest: (1) equilibrium space charge sheath; (2) "frozen ion" sheath; (3) dynamic PIC ions with fluid (Boltzmann or barometric) electrons (hybrid PIC); (4) dynamic PIC ions and electrons (Full PIC). One- and three-dimensional Full PIC calculations [3] and three-dimensional hybrid PIC calculations [4 & 5] were reported at Spacecraft Charging Technology Conferences in 2003, 2005 and 2007. Recent improvements in *Nascap-2k* allow us to perform higher fidelity simulations and better explore their implications than was previously possible. The calculations reported here use an updated geometric model, have a larger computational space, include a larger number of macroparticles, and have improved resolution about the antenna.

The plasma is modeled using the hybrid PIC approach with PIC ions and fluid barometric electron densities. The plasma response, collected ion currents, and chassis floating potential are computed self-consistently with a near-square-wave bias applied to the antenna elements. Particle injection and splitting are used to replenish the plasma depleted at the boundary, represent the thermal distribution, and maintain appropriately sized macroparticles. Limitation of current due to the thermal distribution of ions and the resulting angular momentum barrier are included. The different plasma responses above and below the ion plasma frequency are discussed. The ion current density is also computed. Section 7 discusses the computation of the transverse surface current and the volume electron current.

10.1 Geometry and Grid

The DSX spacecraft shown in Figure 73 consists of an EELV Secondary Payload Adapter (ESPA) ring to which the Avionics Module and the Payload Module are attached. The Avionics Module is essentially the spacecraft bus and includes a deployable solar array. The Payload Module contains most of the DSX specific components. Of interest here are the Y and Z antenna masts, both built by ATK Space Systems Inc. The Y antenna is 80 meters in length (tip-to-tip) and functions as a VLF receive and transmit antenna. The DSX Z antenna is 16 meters in length (tip-to-tip) and functions as a VLF receive antenna in a cross-dipole configuration with the Y antenna. The Y antenna boom is a truss consisting of Graphite-Epoxy (Gr/Ep) longerons and batten elements with steel diagonals. Copper wire is run the full length of each truss's three longerons, attached at every other joint. The Z antenna boom is a similar truss with S-2 glass (fiberglass) material for the longerons and battens instead of the Gr/Ep. [6]
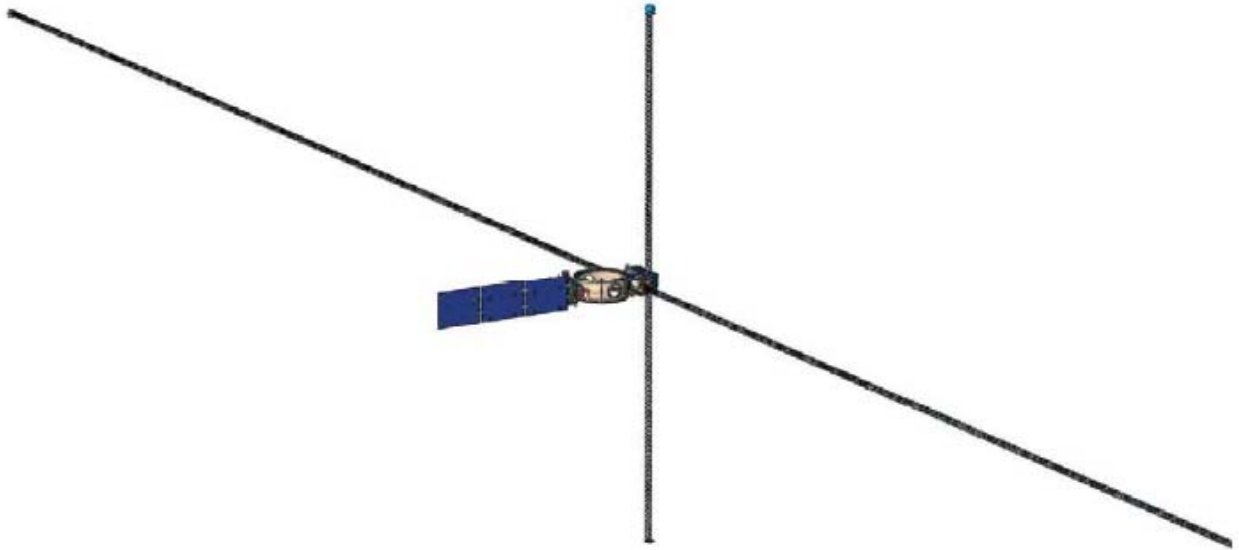
Figure 73. DSX Spacecraft

The *Nascap-2k* model used is shown in Figure 74 and Figure 75. The antenna elements are six-sided, 0.1 m diameter cylinders. This diameter was chosen to match the capacitance of the ATK mesh boom. The antenna elements are 76% transparent to match the collecting area of the ATK booms. The solar array is 4.2 m by 1.15 m by 0.1 m. The $18\times34\times18$ volume grid is shown in Figure 76 and Figure 77. The mesh unit of the outermost grid is 4.72 m, and the mesh unit of the innermost grid is 14.75 cm.

Figure 74. *Nascap-2k* **Model of DSX**
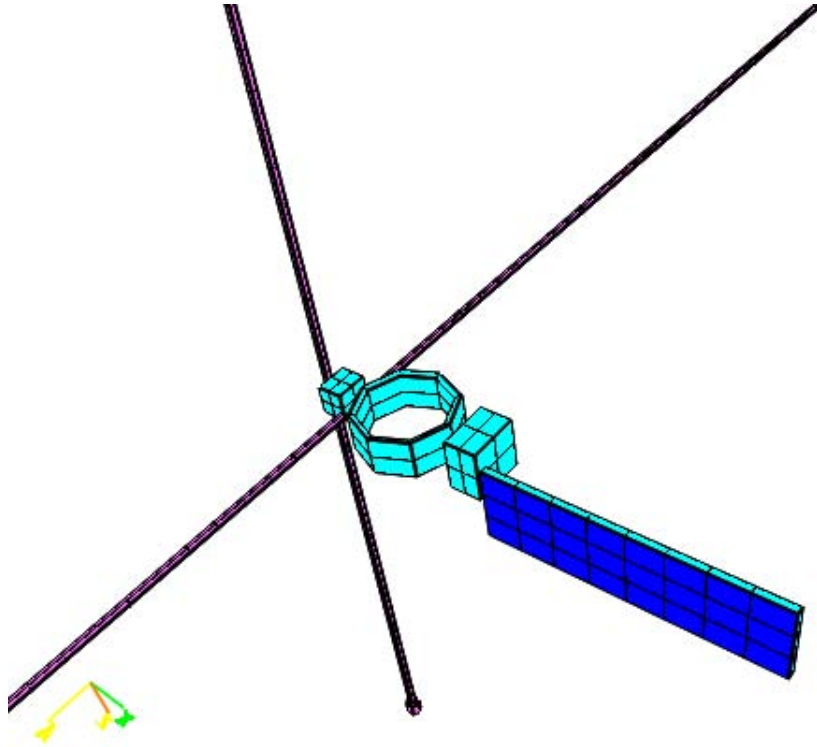
Figure 75. Expanded View of Center Portion of *Nascap-2k* Model of DSX
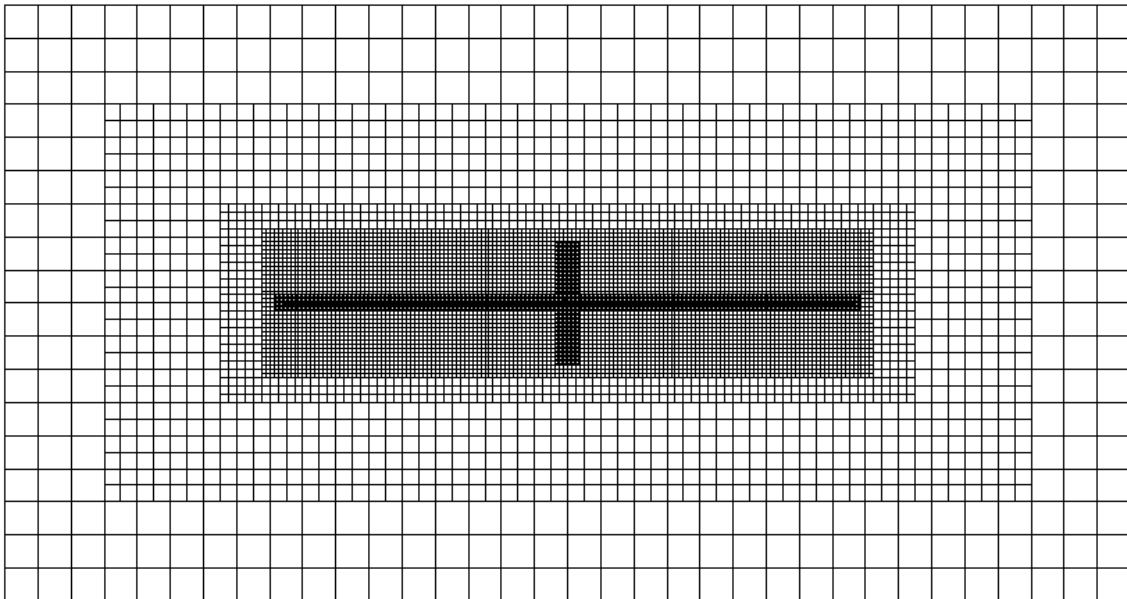
Figure 76. Grid Used for DSX Calculations
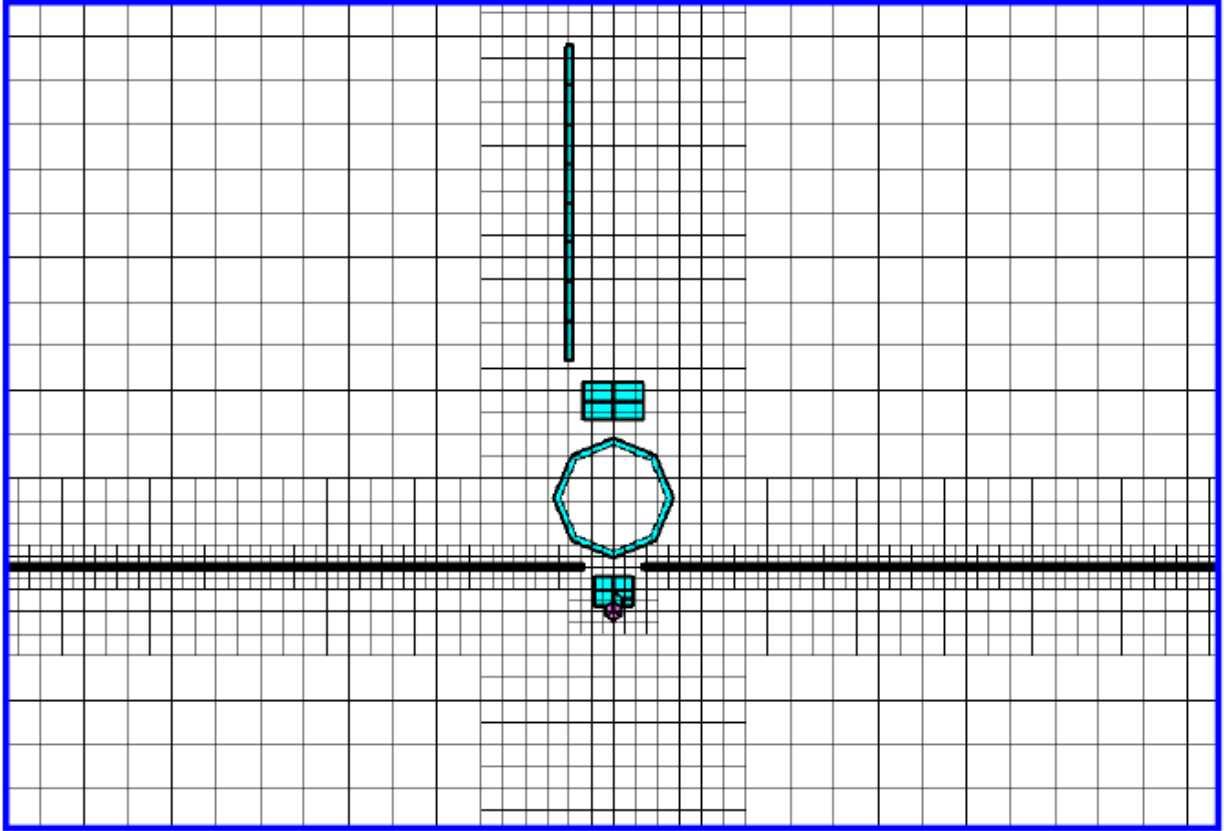
Figure 77. Close-up of Center of Grid Used for DSX Calculations.

10.2 Calculation Parameters

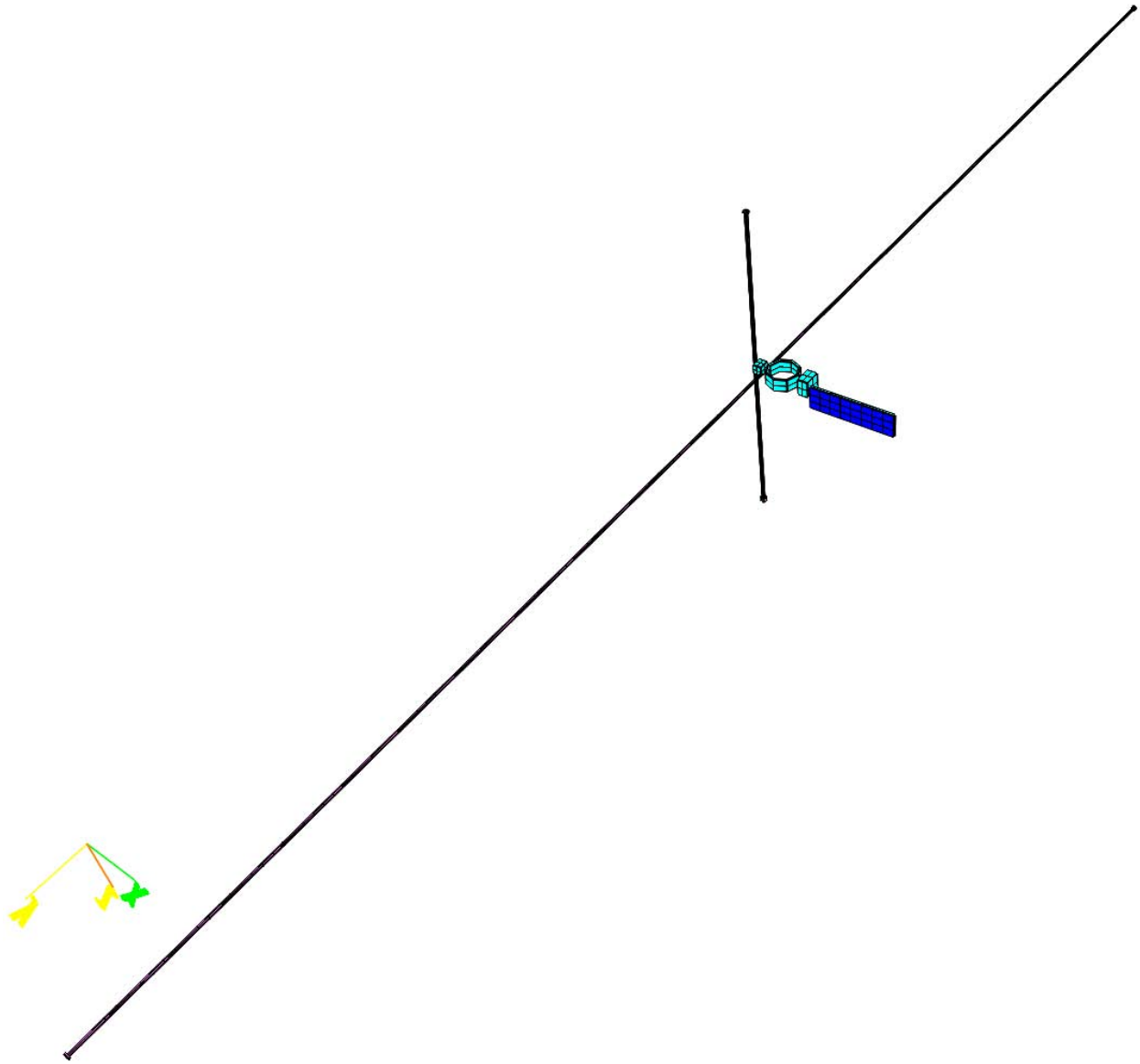The parameters of the calculations are shown in Table 4. For the low density case (Case 1) we simulated the applied frequency above the ion plasma frequency only. For the high density case we simulated the system both above (Case 2) and below (Case 3) the ion plasma frequency. One antenna element is floating and the other has a variable bias with respect to the first. The other components all float together. Floating potentials adjust automatically to account for incident plasma current. The applied bias consists of the first two Fourier components of a square wave with amplitude of 1 keV and the indicated frequency. The shape is shown in Figure78. The timestep is set so that there are 50 timesteps per cycle.

Table 4. Parameters of Calculations Shown

|	Case 1	Case 2	Case 3
Density (m^{-3})	10^8	10^9	10^9
Temperature (eV)	1	1	1
Species	H$^+$	H$^+$	H$^+$
Plasma frequency (kHz)	2	6.6	6.6
Frequency (kHz)	10	12	2
Splitting of initial macroparticles	All grids	All grids	All grids
Splitting on subgrid entry	When needed	When needed	When needed
Macroparticle injection	Every 42 timesteps	Every 50 timesteps	Every 8 timesteps
Number of macroparticles (millions)	20 to 80	20 to 45	20 to 30
Ion current (mA) (mean value during "on" state)	0.06	0.41	0.24
Phase shift between plasma current and applied voltage	11°	13°	-13.5^o
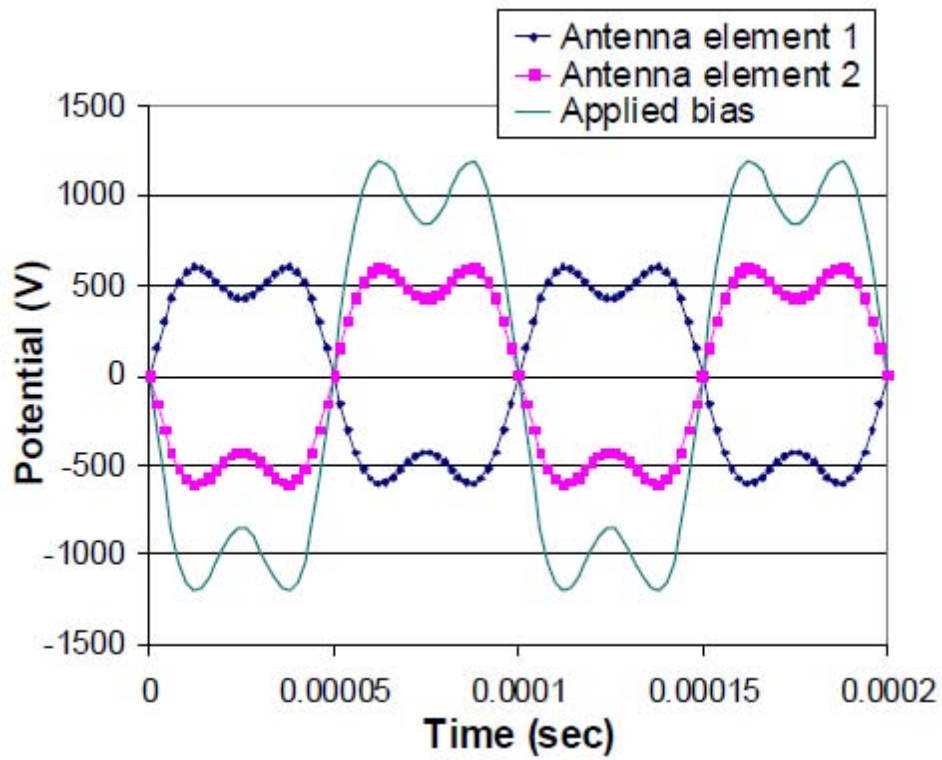
Figure 78. Applied Bias Values and Resulting Antenna Element Potentials in the Absence of Plasma

10.3 Particle-in-Cell Techniques

Nascap-2k has primarily been used to model quasi-static phenomena. However, there are many physical processes of interest whose timescales require a dynamic approach such as a PIC technique. Examples of such processes are breakdown phenomena, plasma kinetics, and sheath structure about surfaces with potentials that change on a timescale comparable to the time it takes an ion to cross the sheath. PIC techniques can also be used to address problems in which analytic representations of the environmental currents are inadequate, such as in a spacecraft wake or in a cavity. A steady-state PIC technique, in which the ion space charge density is computed from macroparticles tracked from the boundary of the computational space until they are collected or exit the computation space, was successfully used to model the CHAWS experiment. [7] In addition, PIC techniques can be useful when developing analytic models. To facilitate these modeling techniques, the ability to perform various types of PIC calculations was built into *Nascap-2k*.

In a hybrid PIC calculation, the problem is initialized by creating ion macroparticles throughout the grid to represent a constant particle density. The ion macroparticles are tracked for one timestep and then volume potentials are computed using the resulting ion density and a barometric electron density. The process is repeated for the time period of interest. In a full PIC calculation both electron and ion macroparticles are tracked and volume potentials are computed using the resulting plasma density.

The barometric potential is defined by $\phi_b = \theta \ln(\rho_i/en)$, where n and θ are the ambient plasma density and temperature and ρ_i is the local ion density (obtained from tracking). At plasma potentials below ϕ_b, the electron density is the barometric electron density and above ϕ_b, the electron density linearly increases. Charge stabilization is then applied. [8]

$$\frac{\rho}{\varepsilon_o} = \frac{\rho_i}{\varepsilon_o} - \frac{e\,n}{\varepsilon_o} \begin{cases} \exp\left(\phi/\theta\right) & \text{for } \phi \le \phi_b \\ \exp\left(\phi_b/\theta\right)\left(1 + \dfrac{\phi - \phi_b}{\theta}\right) & \text{for } \phi > \phi_b \end{cases}$$

[3]

To replace macroparticles that are collected by the probe or escape from the grid, it is necessary to periodically inject macroparticles from the boundary. This allows for the calculation of current for longer time periods. In hybrid PIC calculations without boundary injection, the low field region near the boundary of the problem develops a significant negative potential due to ion depletion. Boundary injection keeps these potentials near zero by replenishing the ions that have been collected or escaped.

Macroparticles may be split when they enter a more finely resolved region or when they are created either at the boundary or throughout the volume at problem initialization. There are two major reasons for splitting macroparticles: one physical and one numeric. Even at moderate potentials, thermal effects can reduce collected currents. Some particles near the sheath edge have enough thermal velocity perpendicular to the electric field that angular momentum conservation prohibits collection. Particle splitting allows for a representation of the thermal distribution in the initial particle distribution and in particles injected from the boundary. From a numeric point of view, particle splitting can be used to keep the particle weight appropriate to the grid size and to help maintain the smoothness of the distribution. A large particle that originated

in an outer grid is split in velocity in such a way that it preserves the plasma temperature and eventually becomes distributed over several volume elements in an inner grid. Because high-field regions are often of interest, particles are split in velocity space only, as spatial splitting would raise problems with energy conservation. The details are discussed in Reference 5.

10.4 Results

The time history of the surface potentials and tracked ion currents to surfaces for the three calculations are shown below in Figure 79 through Figure 87. In each calculation, there is an initial transient in the potentials and currents. In the low-density Case 1, it takes about 6 cycles until the potential variation of the antenna elements settles down to approximate a square wave of amplitude 500 V about a value slightly more negative than -500 V. In the higher density cases, it takes about one cycle. In all cases, the body goes negative to about -200 V and then returns to zero at a rate that depends on the plasma density.

When the excitation frequency is above the ion plasma frequency (Case 1 and Case 2) the plasma current to an antenna element increases sharply when a potential is applied to the element, and continues substantially into the unbiased half-cycle, as seen in Figure 81 and Figure 84. Below the ion plasma frequency (Case 3) the ion current peaks sharply when the potential is applied, falls off substantially during the half-cycle, and drops sharply to zero when the potential is removed, as seen in Figure87. The difference can be understood in terms of the sheath being depleted of ions within every cycle at low frequency, but not at high frequency. For excitation frequencies below the plasma frequency, the initial burst of ion current depletes the sheath. The lower current levels during the second half of the biasing period are a result of ions being attracted from the sheath edge. This shows up in the phase shift, tabulated in Table 4. The negative phase shift for Case 3 is a result of the current maximum occurring shortly after the onset of the high voltage, while the positive phase shifts for cases 1 and 2 show the delay in current response to the high voltage application. These phase shifts are much less than the ninety degree phase shift expected in the linear regime.
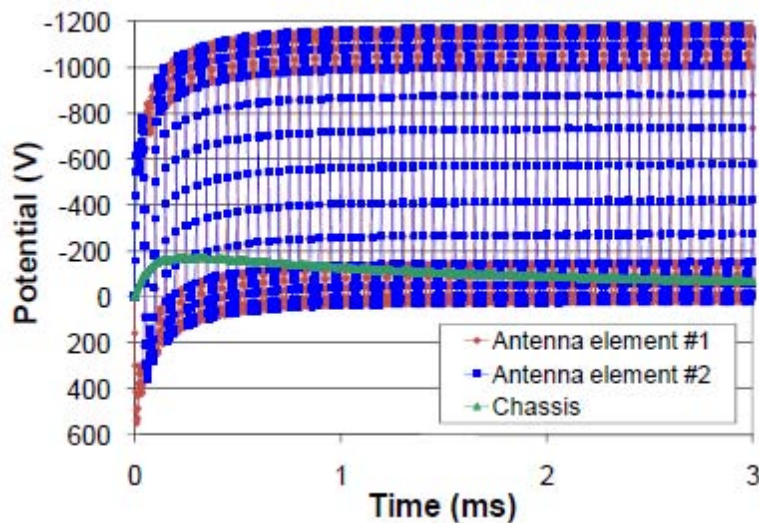

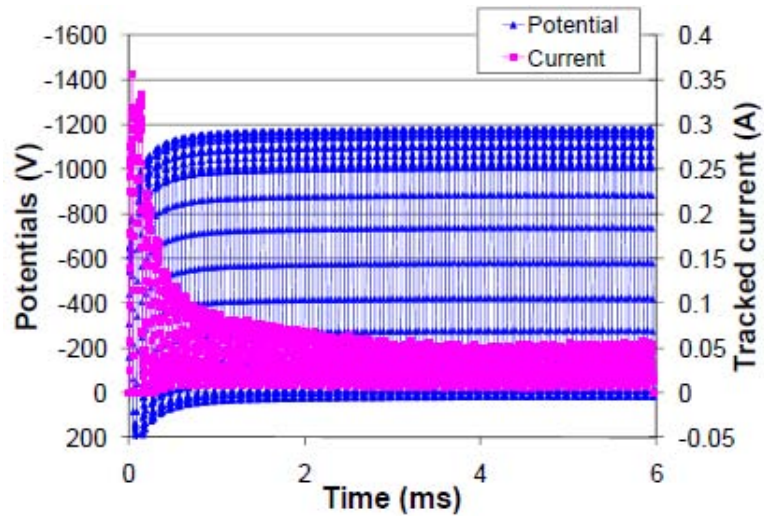**Figure 79. Time Dependence of Antenna Element Potentials for Case 1**

Figure 80. Potential and Collected Ion Current of Antenna Element 2 for Case 1
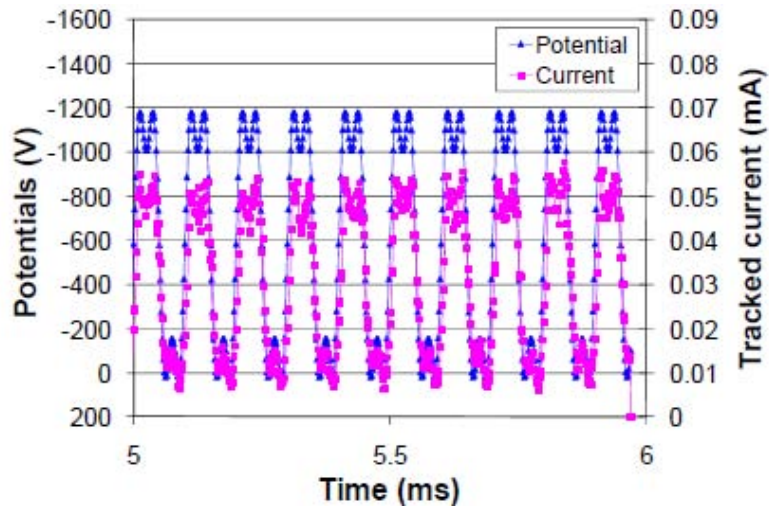

Figure 81. Potential and Collected Ion Current of Antenna Element 2 for Case 1 (Expanded Scale)

Figure 82. Time Dependence of Antenna Element Potentials for Case 2

Figure 83. Potential and Collected Ion Current of Antenna Element 2 for Case 2

Figure 84. Potential and Collection Ion Current of Antenna Element 2 for Case 2 (Expanded Scale)

Figure 85. Time Dependence of Antenna Element Potentials for Case 3

Figure 86. Potential and Collected Ion Current of Antenna Element 2 for Case 3

Figure 87. Potential and Collected Ion Current of Antenna Element 2 for Case 3 (Expanded Scale)
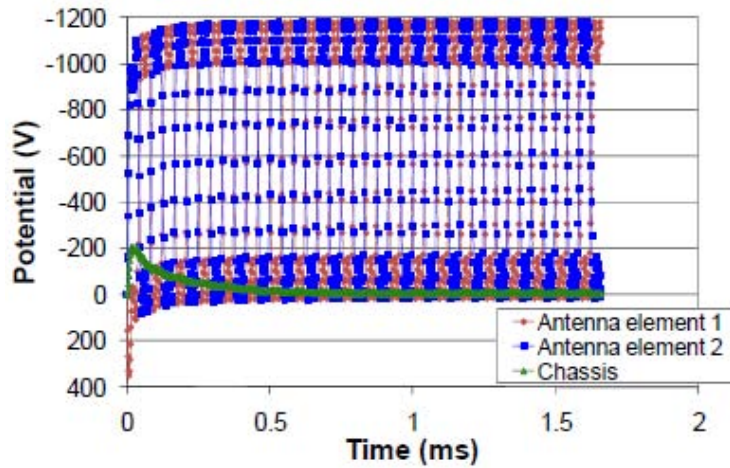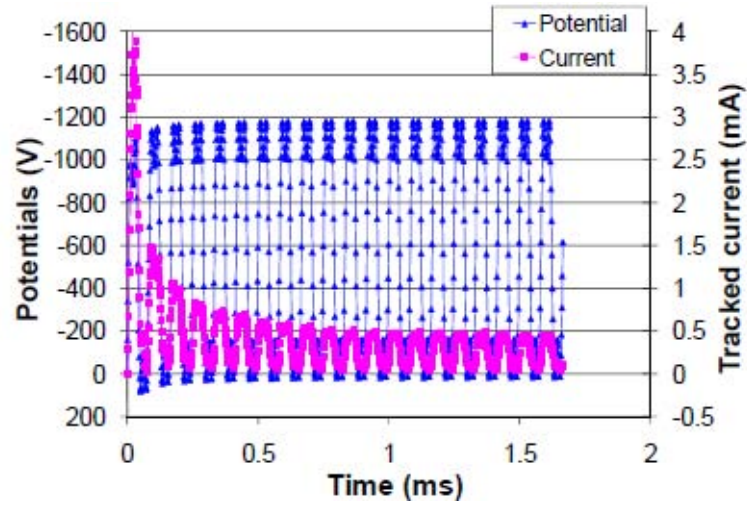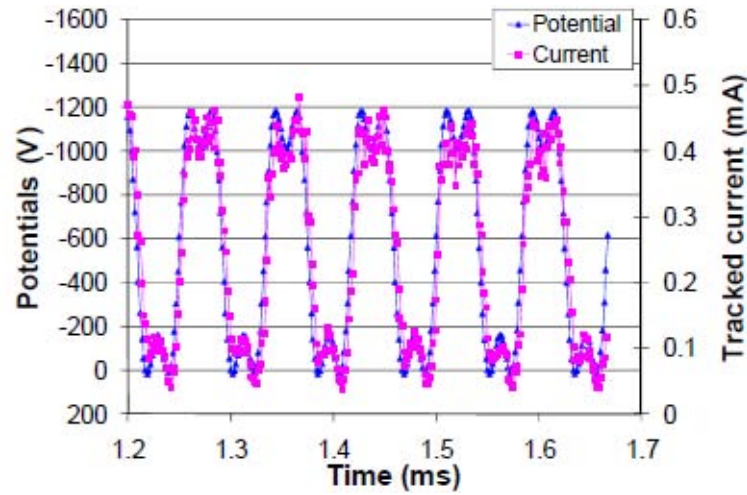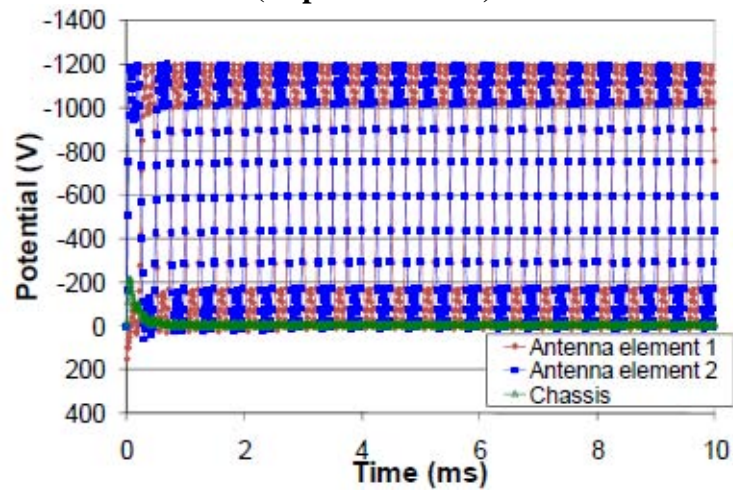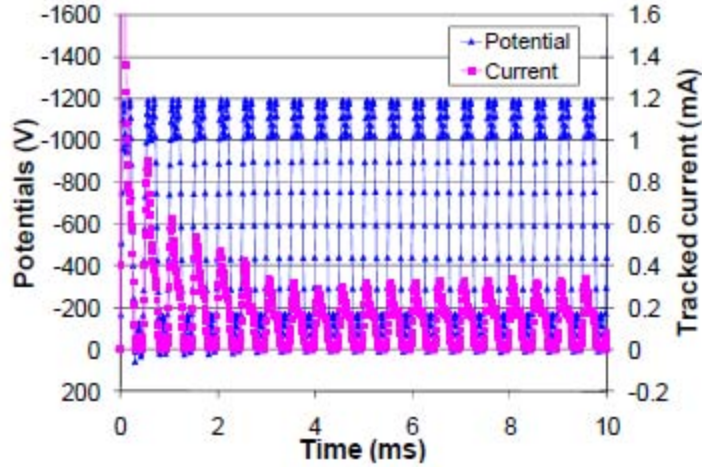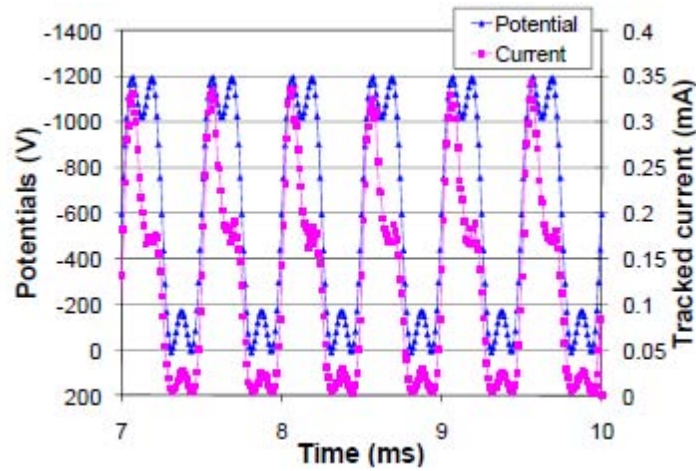
Figure 88 shows the sheath structure in the low density plasma when the potential on one antenna element is at its negative peak at –1.1 kV and the other is positive at +26 V. At this potential and density, the sheath is nearly cylindrical, with a spherical end cap. The sheath envelops the positive antenna element, providing a barrier to electrons, and thus allowing the system to float more positive than might be expected. Presently, this barrier effect on the current collection is *not* modeled. In the immediate vicinity of the antenna, the density is elevated as the ions are attracted to the negative potential. This convergence leaves a slight decrease in density at the edge of the sheath. The elevated density around the positive element is left over from the previous half cycle.

Figure 89 shows the sheath structure when both antenna elements are at the same potential, near –570 V. The sheath is slightly larger about the top element, which had previously been near –1 kV, while a large volume of the lower, previously positive, sheath remains near ambient ion density due to ion inertia effects. In the immediate vicinity of the top antenna element, the ion

density is enhanced by an order of magnitude due to ions that orbit the probe but are not collected. However, throughout most of the sheath the ion density is depressed, leading to less shielding and a larger sheath.

Figure 88. Sheath Structure (Potentials and Densities) for Low Density Calculation at 2.062 ms – Antenna Elements are at –1173 V And +26 V, the Largest Differential of the Cycle – Ambient Plasma Density is 1.8 V m^{-2}
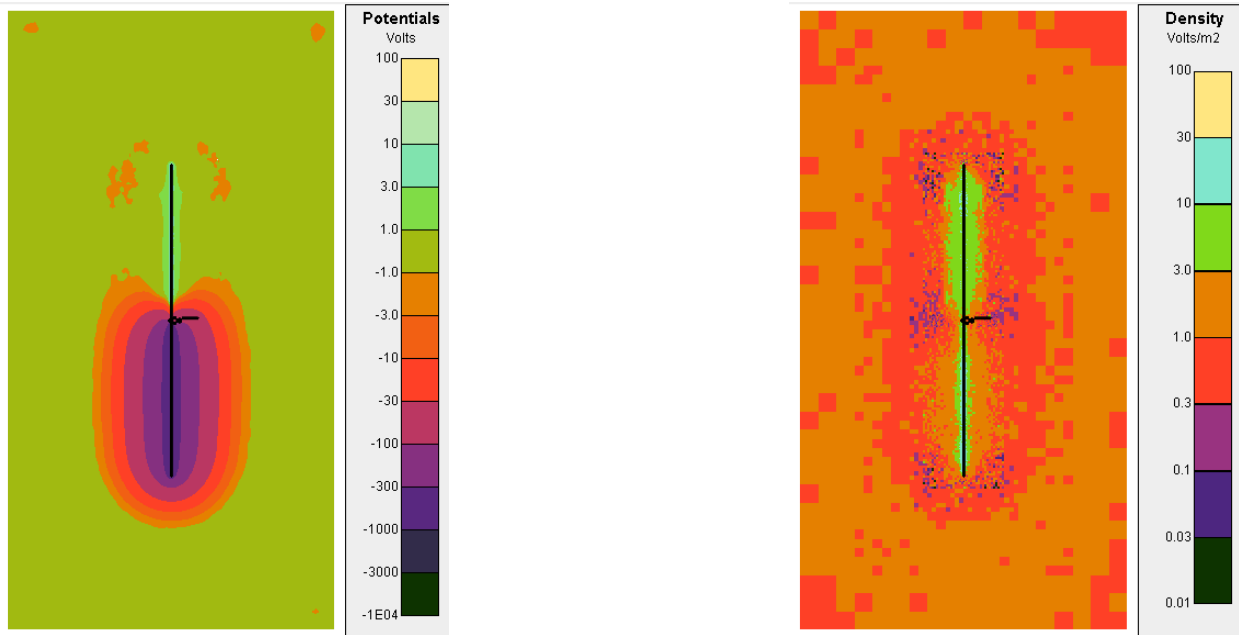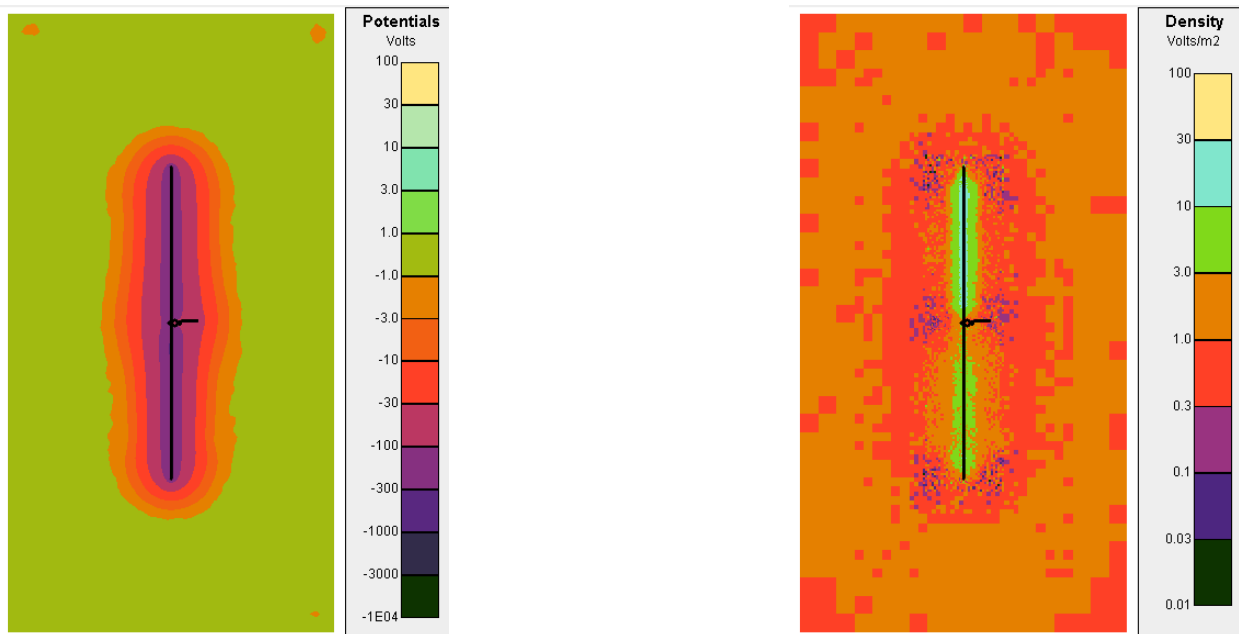

Figure 89. Sheath Structure (Potentials and Densities) for Low Density Calculation at 2.05 ms – Antenna Elements are at –575 V and –573 V – the Bottom Antenna Element was Previously Near Plasma Ground, while the Top Element was Recently/Previously Near -1 kV – Ambient Plasma Density is 1.8 V m^{-2}

The electromagnetic waves from the antenna are created by current flow. The near field current has three components: transverse surface current along the antenna elements, plasma ions, and plasma electrons. The plasma ion currents are obtained directly from the PIC calculations, and are discussed below. The surface currents and volume electron currents are obtained via pseudo-potential methods as discussed in Section 7.

Figure 90, Figure 91, and Figure 92 show the X and Y components of the volume ion current within the computational grid when the antenna elements are at the same potential and at one-fifth and three-fifths of a half-cycle later (near the first and second peaks of the applied potential). The left panels of these figures illustrate how ions that are accelerated toward the antenna and orbit around it form periodic outwardly moving blocks of ions. The details are as follows:

(1) Adjacent to the upper antenna element in Figure 90 (which is in the process of switching from negative to positive) we see the ions (which had been orbiting the antenna) begin to move outward as the attractive force is removed.

(2) In Figure 91, with the electric field now slightly repulsive, a solid block of outwardly moving ions is seen next to the upper antenna element.

(3) In Figure 92 the block of outwardly moving ions separates from the upper antenna element.

(4) Returning to Figure 90 and now focusing on the lower antenna element (which is a half-cycle removed from the upper) we see that the outwardly moving block has radially expanded. The inner portion of the block consists of relatively slowly moving ions that will be recaptured by the increasing negative potential. The outer portion of the block, which consists of more energetic ions that have escaped to the outer, weak field region of the sheath, will continue to move outward. In the high field region immediately adjacent to the newly negative antenna element, the current is high and ion motion consistent with the field direction.

(5) Figure 91 and Figure 92 show continued outward motion of the block around the lower antenna element. Closer to the antenna, ions are moving inward in preparation for forming the next block.

(6) Returning to the upper antenna element, the block we have been following appears (a full cycle later) in Figure 90 about halfway between the antenna and the problem boundary. Its outward motion continues in Figure 91 and Figure 92.

The right panels of these figures show that the Y-component of ion current near the outboard three-quarters of each element is dominated by ions flowing inward along the antenna after being attracted by the field near the boom tip. The Y-component of ion current for roughly the inboard quarter of each element is flowing upward in Figure 90, toward the previously negative element. Due to ion inertia, the current near the root of the upper antenna element is still flowing upward in Figure 91, even though the antenna polarity has reversed. After twenty milliseconds of applying the downward field (Figure 92) the ion flow has reversed to be consistent with the applied field, and is now downward near the antenna element roots.
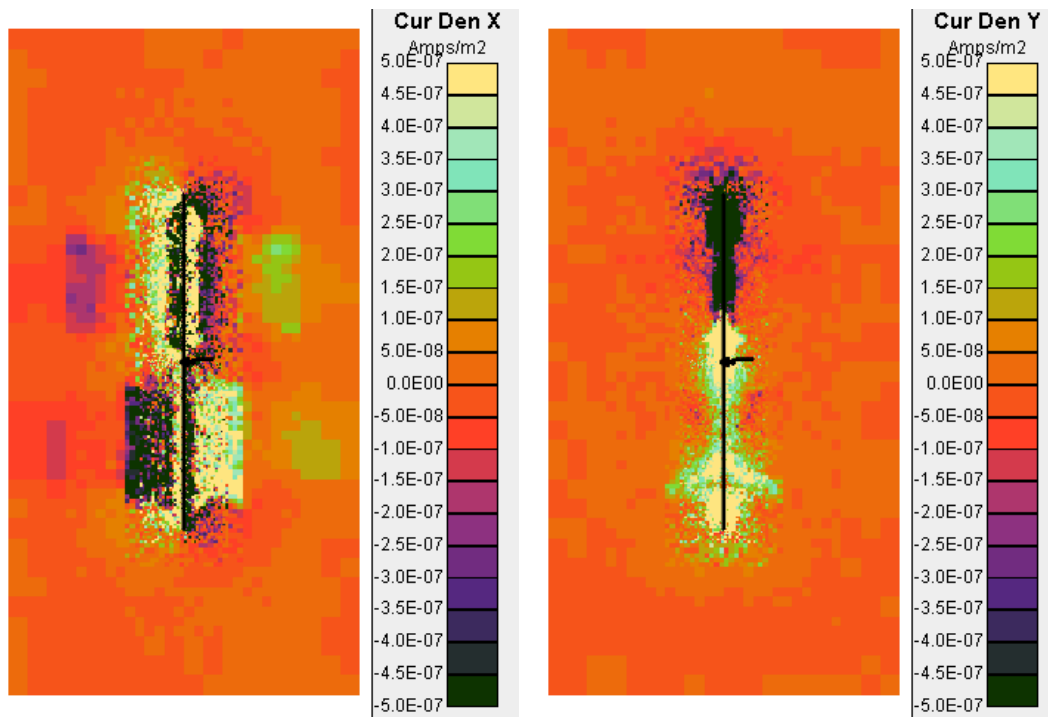
Figure 90. X and Y Components of Volume Current Density Due to Ions at 2.55 ms – Antenna Elements are at –576 V and –578 V – Previously, the Bottom Antenna Element was Near Plasma Ground and the Top Strongly Negative
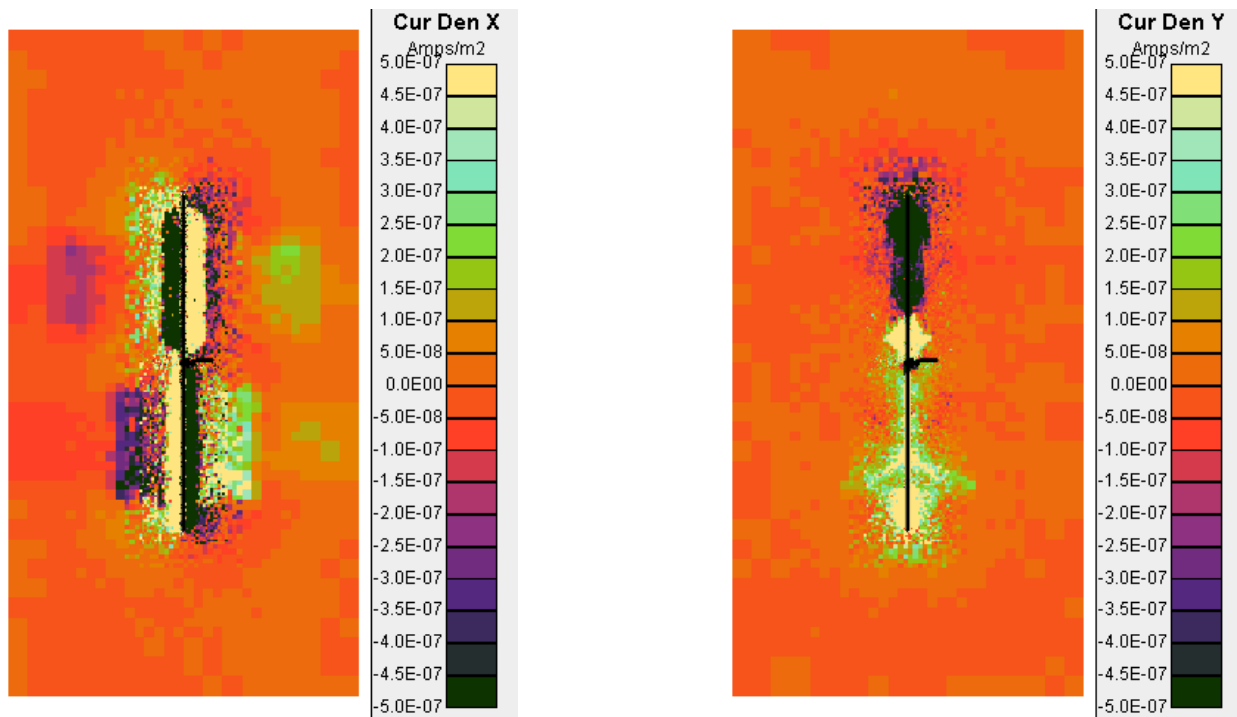

Figure 91. X and Y Components of Volume Current Density Due to Ions at 2.562 ms – Antenna Elements are at -1152 V (Lower) and 1.8 V (Upper)

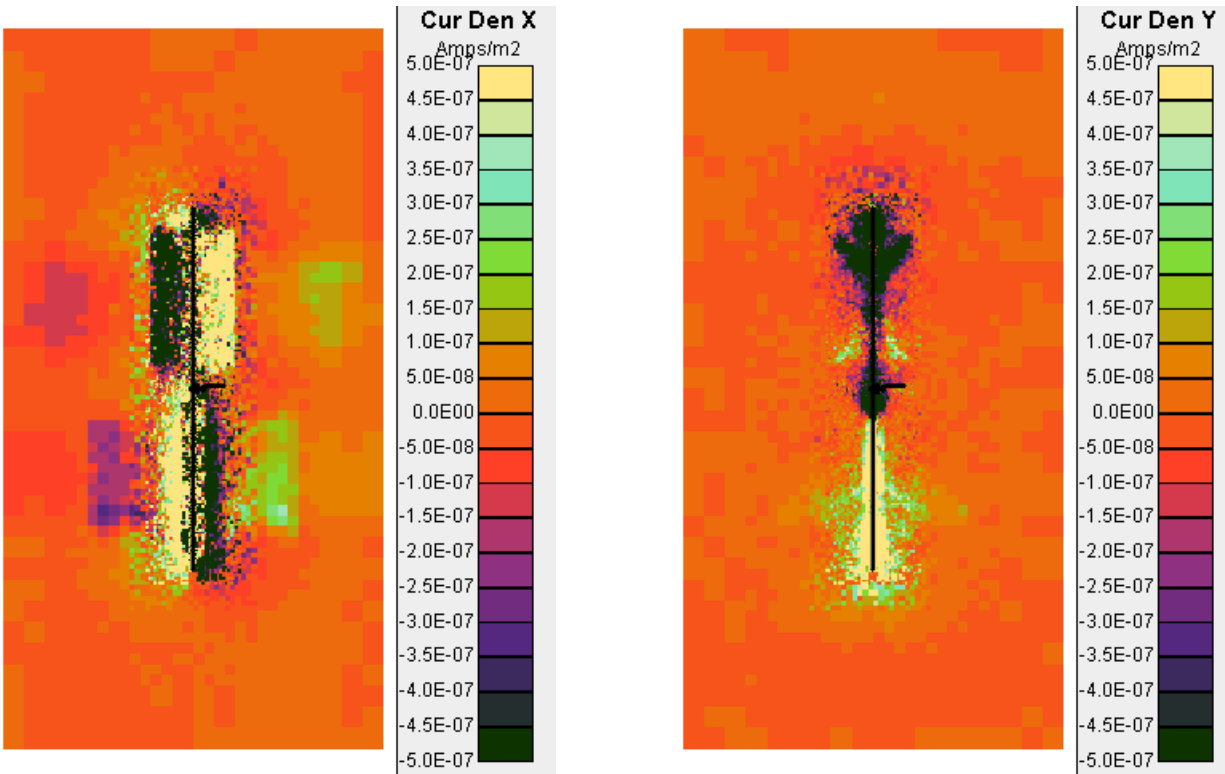**Figure 92. X and Y Components of Volume Current Density Due to Ions at 2.582 ms – Antenna Elements are at -1058 V (Lower) and 0.3 V (Upper)**

Figure 93 and Figure 94 show the vector potential, rate of change in the vector potential, and the magnetic field resulting from the transverse surface current. The radiating electric field is proportional to the rate of change of the vector potential.
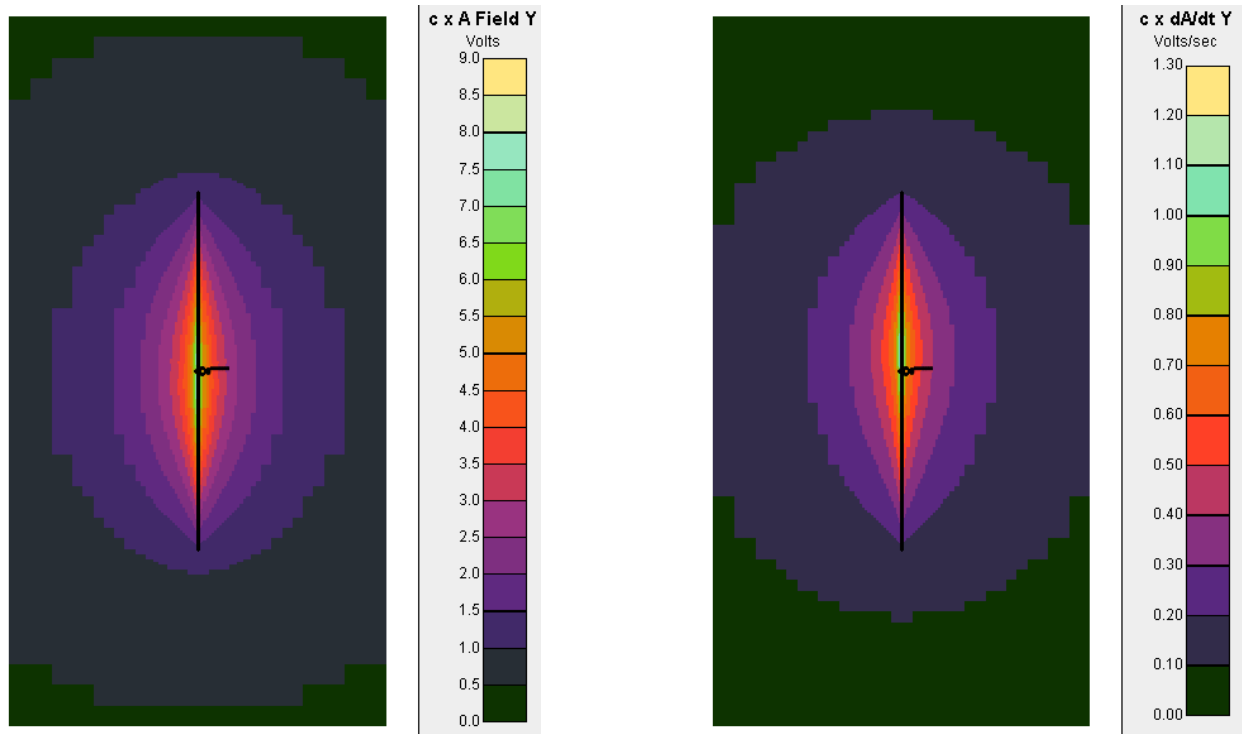
Figure 93. Y Component of the Vector Potential and Rate of Change of the Vector Potential at 2.05 ms as a Result of the Transverse Currents Shown in Figure 50
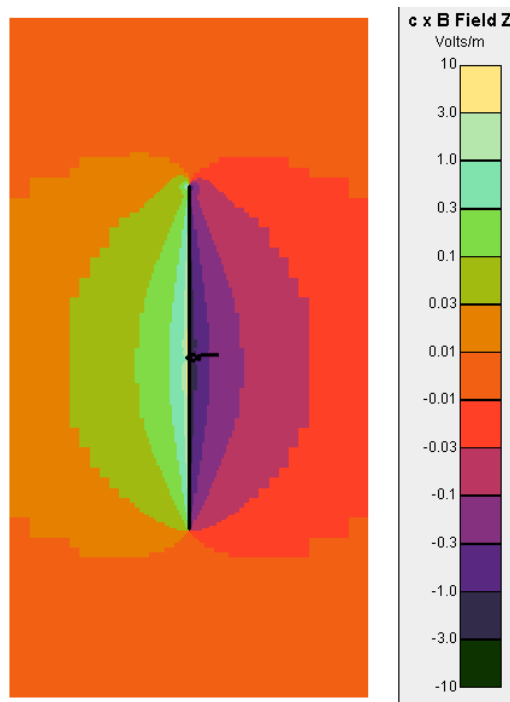

Figure 94. Z Component of the Magnetic Field at 2.05 ms as a Result of the Transverse Currents Shown in Figure 50

10.5 Magnetic Field

We also looked at the effect of the magnetic field on the ion dynamics calculations by repeating the 10 kHz calculation with a 6 μT (0.06 gauss) field in the Y (parallel) direction and in the X (perpendicular) direction. For this magnetic field and 1 kV, the gyroradius of hydrogen ions is 760 m. In both cases, we started the calculation with the result with no magnetic field at 1 ms. As expected there are no discernable differences in the ion surface and volume currents with the magnetic field included in the tracking calculations.

10.6 5 kV

We started a 10 kHz, 5 kV calculation. The time histories of the potentials and currents are shown in Figure 95 through Figure 97. Other than a factor of 5 increase in the voltage and collected current, at 1.3 ms, the results are similar to those at 1 kV at 1.3 ms. The sheath structure near 1.3 ms for 1 kV and 5 kV is shown in Figure 98 and Figure 99. Other than the much larger sheath at 5 kV, the sheath is much the same. The ion currents at 1.3 ms are shown in the final figure. At the higher potential, the released ion current may be more concentrated toward the center of the antenna.
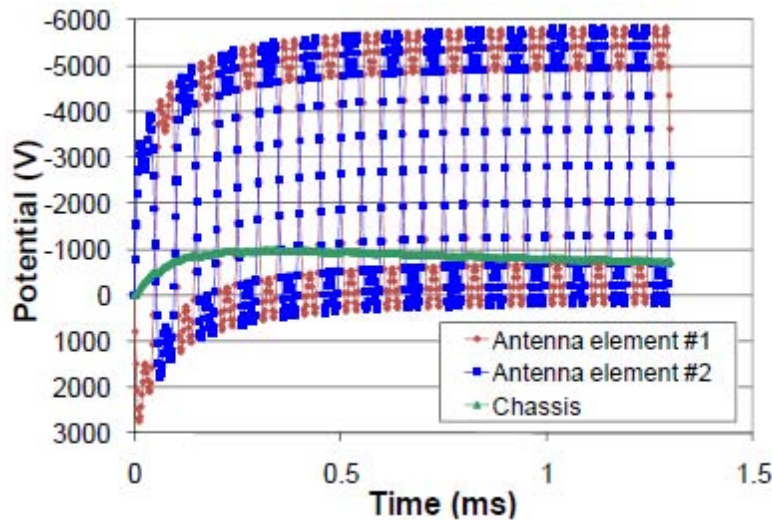
Figure 95. Time Dependence of Antenna Element Potentials for 5 kV at 10 kHz
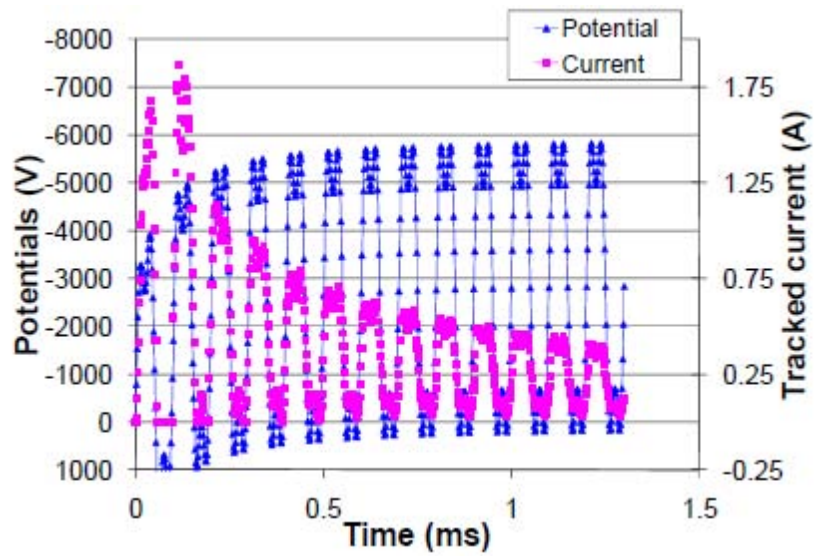
Figure 96. Potential and Collection Ion Current of Antenna Element 2 for 5 kV at 10 kHz

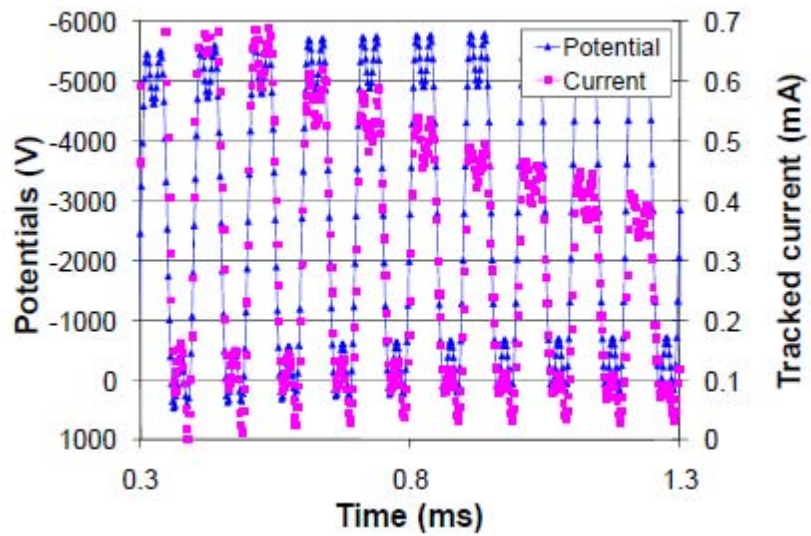**Figure 97. Potential and Collection Ion Current of Antenna Element 2 for 5 kV at 10 kHz (Expanded Scale)**
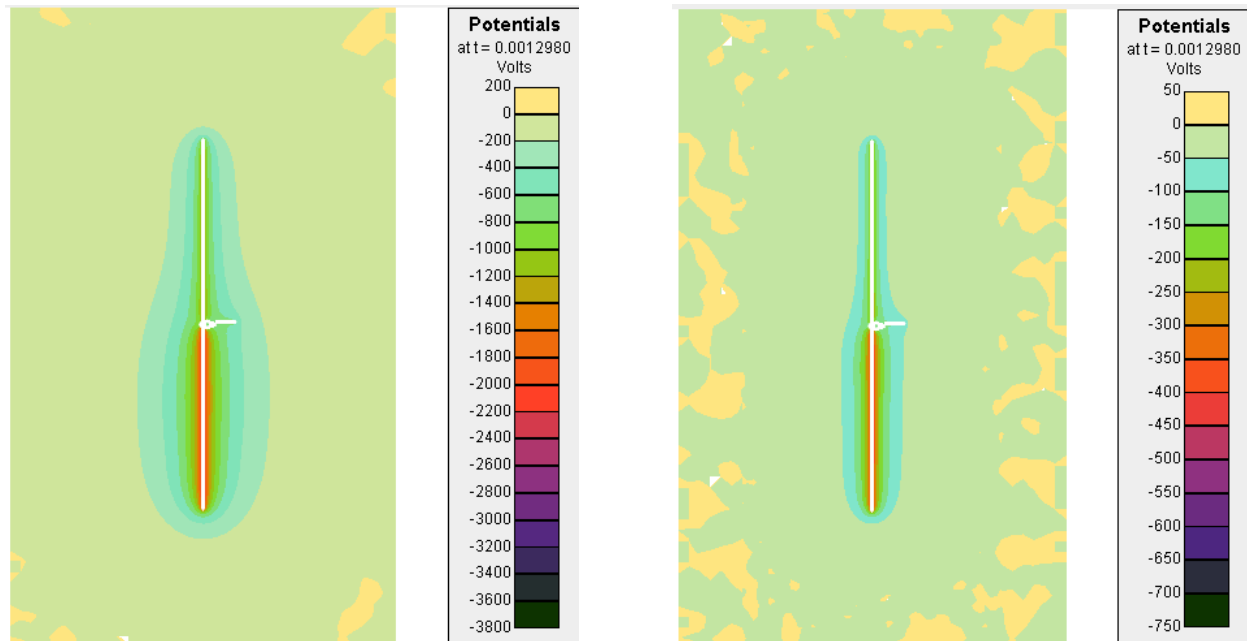
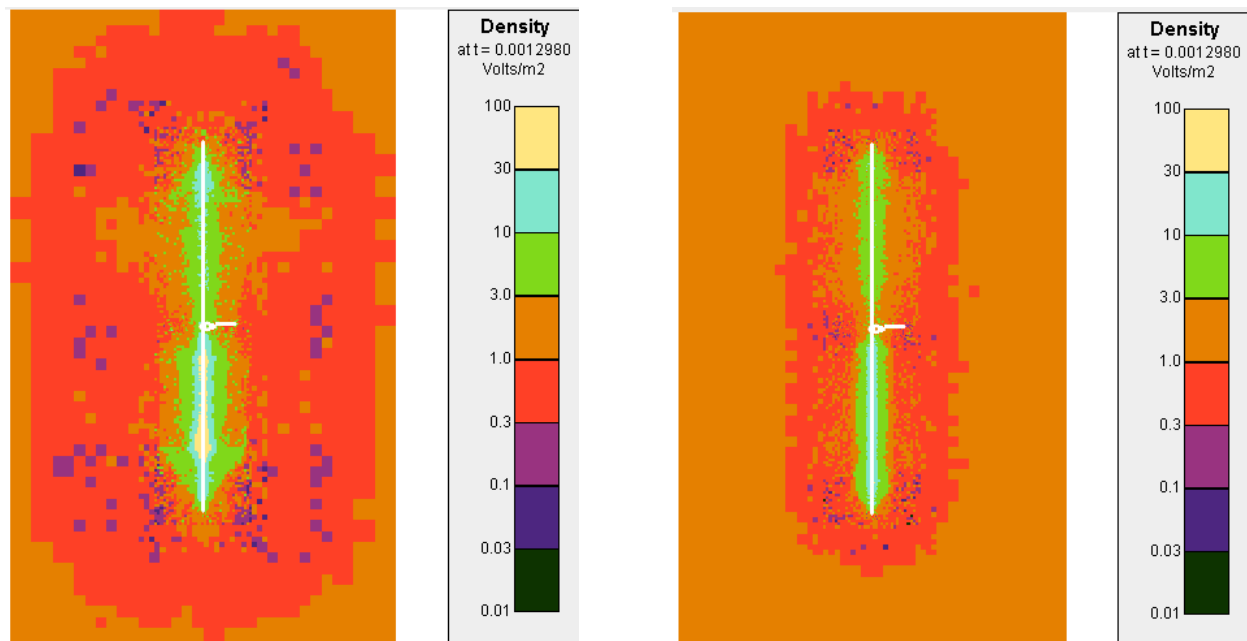**Figure 98. Sheath Structure (Potentials) at 1.298 ms for 5 kV (Left) at 10 kHz and 1 kV (Right) at 10 kHz**

Figure 99. Sheath Structure (Density) at 1.298 ms for 5 kV (Left) at 10 kHz and 1 kV (Right) at 10 kHz – Ambient Plasma Density is 1.8 V m^{-2}

10.7 Conclusions

We have used *Nascap-2k* to study the plasma interactions of a high voltage near-square-wave VLF antenna in MEO plasma. The geometric model captures the main features of the DSX spacecraft. The antenna elements are biased ±1000 V, at frequencies above or below the ion plasma frequency. For these very high applied voltages, the plasma response is nonlinear, and the sheaths are as much spherical as cylindrical, especially at lower densities. In modeling the system it is important to use particle splitting and injection techniques that replenish depleted plasma at boundaries, maintain appropriately sized macroparticles, and provide a reasonable representation of the plasma thermal distribution. When this is done, the incident current is in reasonable agreement with orbit-limited predictions.

The sheath is depleted of ions within every cycle when the antenna is driven below the ion plasma frequency, but not at high frequency. The current lags the applied voltage for excitation frequencies above the ion plasma frequency by 11° at the low density and 13° at the high density, which is much less than the ninety degree shift expected in the linear regime. At low frequency (calculated only for the high density case) the current leads the applied voltage by 13°.

There are three near-field sources of current: current that flows along the antenna element surfaces (supplied by the power supply), plasma ion currents that are attracted and released by the applied potential, and currents of plasma electrons that must vacate an expanding sheath and refill a contracting one. The plasma ion current is computed during the PIC plasma calculation, and has been discussed here. We predict the periodic launch of blocks of energetic ions radially outward into the cold plasma. We have also developed a pseudo-potential method for calculating the surface currents and plasma electron currents self-consistently with the *Nascap-2k* PIC calculation of the sheath dynamics; those results are described in Section 7. These methods allow us to quantitatively predict the disturbances to the presheath plasma that result from the dynamics of the highly nonlinear sheath region, enabling the use of linear plasma theory to predict generation of propagating plasma excitations.

Improvements to *Nascap-2k* over the past six years provide the capabilities needed to predict the near field behavior of electromagnetic transmission from a VLF transmission in a plasma. The first of these improvements is the enhancement of *Nascap-2k* PIC capabilities (particle splitting and injection) and integration of the PIC algorithms with earlier steady-state algorithms. The replacement of the original (1980s) database with a more flexible one with orders of magnitude more storage capability removes the limitation on the size and complexity of problems that can be addressed and also facilitates the use of algorithms that require the storage of more information about the local plasma.

11. CONCLUSION

The program successfully improved the plasma engineering capability available to the spacecraft community. New algorithms for *Nascap-2k* were developed, incorporated, tested, and validated. *Nascap-2k*'s PIC computational capabilities were dramatically improved. *Nascap-2k*'s charging capabilities were enhanced. A transverse surface current model was added and an algorithm developed to compute the volume electron current. Improvements were also made to the

usability of the software. The new database and memory manager, **N2kDB**, enables further *Nascap-2k* development and allows larger calculations to be performed.

The prototype of *Nascap-2k RealTime* is being evaluated by the SEEFS program.

A set of self-consistent calculations of the plasma response to a high voltage square wave VLF DSX antenna were performed in 2007 and repeated with higher fidelity at the end of the contract. These calculations used the new and enhanced capabilities developed under this program.

Much of the work performed under this program has been presented at conferences and published in refereed journals. Details of the work are documented in this and other AFRL reports. At this writing, the next code version, including the new database and memory manager as well as other enhancements, is undergoing beta testing.

The *Nascap-2k* enhancements and new algorithms enable a wide variety of PIC calculations to be performed. In addition, the improvements form the groundwork for further algorithm and software development.

REFERENCES

[1] "Potential Flow," http://en.wikipedia.org/wiki/Potential_flow, last modified 25 February, 2011.

[2] Kershaw, D.S., "The incomplete Cholesky-conjugate gradient method for the iterative solution of systems of linear equations," *J Comp Phys,* **26**, January 1978, p. 43.

[3] Mandell, M.J. Cooke, D.L., *Nascap-2k as a PIC Code, 8th Spacecraft Charging Technology Conference*, Huntsville, AL, NASA/CP-2004-213091, 2003.

[4] Mandell, M.J., Davis, V.A., Cooke, D.L., Wheelock, A.T., Roth, C.J., "*Nascap-2k* simulations of a VLF plasma antenna," *9th Spacecraft Charging Technology Conference,* Tsukuba, Japan, Japan Aerospace Exploration Agency (JAXA), 2005.

[5] Mandell, M.J., Davis, V.A., Cooke, D.L., Wheelock, A.T., Roth, C.J., "*Nascap 2k* self-consistent simulations of a VLF plasma antenna," *10th Spacecraft Charging Technology Conference*, Biarritz, France, June 2007.

[6] Scherbarth, M., Smith, D., Adler A., Stuart, J., Ginet, G., "AFRL's Demonstration and science experiments (DSX) mission," *Advanced Maui Optical and Space Surveillance Technologies Conference*, Wailea, Maui, Hawaii, 2009.

[7] Davis, V.A., Mandell, M.J., Cooke, D.L., and Enloe, C.L., "High-voltage interactions in plasma wakes: Simulation and flight measurements from the Charge Hazards and Wake Studies (CHAWS) experiment," *J Geophys Res,* **104**, A6, June 1999, pp. 12445-12459.

[8] Davis, V.A., Gardner,B.M., Jongeward, G.A., Mandell, M.J., *Spacecraft Potential Control*, AFRL-VS-HA-TR-2004-1152, Science Applications International Corporation, San Diego, CA, July 2004.

DISTRIBUTION LIST

DTIC/OCP
8725 John J. Kingman Rd, Suite 0944
Ft Belvoir, VA 22060-6218   1 cy

AFRL/RVIL
Kirtland AFB, NM 87117-5776   2 cys

Official Record Copy
  AFRL/RVBXR/Adrian Wheelock   1 cy